FACULTY
OF MATHEMATICS
AND PHYSICS
Charles University

MASTER THESIS

Daniela Pittnerová

Functionalization of cerium oxide nanoparticles by simple biomolecules

Department of Surface and Plasma Science

Supervisor of the master thesis: Ing. Nataliya Tsud, Ph.D.

Study programme: Surface and Plasma Physics

Specialization: Surface and Plasma Physics

Prague 2022

I declare that I carried out this master thesis independently, and only with the cited sources, literature and other professional sources.

I understand that my work relates to the rights and obligations under the Act No. 121/2000 Coll., the Copyright Act, as amended, in particular the fact that the Charles University has the right to conclude a license agreement on the use of this work as a school work pursuant to Section 60 paragraph 1 of the Copyright Act.

In…....... date............ signature

I would like to thank to my supervisor Dr. Nataliya Tsud for her patient guidance during the last two years, for teaching me how to acquire, process and understand photoemission data, and for her systematic, but proportionate pressure on me, which kept me going.

My thanks belong to Dr. Anna Fučíková, who significantly helped me with the acquisition of the titration data. I really do owe her not only for introducing me to DLS and AFM techniques, but also for her patience with me in the laboratory and suggestions and comments to my thesis.

I would like to thank to Mgr. Viacheslav Kalinovych and Dr. Yuliia Kosto for their help with measurement and processing of photoemission data. My thanks also belong to prof. Iva Matolínová and the Nanomaterials Group. I would like to acknowledge Synchrotron Elettra and CERIC-ERIC consortium, Trieste for enabling me to perform my experiment there and also the staff of the Materials Science Beamline for their support during my beamtime. I would like to thank the group of Dr. A. Shcherbakov for the preparation of Ce NPs samples studied in this thesis.

Last but not least I would like to thank to my dearest Daniel Dupkala for his never-ending support, patience and boundless understanding. I am sending love also to my family, who supported me all way through my studies.

Title: Functionalization of cerium oxide nanoparticles by simple biomolecules

Author: Daniela Pittnerová

Department: Department of Surface and Plasma Science

Supervisor of the master thesis: Ing. Nataliya Tsud, Ph.D., Department of Surface and Plasma Science

Abstract: Nanoparticles show a great promise in medical applications such as diagnostics and treatment of various diseases. As the biological environment of the living organism is very complex, an extensive research is needed to put the novel alternatives into practise safely. One of the interesting materials for bioapplications is cerium oxide with its unique antioxidant properties. In this work we characterised three systems of bare, histidine-covered and glycine-covered cerium oxide nanoparticles (Ce NPs) in a form of colloid solutions. Colloid stability and reactivity of NPs solutions in various pH were studied using DLS. AFM imaging was utilized to determine the size distribution of NPs clusters and its dependence on the preparation procedure. Synchrotron radiation-based techniques (SRPES, RPES and NEXAFS) as well as laboratory XPS were implemented to investigate electronic structure of the NPs systems with the focus on characterisation of histidine and glycine bonding to Ce NPs surface.

Keywords: cerium oxide; nanoparticles; biomolecules; histidine; glycine

Contents

Introduction

The scientific community has always been trying to move borders of medicine in order to find the best cure for every disease and provide the most suitable treatment to every patient. In the last few years, thanks to the expansion and potential merits, nanotechnologies became a significant part of modern biomedical research. A number of studies on various bioapplications of nanoparticles were recently published. Both organic and inorganic nanoparticles have been studied to inspect possibility of their utilization in drug delivery systems [1–4], bioimaging [5–7] and production of artificial enzymes [8–10].

Materials used for the fabrication of bioapplicable inorganic nanoparticles have to possess suitable properties, such as biocompatibility and nontoxicity. These qualities were confirmed also for cerium oxide [11, 12], although some other papers obtained different results [13, 14]. Apparently, this question is very complex, and therefore more extensive research is needed. In any case, cerium oxide has unique redox properties derived from the ability of Ce cations to easily transit between 4+ and 3+ oxidation states. As a result, there is a wide range of industrial applications of cerium oxide. It is used in fuel oxidation catalysis [15], automotive exhaust treatment [16], chemical mechanical polishing [17], corrosion protection [18], optical devices [19], solar cells [20], oxygen gas sensors [21], etc. As to biomedical applications, cerium oxide nanoparticles (Ce NPs) seem to be suitable for the treatment of disorders caused by oxidative stress [22–24]. They are also an effective radioprotective agent for normal tissues with differential protection in normal cells as compared to tumour cells [25, 26]. Moreover, several studies have shown that cytotoxicity of Ce NPs to cancer cells was more pronounced in comparison with healthy ones [27, 28]. Due to these promising properties, Ce NPs have been widely studied for the fabrication of artificial enzymes [29], bioelectrodes [30] and drug delivery systems [31, 32].

An important parameter determining the utilization of inorganic material in biomedicine is its interaction with the biological environment. For nanoparticles, it is mainly the binding of biomolecules to their surface, which is therefore a key aspect to be explored. By functionalization of NPs by biomolecules their properties can be changed in an advantageous way as described in Refs. [33–35]. The question of bonding is not only crucial but also difficult to answer. With the prospect of simplification, researchers usually employ fewer complex molecules for these studies. Quite simple in their structure/composition, but yet interesting molecules of glycine and histidine fall well into this category. Because of their importance and convenient properties, they are suitable subjects of interest with a focus on their bonding to nanoparticles. A number of studies have already been carried out on glycine- [36, 37] and histidine-functionalized nanoparticles for biomedical applications [38–40].

This work is the final stage of the research line of studying the bonding of amino acids glycine and histidine to cerium oxide of various structures carried out by the researchers from the Nanomaterials group of the Faculty of Mathematics and Physics, Charles University, under the supervision of Dr. Tsud. The research proceeded from the simplest model substrates to more complex systems. At first well-ordered cerium oxide thin films [41], then polycrystalline cerium oxide films [42], and finally cerium oxide nanoparticles were used as a substrate for biomolecules [43]. Here the nanoparticles are the most complex system showing the greatest promise for future bioapplications. First measurements of histidine- and glycine-functionalized Ce NPs were carried out within the bachelor thesis of the author. During the measurements many technical difficulties emerged, mainly connected with charging of the nanoparticles in the photoemission experiments. First results were obtained, but several issues had not been solved.

In this thesis we proceed with research on Ce NPs functionalized with glycine and histidine molecules. Information from the previous studies was utilized to address encountered problems in order to obtain reliable data. Both bare and functionalized nanoparticles were prepared and stored in a form of a colloid solution. The electronic structure of the systems and bonding of molecules to cerium oxide were examined by synchrotron radiation-based techniques (synchrotron radiation photoelectron spectroscopy (SRPES), resonant photoelectron spectroscopy (RPES), and near edge X-ray absorption fine structure spectroscopy (NEXAFS)) and laboratory X-ray photoelectron spectroscopy (XPS). The size distribution of NPs aggregates was determined by atomic force microscopy (AFM). The stability and reactivity of NPs colloid solutions were investigated by the dynamic light scattering (DLS) technique.

1. Studied materials and previous research

1.1. Properties of cerium oxide

Cerium with atomic number 58 is the second element in the lanthanide series and is unstable in the presence of oxygen. With electron configuration $4f^1 5d^1 6s^2$ [44] cerium forms two stable oxides CeO_2 and Ce_2O_3, where it can be found in 4+ ($4f^0$) and 3+ ($4f^1$) oxidation states, respectively [45]. Due to different Ce 4f configurations, the two oxides differ in both core level and valence band structures.

Cerium dioxide (CeO_2) crystallizes in a fluorite structure ($Fm\bar{3}m$ space group), with a face-centred cubic unit cell (Fig. 1.1, left). When CeO_2 is reduced, oxygen vacancies are formed on its surface and phase transition to Ce_2O_3 occurs. Bulk Ce_2O_3 has a hexagonal crystal structure ($P\bar{3}m1$ space group; Fig. 1.1, right) where the layers of -Ce^{3+}-O^{2-}-Ce^{3+}-O^{2-}-O^{2-}- are repeated in the [0001] direction [46]. Thanks to the ability of Ce^{4+} to be reversibly transformed to Ce^{3+}, cerium oxide possesses a unique oxygen storage capacity. Anaerobic reactions (without the presence of oxygen in the gas phase) where cerium oxide is a donor of oxygen can be performed.

Cerium oxide is mostly referred to as a semiconductor in literature. However, the band gap of cerium oxide depends on a number of parameters such as grain size, degree of reduction, presence of vacancies and impurities, etc. Therefore, band gap values published in the literature vary quite significantly. The reported width of the band gap of bulk CeO_2 is in the range of 3 – 3.6 eV [47], with the most stated value of 3.2 eV [48, 49]. The band gap of Ce_2O_3 is in general lower in comparison with CeO_2 [50]. Ce NPs of size 11 to 16 nm, where Ce cations of both phases are expected, were reported to have a band gap of 2.8 eV [48].

It was shown, that the electronic conductivity of cerium oxide single crystal is smaller than the conductivity of bulk polycrystalline cerium oxide. Conductivity increases with decreasing grain size. The different types of conductivity characteristics for cerium oxide with varying grain size were also found. Under conditions at which microcrystalline cerium oxide exhibited impurity-controlled ionic conductivity, nanocrystalline samples showed electronic conductivity [51].

The lattice parameter of CeO_2 single crystal is $a = 0.541134\ nm$ [45]. For Ce NPs lattice parameter depends on their size. Lattice expansion was observed for the

NPs with a diameter of 10 nm or smaller, with the value up to 7 % higher for 1 nm Ce NPs [52]. The expansion is due to the substantial amounts of Ce^{3+} ions together with the associated vacancies present on the NPs' surface.

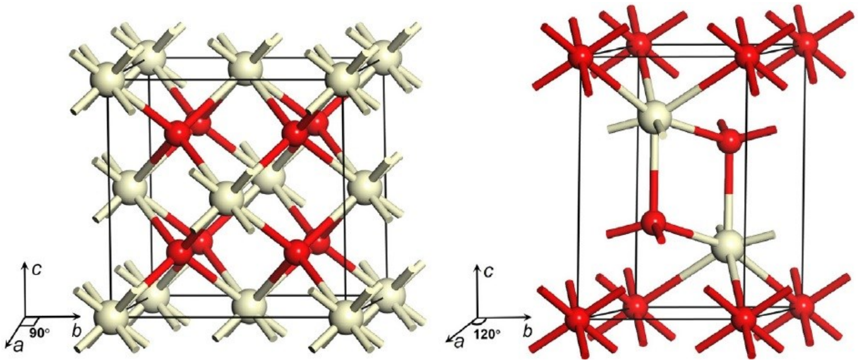

Figure 1.1: Fluorite-type crystal structure of CeO_2 (left) and hexagonal crystal structure of Ce_2O_3 (right). Red and grey spheres represent O and Ce atoms, respectively [53].

1.2. Model biomolecules: glycine and histidine

Glycine (Fig. 1.2, right) with a molecular formula $C_2H_5NO_2$ is the simplest amino acid consisting of the carboxyl group (-COOH) and α-amino group ($-NH_2$) only. It is a non-essential, non-polar, non-optical and glucogenic amino acid [54]. Glycine usually appears as white odourless crystals with a sweet taste. It is water soluble and a 0.2 M aqueous solution has a pH of 4.0, so it acts as a weak acid. The decomposition of glycine starts at 233 °C and its melting point is at 262 °C [55]. Glycine plays an important role in the production of DNA, phospholipids, collagen and hormones connected with immunity responses [56]. The anti-inflammatory, antioxidant and antipsychotic activity of glycine have also been shown. As glycine is also a fast-inhibitory neurotransmitter, it may have antispastic activity as well. It has also been used therapeutically as a nutrient [54].

Histidine (Fig. 1.2, left) with a molecular formula $C_6H_9N_3O_2$ is a bit more complex amino acid compared to glycine including also an imidazole ring (IM) group. Similarly to glycine, histidine can also be found in the form of white crystals with a sweet taste and without any odour. It is also water soluble. The melting point of histidine is at the temperature of 287 °C [57]. Histidine, as an essential amino acid for humans and mammals, is needed for the production of histamine, growth, tissue repair, blood cell production and maintenance of the nervous system [58]. Due to its anti-inflammatory, anti-oxidant and anti-secretory properties [59], it is used to treat allergies, anaemia, ulcers and rheumatoid arthritis [57].

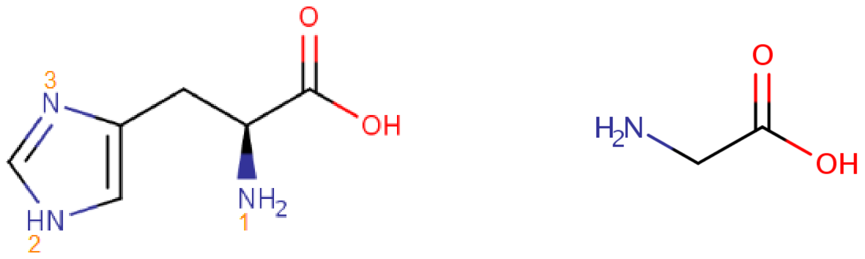

Figure 1.2: Schematic structure of a histidine (left) and glycine (right) molecule.

Amino acids in general are amphoteric molecules, which means they can act as both an acid and a base. More specifically they are amphiprotic molecules, so they can either accept or donate a proton (as an H^+ ion) [60]. This is an important property which determines their behaviour in solutions with different pH. In the neutral aqueous solution, an amino acid is naturally ionized as the carboxylic group loses a proton forming $-COO^-$ group and on the contrary, the amino group accepts a proton forming $-NH_3^+$ group. The molecule with zero net electrical charge and ionized carboxyl group $-COO^-$ is called a zwitterion. The amino acid occurs in this form when the pH of the solution is equal to the isoelectric point (IEP; the pH at which the molecule carries no net electrical charge) of the acid [61]. With decreasing pH, zwitterionic form alters and the net charge of the molecule becomes positive. pH at which the capacity of the molecules to accept protons is over, and therefore all molecules are in the form of positive ions, is called an acid dissociation constant (pK_a). In the basic environment, the amino acid molecule donates protons to the solution and becomes negative. Analogously to the acid environment, there exists also a base dissociation constant pK_b. The IEP is calculated as an average from pK_a and pK_b values. When the molecule has more sites which can donate or accept protons, it has more pK values at which different forms of the molecule are present in the solution. Three possible forms of the glycine molecule and four possible forms of histidine molecule in different environments are depicted in Fig. 1.3. From this behaviour follows, that amino acids behave as weak bases in an acidic environment and as weak acids in a basic environment.

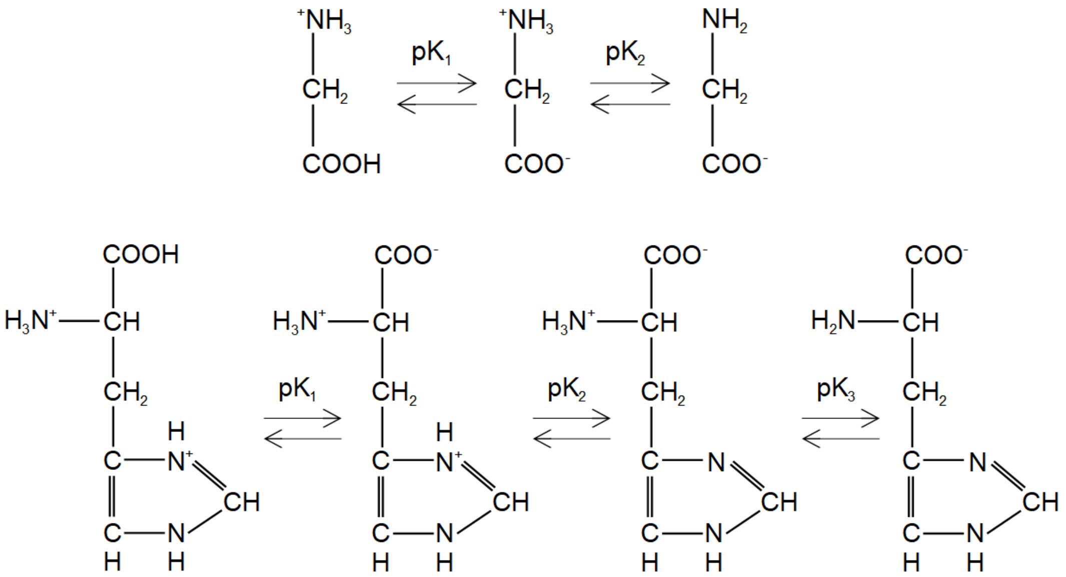

Figure 1.3: Possible forms of glycine (up) and histidine (down) with the dissociation constants corresponding to the particular transitions.

The pK values for glycine and histidine taken from Ref. [62] are shown in Table 1.1. Glycine pK values were measured at 20 °C and are valid for ionic strength of glycine solution in a range of 0.01 – 0.36 M. pK values for histidine were measured at 23 °C for the 0.1 M molecular solution.

Amino acid	pK_1	pK_2	pK_3
Glycine	2.36	9.91	-
Histidine	1.78	5.97	8.97

Table 1.1: Experimentally determined pK values of glycine and histidine.

1.3. Previous research

Previous research by Dr. Tsud started with well-ordered cerium oxide films [41] (0.15 nm thick) on Cu(111) used as a substrate for histidine deposited by evaporation in a vacuum. It was found, that in this case deprotonated carboxylate group, α-amino nitrogen and imidazole ring are all bound to the cerium oxide surface. In a follow-up study, polycrystalline cerium oxide films on monocrystalline Si(100) were used as a substrate [42], while the deposition process of histidine remained the same. It was found, that histidine binds to the cerium oxide surface via the carboxylate group only and imidazole rings formed intermolecular bonds. On the polycrystalline cerium oxide substrate, a change of deposition technique of histidine was also examined. In the case of histidine adsorption from a neutral aqueous solution under a nitrogen atmosphere [63], the bonding of molecules to cerium oxide occurred via carboxylate groups only, as in the previous study. IM ring and amino side group were involved in the intermolecular bonding. From these findings follows, that the surface structure of the cerium oxide is the key factor determining the way of histidine binding and that the results from the systems where histidine was deposited by evaporation in ultra-high vacuum (UHV) partially represent a more biocompatible deposition technique using aqueous histidine solution.

Research on the glycine-covered cerium oxide has also been carried out in our group [64]. The study started with model substrates - stoichiometric $CeO_2(111)/Cu(111)$, partially reduced $CeO_{1.7}(111)/Cu(111)$ and fully reduced $Ce_2O_3(111)/Cu(111)$ thin films. Deposition of glycine was performed by evaporation from a Knudsen cell in a vacuum. It was shown, that presence of oxygen vacancies in cerium oxide plays a key role in the adsorption chemistry of glycine. Glycine was adsorbed to all of the studied surfaces via the deprotonated carboxylic group, but the orientation of the molecule varied. On the CeO_2 substrate, glycine is orientated almost parallel to the surface as oxygen anions of the substrate attract the amino group of the molecule. In the case of Ce_2O_3 and $CeO_{1.7}$ surfaces, bonding of glycine occurs via the carboxylate oxygens incorporation into the vacancies of the substrate and the amino group protrudes from the surface. From the studies of thermal stability follow that molecular bonding strengthens with increasing concentration of oxygen vacancies on the surface [64]. In the next stage of the research, a substrate was changed to polycrystalline cerium oxide. Glycine molecules were deposited by evaporation in a vacuum and also by deposition from an aqueous solution under an inert atmosphere in a glove bag. Both ways of deposition led to the bonding of glycine to polycrystalline cerium oxide via a deprotonated carboxylate group. The amino group of glycine deposited in UHV was in a neutral state, but glycine deposited from an aqueous solution had protonated amino group. The deposition in UHV resulted in the formation of a more stable molecular adlayer, due to additional bonding of surface oxygen cations to α-carbon of the molecules, which was enabled by the flat adsorption geometry of glycine and grain structure of the substrate. Orientation of glycine deposited from aqueous solution varied between all possible variations, while the C-C bond was locally parallel to the oxide surface [64].

1.4. Goal and structure of the thesis

In this thesis, we present the results of the research on the properties of cerium oxide nanoparticles (Ce NPs). Three samples were analysed – bare Ce NPs (sample CO) and Ce NPs functionalized by glycine (sample CG) and histidine (sample CH). Samples of Ce NPs were prepared and stored in the form of colloid solutions, therefore stability of these solutions represented by their zeta potential (ZP) was studied using dynamic light scattering (DLS). ZP was measured in the neutral, acidic and basic pH. Titration experiments were performed to examine the properties and behaviour of Ce NPs in environments with different pH and how these vary with different surface functionalization. The results of these measurements are shown in Subchapter 3.1.

Depending on the ZP of the Ce NPs, their functionalization and sample treatment, clusters of various sizes are formed. Size distribution of the smallest Ce NPs clusters in a dried drop was measured by atomic force microscopy (AFM) at acidic, neutral and basic pH. Results from AFM confirmed the hypothesis derived from the titration measurements that a more uniform layer of Ce NPs can be prepared in a basic and acidic environment compared to a pH-neutral one. The findings of the AFM study are presented in Subchapter 3.2.

The electronic structure of the samples was studied by a series of photoelectron spectroscopies (X-ray photoelectron spectroscopy (XPS), synchrotron radiation photoelectron spectroscopy (SRPES) and resonant photoelectron spectroscopy (RPES)) and near-edge X-ray absorption fine structure spectroscopy (NEXAFS). Combining these techniques, we obtained a comprehensive view of studied systems, as photoelectron spectroscopies (PES) provide information about occupied electronic levels and complementary information about unoccupied levels follows from NEXAFS data. The key issue about the bonding of amino acids to Ce NPs was also solved by analysis of the obtained spectra. Using RPES, the degree of reduction of cerium oxide was examined. Findings related to these techniques are shown in Subchapter 3.3 for photoelectron spectroscopies and Subchapter 3.4 for NEXAFS. Results of the AFM study were applied during the samples' preparation for PES and NEXAFS in order to eliminate the charging effect and acquire reliable data.

2. Experimental methods, instrumentation and sample preparation

2.1. Dynamic light scattering

2.1.1. Theory and principle of DLS

Dynamic light scattering (DLS) is a method used to determine the size distribution of nanoparticles (NPs) in colloid solutions. When the laser beam is shined on the colloid solution, the NPs scatter the laser beam and the light speckle pattern is observed. As NPs diffuse due to Brownian motion, which depends on their size, the intensity at any particular point of the speckle pattern fluctuates. By measuring the rate of these fluctuations at particular points of the speckle pattern, the correlation function can be determined. Then, using the Stokes-Einstein equation, the size distribution of the NPs can be calculated.

Properties and behaviour of NPs colloid solution are greatly influenced by charges present in it. The surface of NP in a liquid medium is usually charged, and therefore an electrical double layer (Fig. 2.1) is created around it [65]. Ions in the inner part of the double layer, called the Stern layer, are strongly bound to the NP. The outer region of the double layer is called the diffuse layer, in which a notional boundary called the slipping plane exists. Ions within this region stay attached to the NP and travel with it when NP moves. The electric potential between NPs and the slipping plane is called zeta potential (ZP) and determines the stability of the colloid solution. A higher absolute value of ZP means higher stability due to increased Coulombic repulsion of individual NPs [66]. ZP typically ranges between -100 and +100 mV, while solutions with ZP above +30 and below -30 mV are considered colloidally stable.

The most important parameter of the solution concerning ZP is pH since the NP is balancing out the ions beyond the slipping plane in reaction to different pH. To examine the dependence of ZP of a particular colloid system on pH, titration experiments are performed. In these experiments, the pH of the solution is changed step by step in a selected range and ZP is measured at every point. Titration is usually performed in several cycles to observe changes in titration curves. In the acid

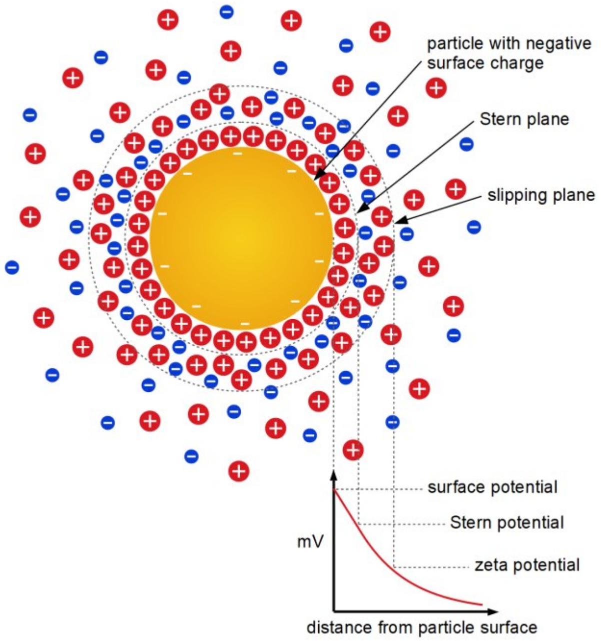

Figure 2.1: Illustration of the electrical double layer around nanoparticle in solution and meaning of zeta potential.

environment, our NPs tend to acquire the positive charge, which leads to the positive value of ZP, while in the basic environment NPs usually have negative ZP. The titration curve in the direction from acidic to basic pH can be different from the titration curve in opposite direction. Such behaviour is called hysteresis of the titration curve. Hysteresis usually occurs when the system does not have enough time to “forget” its past. Therefore, ZP values in direction to base are more positive due to the starting point at lower pH than ZP values in direction to acid with the starting point at the higher pH. Hysteresis is connected to different numbers of positive ions adsorbed during titration to acid from the number of adsorbed negative ions during titration to base. An important point of the titration curve is an isoelectric point (IEP) – the value of pH when the ZP of NPs equals zero. At this point, the colloid solution is the least stable, which is important information for practical applications. Due to the lack of Coulombic repulsion, the NPs tend to agglomerate, which might be permanent even if we move away from the IEP point. When hysteresis is present in the titration curves, IEP points following from titration to acid and to base are not identical. The actual IEP lies somewhere in between them, but not necessarily in the middle.

In the devices, ZP is usually determined indirectly, for example by calculation from electrophoretic mobility using the Henry equation [65]. Electrophoresis is a process when the external electric field is applied to the solution containing charged

NPs and due to Coulombic attraction NPs start to move to the electrode with opposite charge. The velocity of the moving NPs divided by the intensity of the applied electric field is called electrophoretic mobility. This velocity is measured by the Laser Doppler velocimetry (LDV) technique based on DLS. A laser beam is sent through the capillary cell and the frequency shift of the light scattered from a nanoparticle in motion due to the Doppler effect with respect to the reference beam is measured [67]. Zetasizer instruments [68], which we used to perform our measurements, are using a more sophisticated M3-PALS technique based on LDV. By M3, the undesirable electroosmosis effect arising from the surface charge of the capillary wall can be avoided. Phase analysis light scattering (PALS) technique measures not the frequency shift, but the phase shift of the scattered light, which leads to higher sensitivity and accuracy of the measurements.

2.1.2. Instrumentation, measurement and data processing

Data were measured by Zetasizer Nano ZS [69] from Malvern equipped with NBIS optics and M3-PALS technology. The device uses a laser with a power of 4 mW and a wavelength of 633 nm. It is possible to measure the ZP in the range of ±500 mV and the size of particles from 0.3 nm to 10 μm in diameter [70]. The sample solution was measured in a disposable folded zeta potential capillary cell DTS1070. Most of the titration experiments were performed automatically using MPT-2 autotitrator equipped with three syringe dispensing units. Some of the titrations needed to be performed half-manually, as the software was jamming due to the behaviour of some of our samples. This behaviour is described in detail in Subchapter 3.1. In a half-manual titration, titrants were added to the sample by a person in order to add just the right amount of titrants. 0.2 M and 0.02 M HCl, and 0.25 M NaOH were used as titrants. The pH of the samples was measured using the laboratory pH meter HC 133-FES. In the settings for our measurements, the refractive index of cerium oxide NPs was set to 2.2 [71] and the absorption to 0.06. The value of absorption was determined in previous measurements of the system with Ce NPs performed by our group [72]. Smoluchowski model was used for the analysis of the correlation function. For titration measurements, the temperature of the sample was set to 20 °C.

ZP of Ce NPs (CO, CH and CG) were measured in neutral, acidic (around 4.8) and basic (around 8.5) pH. Preparation of the samples is described in Subchapter 2.4.1.

Each sample was measured 3 to 5 times to obtain better statistical information. Measurement was repeated more than 3 times when the acquired ZP distribution varied more notably. The ZP was calculated for each sample as an average of the mean ZP values obtained. The final deviation was calculated as half of the highest standard deviation of individual measurements, which were determined from the ZP distribution by the Zetasizer.

Titration experiments were carried out for three original NPs solutions CO, CH and CG. In these experiments pH of the sample was changed step by step from the initial value to the minimum (or maximum) preset value. If the sample is titrated from neutral pH to acid pH, it is named titration to acid according to the direction in the 0th round. If it is titrated from neutral to basic pH, it is named titration in direction to base. When the threshold pH was reached, titration continued in opposite direction. For each type of NPs, both types of titration (to acid and to base) were carried out. This enables us to observe if the titration curve is direction-dependent and if there is any hysteresis in the samples or permanent change in the surface bonds at extreme pH values or in various ionic concentrations or due to transition through the IEP. From these results we can predict the behaviour of samples in the biological environment and the stability of samples. We performed from two up to four titration cycles in each titration experiment. The pH titration range was selected between pH 4 and pH 9.5. We did not go below pH 4, as CeO_2 starts to decompose in this environment. Titration pH steps varied among the samples, from around 0.3 pH unit as the smallest pH step to the 1 pH unit as the biggest pH step. After each change of pH, the ZP of the sample and NPs' size were measured. For every measured ZP point, the conductivity of the sample was measured as well. The behaviour of the conductivity can support some results following from the titration curves. Also, the results of the titrations cannot be considered reliable if the conductivity increases above 2 mS/cm. As we analysed mainly the relative conductivity change, in the graphs it is displayed only as mean values without deviations.

At each measurement point, ZP and size of particles (their hydrodynamic diameter) were measured twice in at least 2 min intervals in order to allow stabilization of the sample and to obtain reliable results. The whole titration is usually automatically carried out by the device. However, the samples CH and CG have rather unique buffering properties due to which the Zetasizer machine got jammed. Therefore, measurements of these samples had to be performed half manually.

Data were obtained and processed by Zetasizer software 7.13 [73], by which ZP and particles' size distributions, mean values and standard deviations in each pH point were determined. For further processing software LibreOffice Calc 6.0.2.1 [74] and OriginPro 2020b 9.7.5.184 [75] were used. Aggregation and disaggregation of the NPs with changing pH were observed in the measured data. However, due to the presence of dust in the samples, which adds a significant contribution to the light scattering, we can obtain just the general trends in the clusters' size changes. Therefore, the exact size of the NPs clusters cannot be determined by the DLS method.

2.2. Atomic force microscopy

2.2.1 Theory and principle of AFM

Atomic force microscopy (AFM) is a scanning probe microscopy technique which uses interatomic forces for imaging the sample. The main advantage of AFM is the possibility to use it not only in a vacuum but also in a gaseous and liquid environment. A key part of the AFM is a cantilever, a plate spring with a sharp tip at its end. The tip is scanned over the sample surface using piezoelectric elements, which position is determined by the laser deflection from the cantilever. This reflection is recorded and then converted into the height profile of the sample. The movement of the tip is usually tracked by a laser beam reflected by the cantilever and detected by a four-quadrant photodetector (Fig. 2.2).

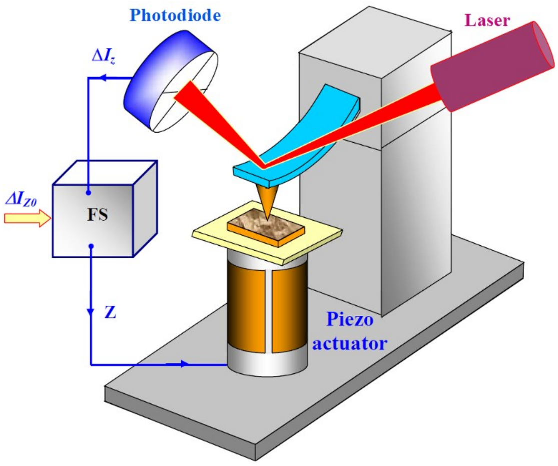

Figure 2.2: Schematic illustration of AFM with optical lever detection. Taken from [76], modified.

The force between the tip and the sample can be described by Lennard-Jones potential *U* (Fig. 2.3) given as:

$$U = 4\varepsilon\left[\left(\frac{\sigma}{r}\right)^{12} - \left(\frac{\sigma}{r}\right)^{6}\right]. \qquad (2\text{-}1)$$

Here ε is the depth of the potential well (at distance $r_m = \sqrt[6]{2}\sigma$), σ is the distance at which the potential energy is zero and *r* is the tip-sample distance. The first term in the Equation (2-1) describes long-distance attractive potential caused by dipole-dipole interaction, while the second term involves Pauli repulsion resulting from overlapping of electron orbitals [76]. Then the force *F* can be calculated as a minus gradient of the potential. Due to force interaction cantilever will be bent according to the Hook's law:

$$F = -k\Delta z, \qquad (2\text{-}2)$$

where *k* is a spring constant of the cantilever and Δ*z* is its deviation from equilibrium in the *z*-direction. Basic AFM modes can be divided into static and dynamic modes and they can also be characterized by a measure of contact between the tip and the sample (Fig. 2.4) [77].

In a static or contact mode cantilever is scanning the sample surface without moving in a vertical direction (usually marked as *z*-direction). There are two types of contact modes: constant height and constant force. In constant height imaging mode, the *z* coordinate of the cantilever is held constant while scanning. Parts of the sample with different heights experience different forces, which is used for obtaining the contrast. Measuring using this mode is fast, however, there is a high risk of destroying both the sample and the tip due to possible collisions. Therefore, the constant force

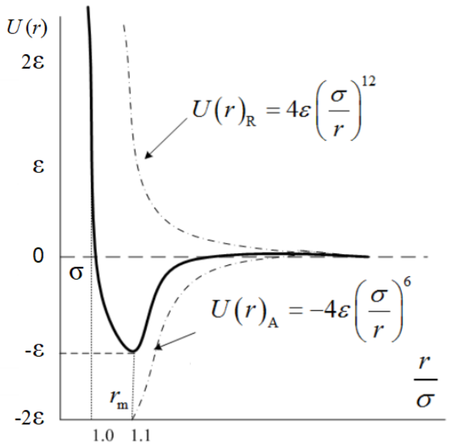

Figure 2.3: Lennard-Jones potential as a sum of repulsive and attractive potentials. Taken from [78], modified.

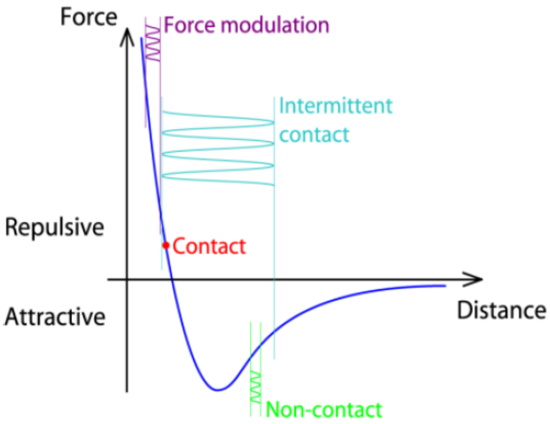

Figure 2.4: Basic AFM modes depicted according to the potential region in which they operate [77].

imaging mode is more widely used, as in this case the cantilever height is adjusted by the feedback loop so that the force between the tip and the sample is constant during the imaging. The static mode provides high-resolution images, but soft samples can be damaged due to direct mechanical interaction with the tip.

In dynamic modes, the cantilever is vibrating close to its resonance conditions and frequency or oscillation amplitude modulations caused by interaction with the sample are measured as a signal. Several dynamic AFM modes can be classified. If the tip stays in a region of repulsive forces, we talk about a force modulation mode.

In the intermittent contact mode, the tip oscillates between the repulsive and attractive force regions. Usually, the amplitude of oscillations is held constant by the feedback loop and the voltage needed to recover the setpoint amplitude after its deviation by the sample is used as a signal. A phase shift of the resonant frequency can provide information about the stiffness or adhesion of the sample. As the repulsive force is applied to the sample only for a short part of the cantilever cycle, damage to the sample is significantly reduced compared to contact mode.

2.2.2. Instrumentation, measurements and data processing

Data were measured using JPK NanoWizard 3 Bioscience AFM module equipped with Life Science Stage and inverted optical microscope Olympus IX73. CCD camera JUnicam serves for the observation of the sample surface, cantilever movement during adjustments and measurement. The whole system is located in a sealable acoustic enclosure. The table holding the microscope is standing on pneumatic legs damping external vibrations.

As a probe, cantilever AppNano ACTA-20 was used. This cantilever operates in a frequency range of 200 to 400 kHz and its spring constant lies between 13 and 77 N/m. The tip has a pyramidal shape and its radius of curvature is smaller than 10 nm.

AFM images 10×10 μm with resolution 512×512 px were acquired using intermittent contact AC mode. For every sample which showed suitable concentration and distribution of NPs, several images were taken to have a reasonable amount of data (at least 100 data points equalling to NPs heights) for statistical analysis.

First of all, samples with neutral pH were studied. Measurements started with bare Ce NPs in the order: CO_w, CO and CO_s (information about these samples can be found in Subchapter 2.4.2). In the next step samples with functionalized Ce NPs were measured, i.e. CG and CH. Afterwards, images of the samples (CO, CG and CH) with basic pH were acquired and the measurements were finished by samples with acidic pH.

JPK NanoWizard Control was used for the data acquisition. Basic processing of the raw images was performed in JPK Data Processing software, where the linear or polynomial background was subtracted from the images and selected horizontals scars were replaced by interpolation of neighbouring lines. The images suitable for statistical analysis of cluster sizes were further processed using an internal script based on Mathematica software. Using this script, particles or clusters were bordered and their height and area were determined. Afterwards, cluster size distribution was established according to the measured heights of the clusters. Software OriginPro 2020b 9.7.5.184 [75] was used for creating histograms of obtained size distributions. Using Origin, the histograms were fitted with Gaussian distribution, from which the mean value of the cluster size and FWHM (full width at half maximum) of the peak were determined. However, images of some samples were not suitable for the statistical analysis as the majority of Ce NPs aggregated into super big clusters. In this case, the height profiles of the clusters were measured using JPK data processing software.

2.3. Photoelectron spectroscopies and near edge X-ray absorption fine structure spectroscopy

2.3.1. Theory and principle of PESs

Photoelectron spectroscopies (PESs) are surface-sensitive techniques based on the photoelectric effect (Fig. 2.5). When light with sufficient energy irradiates a sample, an incident photon is absorbed by an atom of the sample and its energy is transferred to an electron, which is subsequently ejected. The kinetic energy E_k of the emitted electron, called photoelectron, depends on the energy of the incident photon $h\nu$ according to the equation:

$$E_k = h\nu - E_b - \varphi, \tag{2-3}$$

where h is Planck's constant, ν is the frequency of the incident photon, E_b is the binding energy of the ejected photoelectron and φ is the work function of the spectrometer. The intensity of the photoelectrons as a function of their kinetic energy is measured by a spectrometer. However, the electronic structure of the samples is usually determined by analysing the intensity, shape and binding energy of the photoelectron peaks. Therefore, E_k is converted to E_b using *Eq. (2-3)*.

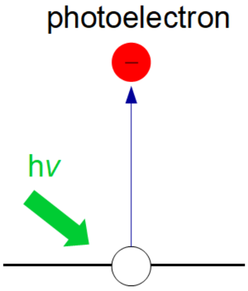

Figure 2.5: Diagram of the photoelectric effect.

The intensity of the photoemission peak I_A of the specific level A of chosen material M can be described by the equation:

$$I_A = K\sigma_A(h\nu)\lambda(E_A)n_M \tag{2-4}$$

where $\sigma_A(h\nu)$ is a photoionization cross-section of electronic level A dependent on photon energy $h\nu$; $\lambda_M(E_A)$ is the inelastic mean free path (IMFP) of photoelectrons in material M with kinetic energy E_A; n_M is the concentration of the studied material M; K is the coefficient, which includes different parameters (detector efficiency, transmission function of the analyser, photon intensity, etc.) and assumed to be a constant during the measurement.

Sampling depth, i.e. depth in the sample from which the information arises, is defined by IMPF of photoelectrons in a given material. The IMPF value is determined by the photoelectron kinetic energy. This dependence is represented by the so-called universal curve, which is shown in Fig. 2.6.

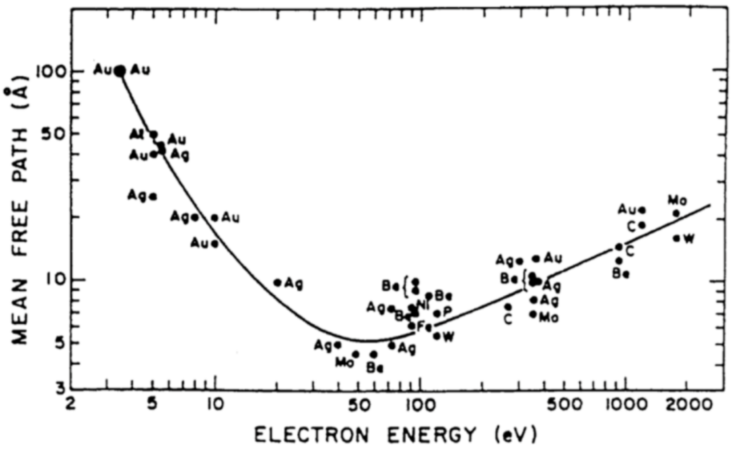

Figure 2.6: Universal curve of an inelastic mean free path as a function of electron kinetic energy for chemical elements [79].

Among other parameters, distinct spectral features observed in the photoemission from a specific level of the element depend on the type of the occupied electronic orbital. As a result of spin-orbit coupling, intensity arising from *p*, *d* or *f* orbitals are observed as doublets, while electrons from *s* orbital create a single photoelectron peak called a singlet. The chemical environment of the emitting atom directly affects the peak position in the spectrum. Therefore, the information extracted from PES spectra regards not only the chemical composition of a sample but also the chemical states of the atoms. In PES, the final state of the emitting atom plays also an important role. Sometimes more than one final state of photoemission can exist. In this case, every final state is represented as the peak (singlet or doublet) in the spectrum. These peaks are usually located at slightly different positions. The intensity ratio between the peaks representing different final states is defined by the ratio of probabilities of occurrence of these states. An example of multiple final states is Ce 3d and Ce 4d core-level spectra shown in Fig. 2.7 with the indication of Ce^{4+} and Ce^{3+} contributions according to Refs. [80, 81].

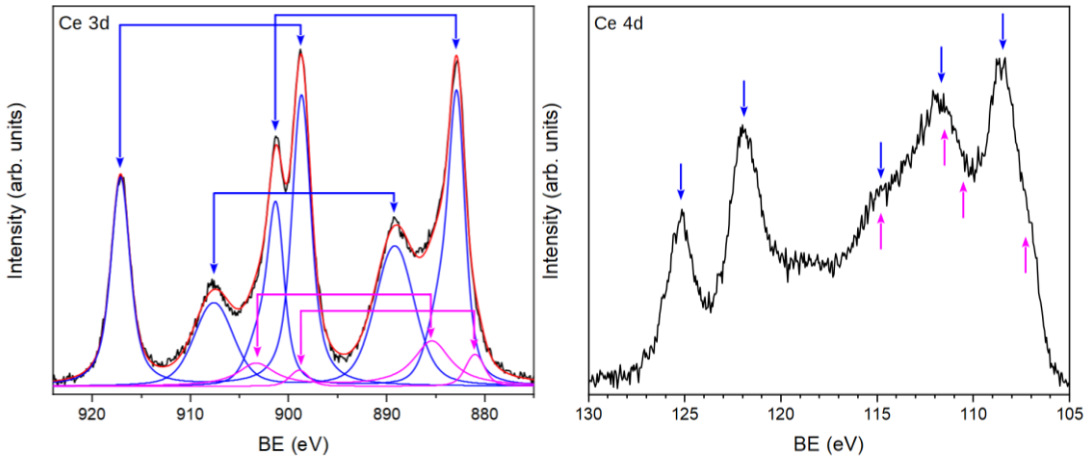

Figure 2.7: XPS Ce 3d (left) and 4d (right) core level spectra acquired at photon energy 1486.6 eV and 490 eV, respectively. Ce^{4+} contributions are indicated by blue arrows and Ce^{3+} by purple arrows.

Besides photoelectron peaks, inseparable components of the PES spectrum are Auger peaks. When the atom is ionized by emission of the core level electron, another electron from a higher energy level may fill this hole. Excessive energy can be released in the form of radiation (i.e. fluorescence) or it can be spent for excitation and emission of the third electron called Auger electron (Fig. 2.8) Therefore, the Auger process is a three-step-process and the kinetic energy of the Auger electron is independent of the incident photon energy and depends only on the energy difference between electronic orbitals involved. Thanks to this particularity, the origin of the peak can be distinguished by changing the energy of initial radiation: in the binding energy scale the position of photoelectrons' signals does not change, but Auger peaks are shifted.

Photoelectron peaks are marked with the chemical symbol of the element followed by the number of the electronic level (defined by principal quantum number), orbital type (defined by angular momentum quantum number) and total momentum number which accounts for a spin quantum number of the emitted electron. Auger peaks are marked with the chemical symbol of the element followed by three letters describing three electronic levels involved in the process.

Stepwise background in the PES spectrum is created by secondary electrons, which are inelastically scattered multiple times on their route to the vacuum. The background is subtracted during the data processing. The typical wide scan photoelectron spectrum is shown in Fig. 2.9.

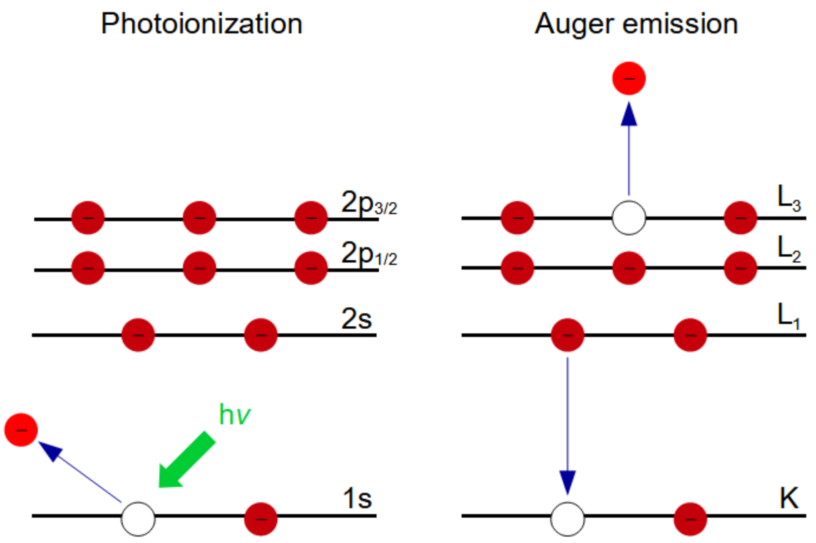

Figure 2.8: Illustration of the Auger process: photoionization of a neutral atom (left) and subsequent Auger emission (right).

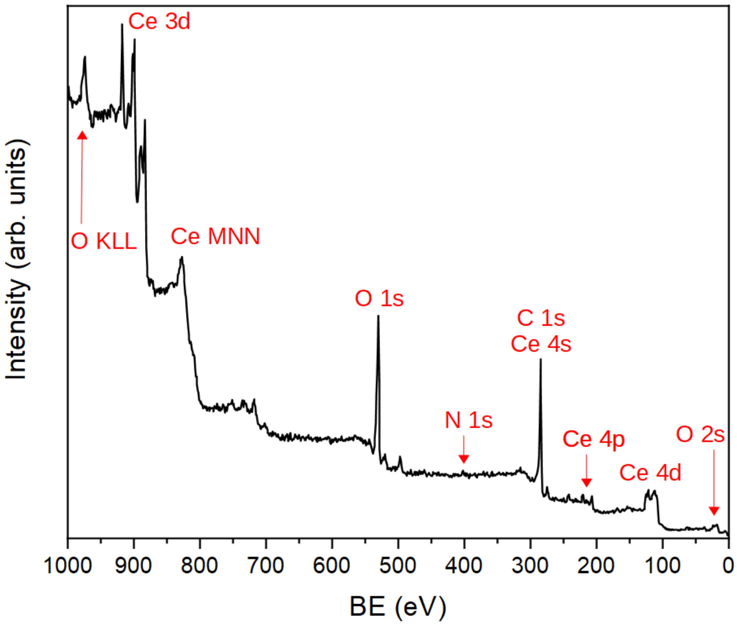

Figure 2.9. The wide scan photoelectron spectrum taken from Ce NPs functionalized by histidine with the assignment of the main features. The excitation energy is 1486.6 eV.

A typical problem during the characterization of the poorly conducting sample by PES is a charging effect, which arises due to the lack of the proper compensation of the electric field created by holes after the photoelectron emission. The charging effect causes the shifting of the peaks to the higher binding energy. If it cannot be eliminated by an electron flux gun or better conductive holder, spectra need to be calibrated according to the binding energy of the known photoemission feature, for instance, the C 1s position of the carbon contaminations. However, calibration is possible just for the spectra acquired with a laboratory X-ray source. When differential charging is present, in the case of synchrotron radiation, various parts of the sample are charged differently, and this calibration method cannot be utilized.

For X-ray photoelectron spectroscopy (XPS), a laboratory X-ray source Specs is used. Al Kα line with a photon energy of 1486.6 eV is employed due to its narrow energy width [82]. The measured kinetic energy of the photoelectrons is then in a range of 100 – 1400 eV, which corresponds to the inelastic mean free path between 0.6 to 2 nm. The information depth is therefore quite small and few surface atomic layers can be analysed in course of the XPS study.

As indicated by the name, synchrotron radiation (SR) is applied as the photon source for synchrotron radiation photoelectron spectroscopy (SRPES). Advantages are the tunability of the photon energy, narrow energy width of the beam and smaller spot size in comparison with a standard laboratory X-ray source. By changing the photon energy, photoionization cross-section and information depth can be tuned. Therefore, by careful adjustment of the photon energy, the highest possible surface sensitivity can be achieved. SRPES also allows performing depth profiling measurements.

2.3.2. Theory and principle of RPES

For resonant photoelectron spectroscopy (RPES) photon energy close to the X-ray absorption threshold of the chosen core level is used. Therefore, a tunable light source is essential. In off-resonance conditions, a photon with energy higher or lower than the resonance energy causes a direct transition of the electron from the substrate to the vacuum. However, when the energy of the incident photon causes the resonance, the excited core-level electron is scattered via Coulombic interaction with a valence electron. As a result, one electron fills the core hole and the second one is emitted from the sample as a photoelectron [83]. An illustration of the resonant effect at the $4d \rightarrow 4f$ photoabsorption threshold for cerium oxide is depicted in Fig. 2.10.

Due to the resonance effect intensity of the photoelectron peak significantly increases. Therefore, this technique also enables examining oxidation states with high sensitivity. It is especially convenient to use RPES when resonant states of the two

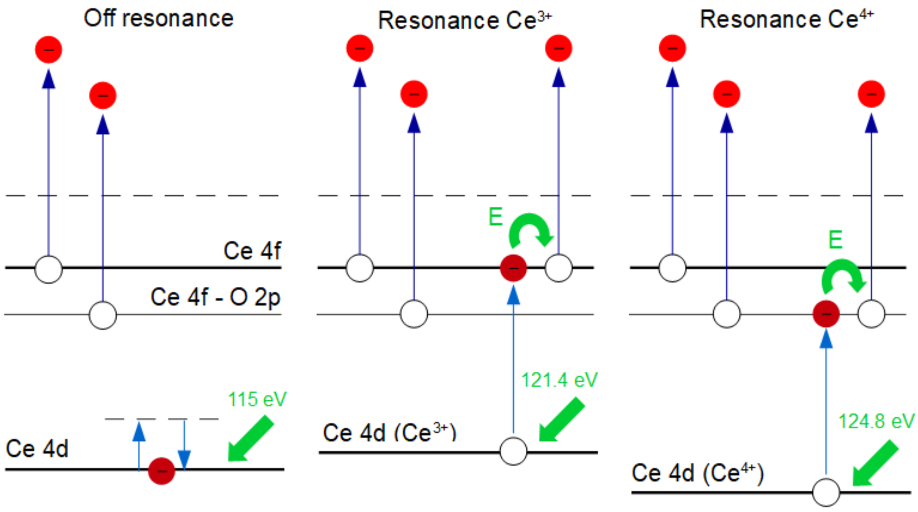

Figure 2.10: Diagram of the resonant effect at the $4d \rightarrow 4f$ photoabsorption threshold for cerium oxide.

oxidation states of the element are distinguishable, as for the Ce $4d \rightarrow 4f$ photoabsorption threshold (Fig. 2.10). When the spectra at the two resonance energies and also at the off-resonance energy are measured, the contribution of the individual states can be analysed (see Fig. 2.11). Moreover, the oxidation state of the surface can be expressed through the resonance enhancement ratio (RER) given as

$$RER = D_1/D_2 \tag{2-5}$$

Here D_1 and D_2 are the intensity differences between on- and off-resonance features in the valence band of the first (Ce^{3+}) and second (Ce^{4+}) oxidation state of cerium cations, respectively [46].

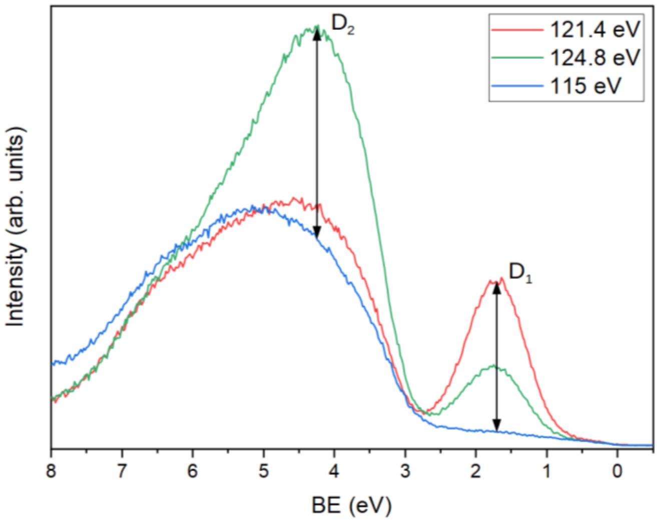

Figure 2.11: Illustration of resonance intensity enhancement determination for VB spectra of cerium oxide.

2.3.3. Theory and principle of NEXAFS spectroscopy

Near edge X-ray absorption fine structure (NEXAFS) spectroscopy is a quite young technique used to study the electronic structure and orientation of molecular adlayers and thin films. Information in NEXAFS is obtained as a dependence of an X-ray absorption intensity on incident photon energy, which ranges from below the X-ray absorption edge to tens of electronvolts after it. Since NEXAFS needs a tunable energy source, the measurements are performed at synchrotrons.

The principle of the technique lies in the excitation of the core level electron to an unoccupied orbital above the Fermi edge using the radiation of sufficient energy. Auger electron or fluorescent radiation is emitted, when the core hole is refilled, and then can be detected. Partial Auger yield NEXAFS is commonly used for studies of atoms with low atomic numbers. For these atoms, the relaxation of the system through the Auger process is far more substantial than through fluorescence. Furthermore, indirect information about absorption can also be obtained by the measurement of inelastically scattered electrons (secondary electrons) [84].

There are several characteristic features in a NEXAFS spectrum as shown in Fig. 2.12. A step-like intensity increase in the spectrum corresponds to the moment when the incident photon energy exceeds the ionization threshold. Excitation of a core-level electron to a bound state occurs when the photon energy equals the energy difference between the initial (occupied) and final (unoccupied) orbital. A core level electron can transit into antibonding orbitals of π^* or σ^* character, or into the Rydberg states [85]. The π^*-states are the lowest unoccupied molecular orbitals for diatomic structure with π bonds and are usually located below the ionization threshold. When the transition from the 1s level to π^* orbital occurs, it is called π^*-resonance transition. As π orbitals correspond to double or triple bonds, this type of resonance cannot arise from single-bound systems. Between π^*-states and the ionization edge, the Rydberg states can be found [85]. The π^* and Rydberg resonance transitions are represented as sharp peaks in the NEXAFS spectrum due to the short lifetime of excited electrons. However, the Rydberg resonances are usually quite weak, particularly when the chemisorbed molecules or condensed phase are measured. The σ^*-states are located above the ionization edge and transitions to these states are shown as wide features in the NEXAFS spectrum.

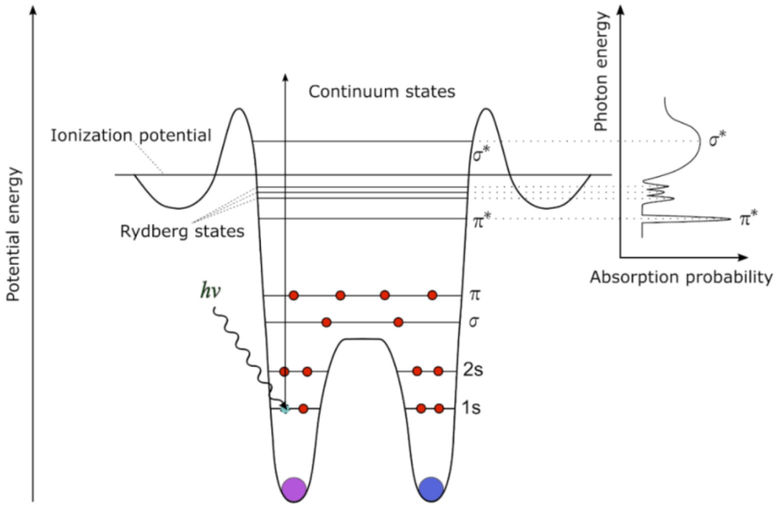

Figure 2.12: Illustration of the potential of a diatomic molecule (left) and corresponding NEXAFS K-edge spectrum (right) [64].

NEXAFS can also provide information about the orientation of molecules adsorbed on a surface because intensities of π^* and σ^* resonances are dependent on the angular orientation of incident radiation's electric field vector with respect to corresponding molecular bonds [86]. The highest intensity of resonance is measured when the electric field vector is parallel to the orbital of the final state and on the contrary, the resonance peak disappears when they are perpendicular. The σ orbital is oriented along the bond axis and the π orbital is perpendicular to it. Therefore, when the NEXAFS spectrum is measured at both grazing and normal incidence, the spatial orientation of the molecule can be determined according to the relative intensity changes of π^* and σ^* resonances.

2.3.4. Instrumentation, measurement and data processing

A typical experimental setup for PES (Fig. 2.13) consists of a source of radiation, a vacuum chamber with a grounded sample, an electron energy analyser and a detector. According to the used radiation source, several types of PES can be classified. Nowadays the most widely used electron energy analyser for PES is a hemispherical analyser (HMA). It consists of two concentric conductive hemispheres on which voltages of opposite signs are applied. The hemispheres serve as electrodes creating an electric field which bends the trajectory of electrons passing through the space between the hemispheres.

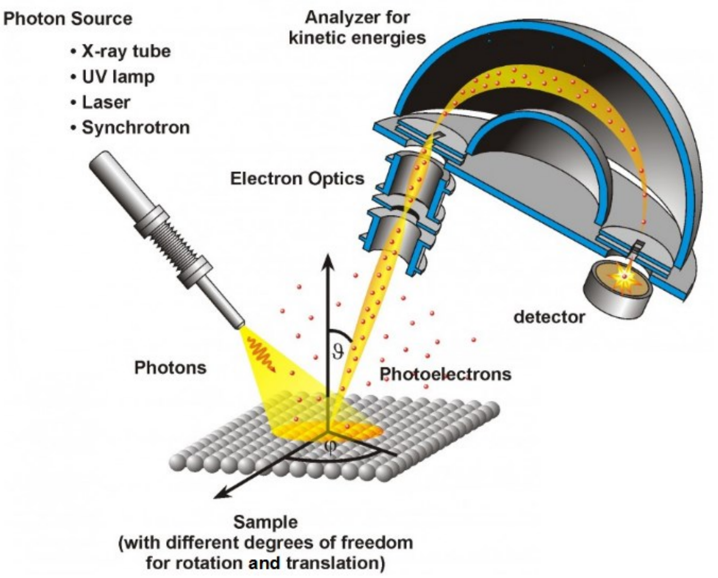

Figure 2.13: Illustration of the typical experimental setup for photoelectron spectroscopy. Taken from [87], modified.

At specific applied voltage, only electrons with suitable kinetic energy called pass energy have a trajectory with the right radius to pass through the HMA to the detector. Usually, the hemispheres' voltages are held fixed and incoming electrons are decelerated to pass energy by electrostatic lenses located between the sample and the entrance slit of the analyser. HMA can operate in two basic modes: constant retarding ratio (CRR) and constant analyser transmission (CAT). The latter mode is more widely used for PES measurements, as it provides constant energy resolution across the whole spectrum. In this mode, all electrons are retarded to the same fixed pass energy by suitable retarding potential chosen automatically according to the expected kinetic energy of the measured photoelectrons.

PES (XPS, SRPES, RPES) and NEXAFS data were measured at the Materials Science Beamline (MSB), Elettra Synchrotron, Trieste, Italy. Elettra is a third-generation synchrotron providing ultra-bright radiation with high intensity ranging from infrared to X-rays [88]. Radiation is produced by electrons circulating in the storage ring at the moments when they are passing through bending magnets, wiggles or undulators. They deflect the trajectory of the electrons substantially and the deceleration of charged particles makes them radiate. Electrons are generated in the linear accelerator and accelerated into the booster, from where they are injected into the storage ring when needed [89]. Elettra operates 28 beamlines, which utilize produced radiation delivered to specific experimental end-stations through vacuum optical systems.

The photon beam of the MSB is produced by the bending magnet and is mostly linearly polarized in the horizontal direction. The optical system delivering radiation from the magnet consists of a prefocusing mirror, an entrance slit, a monochromator used to set the photon energy, an exit slit, a refocusing mirror and a gold mesh used to measure the photon flux before entering the end station. The end-station consists of several vacuum chambers separated by gate valves – a load lock, top and bottom preparation chambers and an analysis chamber. A sample is inserted into the load lock, sample modification can be done in the preparation chambers and measurements are carried out in the analysis chamber in an ultra-high vacuum (10^{-10} mbar). The available photon energy range is from 22 to 1000 eV, which is classified as a soft X-ray [90]. The beam spot is approximately a few hundred μm. Hemispherical electron energy analyser Specs Phoibos 150 is employed [91].

In the beginning, after the glassy carbon (GC) substrate cleaning procedure, the core levels of Ce 3d, O 1s, C 1s, N 1s, Na 1s and Cl 2p were acquired for each substrate to check its cleanliness. The exact photon energy was defined by measuring the Fermi edge of a Ta holder.

All the samples of Ce NPs were measured as soon as possible after their preparation. The measurement procedure of each sample consisted of several steps. After alignment for the best signal, SRPES including RPES data were acquired. Then it was followed by NEXAFS, after which RPES and SRPES N 1s measurements were repeated. The last step was to measure XPS and then another RPES was performed.

By SRPES, C 1s, Cl 2p (in case of acidic samples), N 1s, Ce 4d and O 1s core-level spectra were acquired. Photon energies of 410, 490 and 630 eV were used, with total resolution 0.36, 0.44 and 0.63 eV, respectively. For each sample, RPES measurements were performed several times at different stages of the measurement process, so that influence of individual factors on sample reduction can be determined. RPES measurements included acquiring of series of valance band spectra with photon energies 121.4 eV (resonance of Ce^{3+}), 124.8 eV (resonance of Ce^{4+}) and 115 eV (off-resonance). Na 1s (only in case of basic samples) and Ce 3d core level spectra were measured by XPS. By NEXAFS, the N K-edge spectrum was measured in partial Auger yield and Ce $M_{4,5}$-edge and O K-edge spectra were obtained from partial secondary electrons signal.

PES and NEXAFS data were processed using the software KolXPD 1.8.0 [92]. Spectra measured using synchrotron radiation needed to be corrected to the real value of the used photon energy. Therefore, exact photon energy was determined from the measured Ta valance bands. Then according to these values, energies in corresponding SRPES and NEXAFS spectra were corrected. In the next step, all SRPES spectra were normalized by mesh current. The next treatment was a subtraction of background, which applies to both SRPES and XPS data. In C 1s, O 1s, Ce 4d and Ce 3d spectra, the Shirley background was used. The linear background was subtracted only in N 1s spectra because they were very noisy. XPS Ce 3d spectra were fitted as shown in Fig. 2.7, left, in order to determine the stoichiometry of the cerium oxide NPs. Triplets of corresponding RPES spectra (Fig. 2.11) were compared to calculate RER values. NEXAFS spectra after the photon energy correction were divided by mesh current. To compare O K-edge and Ce $M_{4,5}$-edge spectra among all three samples CO, CH and CG, the data were processed as follows. A constant was subtracted from each spectrum, so there is zero intensity at the lowest photon energy. Then each spectrum was divided by a constant, so the intensity at the highest photon energy is equal to one. Finally, the spectra were normalized according to intensity of the peak at 533 (O K-edge spectra) and 884 eV (Ce $M_{4,5}$-edge spectra). N K-edge spectra of sample CH were obtained as follows (and the same applies to sample CG). The corresponding background signal of the sample CO with the same pH recorded under identical conditions was subtracted from the NEXAFS N K-edge spectra recorded on sample CH. The resulting spectra of sample CH at various pH were normalized to the intensity of the highest peak for better comparison.

2.4. Sample preparation

Original Ce NPs solutions studied in this thesis were prepared by the group of Dr. A. Shcherbakov, Zabolotny Institute of Microbiology and Virology, National Academy of Sciences of Ukraine. The solutions were prepared as follows.

3.73 g of $CeCl_3 \cdot 7H_2O$ was dissolved in 100 ml of water. Under intensive stirring drops of the prepared solution were slowly added to the 3 M KOH solution (1000 ml). After 30 minutes of stirring the solution was heated to the boiling point and kept under stirring in these conditions for 3 hours. Then the solution was left at room temperature without stirring for particles to condense. After 24 hours the condensed phase was separated by decantation and dispersed in 500 ml of distilled water. The condensed phase was rinsed in water several times using decantation until the neutral pH of the solution was achieved. Finally, 200 ml of the solution was prepared and ultrasonicated for 20 min. The resulting colloid solution was divided into 4 parts, 50 ml each. Two parts were combined and in this way sample CO (0.05 M colloid solution of Ce NPs) was prepared.

Another two parts were used for the preparation of samples CH and CG as follows. An equimolar amount of amino acids was added into each of the solutions (50 ml) - histidine monohydrochloride monohydrate (523 mg) and glycine (188 mg). The resulting solutions were ultrasonicated for 5 min and then stirred for 2 hours. Then the solutions were left at room temperature without stirring allowing ceria nanoparticles to reach the equilibrium in interaction with biomolecules. After 24 hours, the NPs were separated by centrifugation, then dissolved in 50 ml of distilled water and centrifuged again. The rinsing procedure was repeated 5 times for each sample (CH and CG). In the end, the colloid solution of NPs was mixed with 50 ml of distilled water and ultrasonicated for 20 min. In this way, samples CH (0.05 M colloid solution of Ce NPs functionalised by histidine) and CG (0.05 M colloid solution of Ce NPs functionalised by glycine) were prepared.

2.4.1. Sample preparation for DLS

For the dynamic light scattering measurements, NPs solutions were diluted in order to prepare a slightly opalescent sample with maximum optical density of 0.1. Pure deionized water (prepared by Aqual 29) with a maximum conductivity of 0.05 μS/m was used for the preparation of all DLS samples.

Samples for measurement of ZP at various pH were prepared by dilution of 10 μl of original NPs solution in 1 ml of water. To change the pH of the samples required amount (several μl) of 0.2 M HCl or 0.25 M NaOH was added to the solution, thus the resulting pH of the samples was around pH 4.5 and pH 8.5, respectively. The diluted solution was ultrasonicated for 15 minutes before the measurement.

For titration experiments original NPs solutions CO, CG and CH were diluted with water in a ratio of 30 – 50 μl to 8 ml. The dilution ratio was determined according to the optical density of the original solution. The diluted solution was ultrasonicated for 15 minutes before the measurement.

2.4.2. Sample preparation for AFM

AFM measurements of neutral NPs solutions were performed on three types of samples differing in the preparation procedure. When the liquid above the settled solid part was mixed with water in a ratio of 10 μl to 1 ml, the resulting sample was denoted with *w*. Pure deionized water (prepared by Aqual 29) with maximum conductivity of 0.05 μS/m was used for the preparation of all AFM samples. In this way, samples CO_w and CG_w were prepared. As the original CH NPs solution was more or less homogenous and stable in time, the settled part did not exist and therefore sample CH_w was not prepared. To prepare the second type of neutral AFM samples, every bottle with the original NPs solution was agitated by hand and 2 - 8 μl of NPs solution (depending on the optical density of the original solution) was mixed with 1 ml of water. In this way samples labelled CO, CG and CH were prepared. The process of preparation of the third type of samples is the same as for the second type, but it includes also 10 min of ultrasonication after the dilution of agitated solution with water in a ratio of 2 μl to 1 ml for CO NPs and 20 μl to 1 ml for CH and CG NPs. The resulting samples are denoted with *s*: CO_s, CH_s and CG_s.

Samples of NPs solutions with acidic or basic pH were prepared as follows. Original NPs solutions were agitated. Then 10 μl (for basic sample) or 20 μl (for acidic sample) of NPs solution were mixed with 1 ml of water. Subsequently, a few μl of 0.25 M NaOH or 0.2 M HCl were added to the solution to adjust pH to the required value of around 8.5 or 4.8, respectively. The resulting solutions were sonicated for 10 min and then left to stabilize for approximately 60 min.

In the last step of preparation of all AFM samples, 2 μl of final solution were dropped on freshly cleaved atomically flat mica support, which area is around 1 cm^2, and left to dry. The drying procedure was performed in a way that the dried drop was more or less uniform.

2.4.3. Sample preparation for PESs and NEXAFS spectroscopy

Samples for PESs were prepared by deposition of NPs colloid solutions onto a substrate. As a substrate unpolished glassy carbon (GC) was used. The substrate was cleaned before Ce NPs deposition as follows. At first, GC was heated to 200 °C for 15 min. Then Ar^+ sputtering was performed for 30 min. Then another heating to 200 °C for 15 min followed by 15 min of Ar^+ sputtering was applied. Finally, the substrate was heated to 200 °C for 5 min.

Every type of NPs (CO, CG and CH) was measured at neutral, acidic (around 4.5) and basic (around 8.5) pH. Overall nine samples were prepared. Neutral samples were prepared as follows. 200 μl of original NPs solution was added to 800 μl of Milli-Q water. The pH of the resulting solution was measured by pH indicator papers and then the solution was ultrasonicated for 10 min. After that 1 drop (5 μl) of the solution was deposited on the previously cleaned substrate and left to dry in a desiccator.

Samples with acidic and basic pH were prepared as follows. 200 μl of original NPs solution were added to 800 μl of Milli-Q water and the pH of the resulting solution was measured by pH indicator papers. Then several μl of 0.2 M HCl or 0.25 M NaOH were added to create acidic or basic pH, respectively. The pH of the solution was measured again and the process was repeated until pH around 4.5 or 8.5, respectively, was reached. The amount of added acid or base differed for every sample. The final solution was ultrasonicated for 10 min. Afterwards, 1 drop of the solution was deposited on the previously cleaned substrate and left to dry in a desiccator. Samples were prepared just before they were inserted into a vacuum for the measurements.

Besides the samples mentioned above, in SRPES N 1s and NEXAFS N K-edge spectra, we display also the spectra of the sample named CH pH 6.7 2020. These spectra are shown because they are the best spectra of sample CH which we got during all performed measurements. The sample CH pH 6.7 2020 was prepared as follows. Original CH NPs solution was diluted with Milli-Q water in a ratio of 1 to 4. The resulting solution was left in an ultrasonic bath for 10 min. Then 1 drop of the solution was applied to the prepared GC substrate and left to dry in a desiccator for approximately 10 min.

3. Results

3.1. Dynamic light scattering

3.1.1. Measurement of zeta potential at different pH

If we inspect samples from the visual perspective, samples CO and CG sediment with passing time, but sample CH remains visually uniform over at least several months.

In order to determine the colloid stability of samples in various environments, the ZP of samples CO, CG and CH were measured at acidic, neutral and basic pH. As samples CO and CG were measured in deionised water, their pH was in the range of pH 6 to 7, due to the equal amount of positive and negative ions (originating utterly from water molecules). In the case of sample CH, the solution had a pH of 7.0 and it was measured after one round of titration with very low conductivity. The increased number of ions in the sample CH allowed us to determine pH more precisely. Detailed preparation of the samples for these measurements is described in Subchapter 2.4.1. Measurement procedure and data processing are described in Subchapter 2.1.2. The resulting average values of ZP and their deviations are written down in Table 3.1.

	Acidic			Neutral			Basic		
Sample	pH	ZP [mV]	ΔZP [mV]	pH	ZP [mV]	ΔZP [mV]	pH	ZP [mV]	ΔZP [mV]
CO	4.8	34.7	3.1	6 - 7	12.3	4.2	8.8	-55.4	2.9
CH	4.8	42.7	6.0	7.0	-53.8	4.7	8.3	-56.6	5.4
CG	4.8	39.1	4.3	6 - 7	-17.7	6.9	8.9	-56.2	5.8

Table 3.1: Zeta potential of samples CO, CH and CG in acidic, neutral and basic pH. ΔZP is a deviation of the mean ZP value.

From Table 3.1 follows, that all samples have positive ZP at pH 4.8 and negative ZP at higher pH than 8.3. At neutral pH, ZP values differ significantly among the samples. This is connected to different surface modifications. At neutral pH, samples CO and CG are unstable as their absolute value of ZP is lower than 20 mV, which means they tend to agglomerate easily. On the contrary, sample CH has a quite high absolute value of ZP at neutral pH. As the pH of this sample was changed by NaOH, $-OH^-$ groups adsorbed on the NPs decreased their ZP. However, the ZP value of -53.8 mV is even lower than the values from the titration curves of sample CH shown further in this Subchapter, which are around -40 mV. It is probably a result of a longer time for stabilization after the pH change (several days in this case compared to several minutes in titration measurements).

We can also analyse ZP distributions from which the mean ZP values and their deviations in the Table 3.1 were determined. ZP peaks of sample CO were symmetrical single peaks at all measured pH values. Thus, only one type of NPs is present in this sample, which are in an equilibrium with surrounding ions of colloid solution, resulting in similar ZP characteristics. For sample CH some of the measured ZP peaks were not particularly uniform and symmetric, mainly in an acidic environment. This reflects nonuniformities in the sample, which arise from the fact, that the number of histidine molecules per particle surface can vary. In any case, ZP peaks of repeated measurements in a certain environment overlapped in at least 90% of their area. Therefore, the resulting mean ZP of the sample was calculated as an average of the individual mean ZP values. ZP peaks of sample CG were uniform and symmetric single peaks in acidic pH. However, we saw significant asymmetry of the ZP peak in both neutral and basic pH and in some cases even several peaks were identified in the ZP distribution. Similarly to sample CH, peaks overlapped quite well, in at least 90% of their area. However, in neutral pH, all ZP distributions had minor contribution on the right side of the main peak, in the positive ZP region, as can be seen in Fig. 3.1. Free glycine molecules should not be present in the sample and we do not expect any other significant impurities either. It indicates, that there are NPs with different ZP characteristics present in the sample CG at neutral pH. Probably, the difference is in the measure of the glycine surface coverage or orientation. The majority of NPs had a mean ZP value of around -19 mV, but there was a part of the NPs which had positive ZP with a mean value of around 14 mV.

From the determined ZP values in Table 3.1 we see, that all samples have quite a good colloid stability at pH 4.8 and relatively high colloid stability above pH 8.3. Higher colloid stability means better distribution of individual NPs in the solution, which can be utilized for the preparation of more uniform layers of dried NPs from solutions.

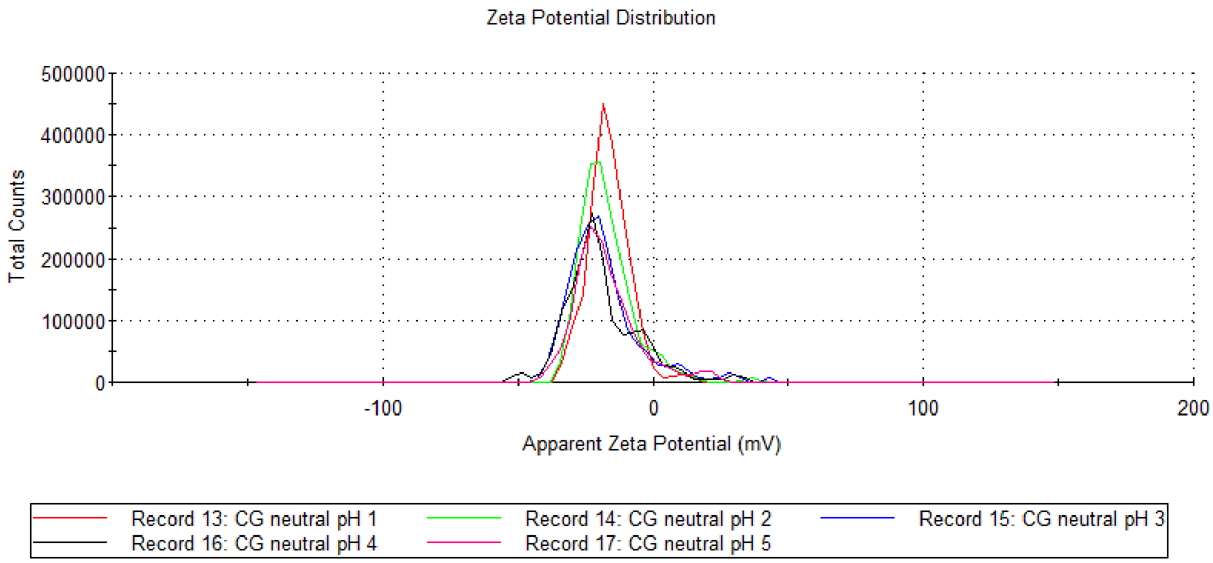

Figure 3.1: Measured ZP distributions of sample CG in neutral pH.

3.1.2. Titration measurements

3.1.2.1. Sample CO

3.1.2.1.1. Titration to acid

In Fig. 3.2 we can see titration curves of the CO sample in to acid direction. At the beginning of the 1st round, a quite large amount of NaOH was added to the sample but the pH was not changing. This situation means, that the sample behaves as a buffer and adsorbs or compensates for the ions added to the solution. Most probably the added –OH^- groups were neutralized by hydrogen ions present in the sample. When added base exceeded a certain amount, the number of –OH^- groups was sufficient to compensate for protons present in the sample and pH rose rapidly from pH 3.7 to pH 6.4. During this change, ZP passed through an IEP around pH 5.5, where the surface polarity of the NPs switched from positive to negative by the change of adsorbed ions. Simultaneously, the conductivity of the sample slightly decreased (Fig. 3.3), which confirms the depletion of H^+ from the solution. A data point was measured after the described change, at pH 6.4. However, software was set to measure data points with the pH step of 0.3 pH unit. Therefore, when the pH got over the target value, skipped data points were still measured afterwards, but without any addition of the titrant. During these measurements, pH was gradually decreasing, as –OH^- groups were slowly neutralized by remaining protons. When software got to the point where pH needed to be increased from pH 4.8 to pH 5.2, buffering occurred again, until pH abruptly jumped to 10.8.

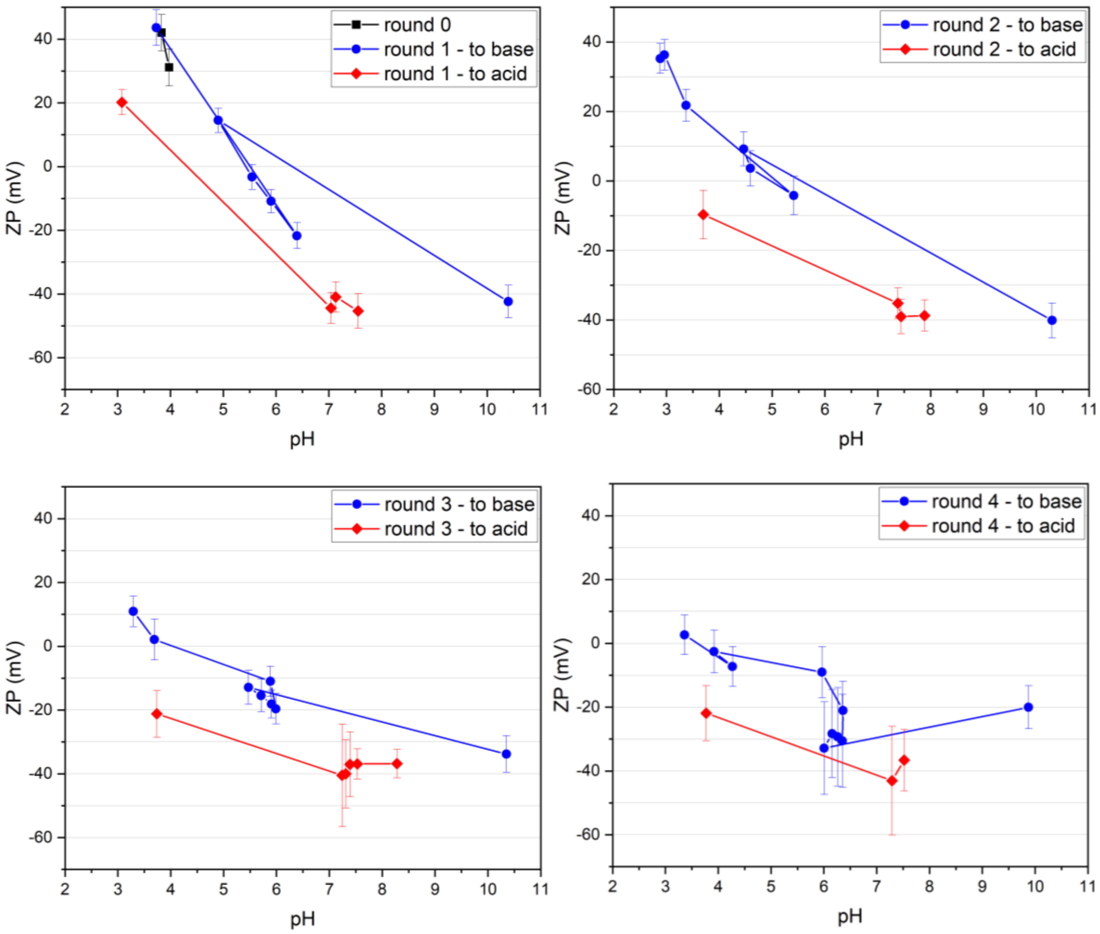

Figure 3.2: Titration to acid of sample CO. Titration curves of the 0th and 1st round (upper left), 2nd round (upper right), 3rd round (bottom left) and 4th round (bottom right).

Then the titration in the direction to acid of the 1st round started. Interestingly, the pH of the sample was decreasing naturally down to pH 7 without adding any acid. That means that $–OH^-$ groups were gradually neutralized by the sample, but it took longer than was the time interval left for achieving the equilibrium after the pH change. A pH drop from pH 10.3 to pH 7.6 took around 30 minutes. Then pH decreased by 0.4 pH units in around 20 min. After another 20 min, pH decreased only by 0.1 pH units. During the next addition of an acid, the sample buffered again until another sudden pH change from pH 7.0 to pH 3.0 occurred. Therefore, the sample reached pH

3.0, which was out of the desired range and could damage Ce NPs, according to Ref. [93], as Ce NPs are not stable at pH below 4. During this change sample passed through an IEP, which was lower than in the direction to base – IEP point had a value of 4.3 compared to the previous value of 5.5. Simultaneously, the conductivity of the sample rapidly increased (Fig. 3.3).

2nd and 3rd rounds of the titration had a very similar course as the first one. Titration curves in directions to acid and to base did not overlap within the error bars, which means sample CO shows hysteresis. We can see that titration curves were flatten with increasing the number of rounds. While the ZP range within the 1st round was from 40 mV to -45 mV, in the 3rd round the ZP was ranging only from 10 mV to -40 mV. Simultaneously, the position of IEP decreased as well in both directions of the titration. We can see, that in the region of basic pH, the value of ZP did not change that much within the titration. The 4th round of the titration had a similar pattern as the previous rounds, with the difference in the sudden increase of ZP at the end of titration in the direction to base. This indicates that the sample was affected by the titration.

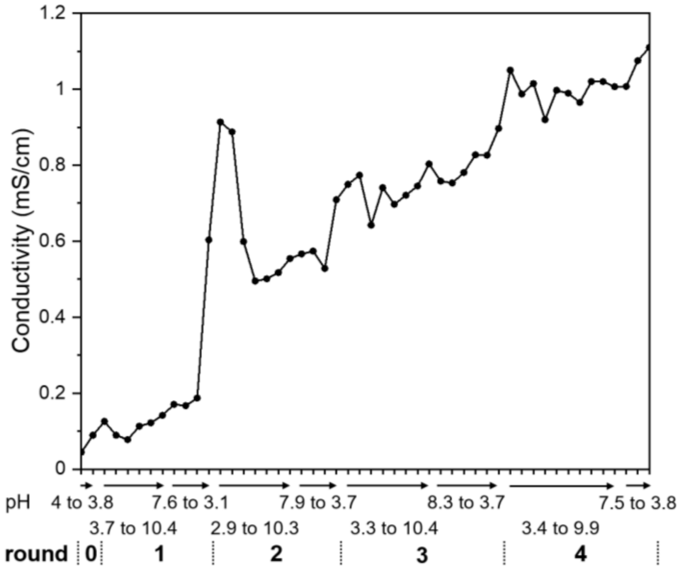

Figure 3.3: Conductivity of sample CO during titration to acid.

As the titration curves flattened, IEP moved to lower pH values and the achieved ZP range decreased during the titration, sample CO was changed during the measurement. A gradual decrease of ZP around pH 3.5 during titration means that NPs' sorption capacity for positive ions was reduced. However, as the ZP around pH 8 did not change, the sorption capacity for negative ions remained more or less stable.

Therefore we assume, that part of the negative –OH$^-$ groups which adsorbed on the NPs in the basic pH was adsorbed irreversibly and blocked some adsorption sites for hydrogen cations even in acid pH. A decrease in IEP also agrees with this assumption, as according to Ref. [94] adsorption of negative ions on the Ce NPs moves IEP to lower pH values. Hysteresis of the titration curves shows, that sample was titrated too fast for the equilibrium to be reached after the pH change. Therefore, the titration curves are direction-dependent.

A significant increase in conductivity at the end of the 1st round (Fig. 3.3) was caused probably partly by the addition of a large amount of acid, but also by the desorption of ions from the NPs' surface due to passing the IEP. This increase was followed by a substantial decrease during the first half of the titration to base of the 2nd round, so the ions from the solution were adsorbed back on the NPs' surface. Such a major peak in conductivity was not expected during the titration and was a sign of some important process. When pH changed from pH 7.0 to pH 3.0, the size of the NPs clusters increased from 500 nm to 1200 nm, which could have decreased the number of adsorption sites. After a few minutes, the clusters' size decreased back to approximately 550 nm while ZP increased from 20 to 35 mV and conductivity increased from 0.6 to 0.9 mS/cm. It seems, that at pH 3 big NPs clusters partially decomposed, by which new adsorption positions were revealed and subsequently occupied by hydrogen cations increasing ZP.

3.1.2.1.2. Titration to base

In Fig. 3.4 results of titration to base of sample CO are displayed. Titration curves of sample CO in the 0th and 1st round show no hysteresis, while ZP changed almost negligibly in the measured pH range, just between -60 to -40 mV. In the 2nd round, ZP at pH 4 was slightly higher, reaching a value of -30 mV. ZP at pH 9 remained around -60 mV. The titration curve of the 2nd round in the direction to acid was shifted even a bit higher, approximately about 15 mV, compared to the previous one in the direction to base, creating small hysteresis. This shift was probably caused by the stay of NPs in an acidic environment for more than 15 hours due to the night break during the experiment. When we look at the measured average size of the clusters, at the beginning of the titration we started with 1000 nm, but during the measurement the size gradually decreased down to 330 nm at the end of the direction to acid of the 2nd round. During the night break, bigger clusters with around 660 nm in diameter were created. However, during the titration in the direction to base in the 2nd round size decreased back to 380 nm.

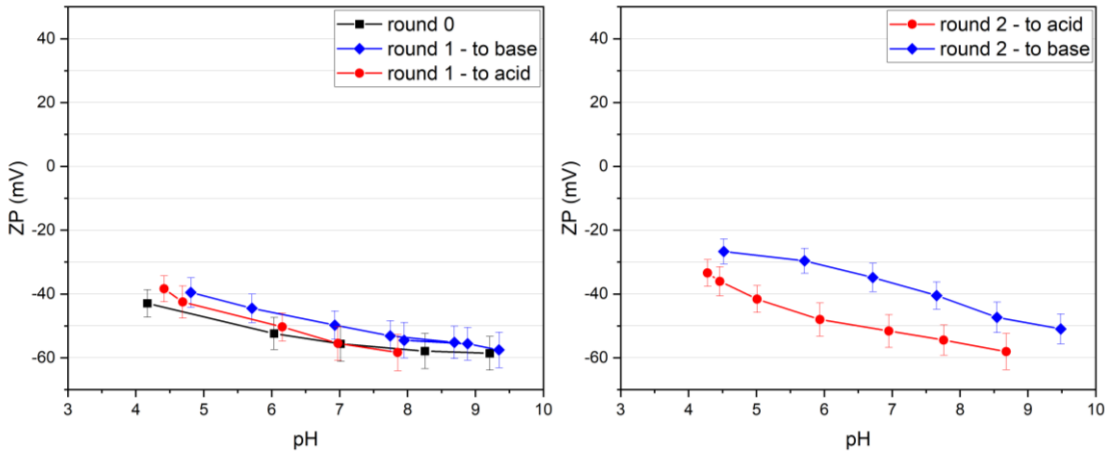

Figure 3.4: Titration to base of sample CO. Titration curves of the 0th and 1st round (left), and 2nd round (right).

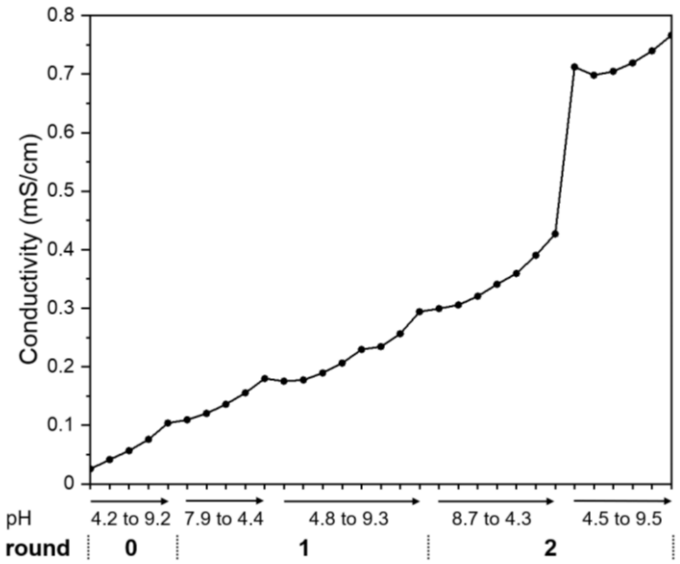

Figure 3.5: Conductivity of sample CO during titration to base.

The conductivity of the sample CO during titration to base shown in Fig. 3.5 was increasing almost linearly. A major increase at the end of titration in the direction to acid of the 2nd round corresponds to the interruption of the measurement during the night, as this titration needed to be performed half-manually. In the graph of conductivity, we can also see very subtle “waves” – a decrease of conductivity at the point of reversal of direction of titration, after which the conductivity increase continued. This effect is due to the partial neutralisation of ions of one type in the solution by ions with the opposite charge desorbed from the NPs at this point.

Since in the 1st round the titration curves overlapped very well (Fig. 3.4, left), titration did not cause any change in the behaviour of sample CO. However, in the 2nd round, the ZP range increased compared to the 1st round and a hysteresis emerged. From this follows, that more H^+ were adsorbed on the NPs' surface, so the sorption capacity for positive ions had increased. This increase was probably connected to the higher accessible surface area of NPs, which was revealed by breaking the big NPs clusters into the smaller ones during the titration, as follows from the size measurements. When the sample was left at pH 4.3 overnight, the NPs had more time to reach equilibrium. It seems, that part of the hydrogen cations from the solution adsorbed on the NPs, resulting in the increase of ZP and decrease of pH. A significant increase in the conductivity during the night was probably caused by the desorption of negative ions from NPs to the solution. At the same time, the size of the clusters increased, therefore probably more ions were released due to lowering the number of adsorption positions on the NPs clusters' surface.

3.1.2.1.3. Comparison of CO titrations to acid and to base

When we compare titration curves of sample CO from titrations to acid and to base, we can see they differ in the range of ZP and behaviour during the titration. While in the 1st round in the titration to acid ZP ranged from 40 to -40 mV (Fig. 3.2, top left), which agrees with the ZP range in the Ce NPs' titration curve in Ref. [94], in the titration to base the range of ZP was between -40 to -60 mV (Fig. 3.4, left). Hysteresis was present in all rounds of the titration to acid and the curves were flattening during the measurement. However, there was no hysteresis in the 1st round of titration to base and the curves were quite flat but in the 2nd round, hysteresis emerged together with an increase of ZP range to -25 to -60 mV. As was discussed above, adsorption capacity for positive ions decreased during the titration to acid, but increased during titration to base. This opposing behaviour can have several reasons.

One possible cause of dissimilarities can be different starting directions. However, what has the bigger influence on the changes in surface chemistry is going over the IEP point. We saw, that in titration to acid sample crossed IEP in every titration round, unlike in titration to base, when the IEP was never reached. When the sample did not go over the IEP, no major change in surface polarity happened. Therefore, the sample in titration to base was modified more slowly than in the titration to acid. Also, these two titrations were performed with a year time gap between them and during this time original CO solution could have undergone some change. This seems to be the case, as already the starting point of the 0th round had different ZP in each measurement (31 mV and -43 mV in to acid and to base titration, respectively), although the starting pH was around 4.1 in both cases.

Another difference between the two titrations is, that in the titration curves of titration to base we do not see abrupt jumps in pH as in the case of titration to acid. However, this is only due to performing the titration to base half-manually, so that pH was adjusted more carefully. A common feature of both titrations is quite similar negative ZP value at pH 9, around -50 mV, which means the sample CO has quite good colloid stability at this pH. Additionally, this characteristic seems to also be stable in time, at least within the 21 hours of titration.

3.1.2.2. Sample CH

3.1.2.2.1. Titration to acid I

Results of the 1st titration to acid of sample CH are shown in Fig. 3.6. Several data points around pH 4.4 at the beginning of the 1st round show extensive buffering of the sample when we tried to increase pH 4.2 by about 1 pH unit. Titration was stopped and restarted twice due to buffering, and at each start, one data point was measured. Then, finally, a sufficient amount of base solution was added to the sample to overcome buffering. Required excessive addition of titrant is reflected also in the conductivity function in Fig. 3.7 as a steep increase. However, when pH finally moved, it suddenly jumped from pH 4.5 to pH 9.5, by which the upper threshold value was already reached. Another buffering occurred at pH 6.3 in the direction to acid of the 1st round. At this pH buffering is expected, as histidine has the strongest buffering properties in the pH range of 5.5 to 7.4 [95]. During transition via IEP, negative ions adsorbed on the NPs' surface were released into the solution, which, together with the addition of acid, led to a significant increase in conductivity (Fig. 3.7).

Due to hysteresis in the 1st round, the position of the IEP in the direction to base (pH 6.9) and to acid (pH 5.2) differed considerably. In the 2nd round buffering occurred around pH 6, where histidine had the strongest buffering effect, and also where the IEP was crossed. As follows from Fig. 3.6, ZP reached values from 50 mV at pH 4 to -55 mV at pH 9. This range was more or less the same in both the 1st and the 2nd round.

The measured size of the clusters started at around 70 nm, but during the experiment, it gradually increased reaching 1400 nm at the end of the measurement. Local significant increase occurred mainly around the IEP, while in the 2nd round the average size reached 3000 nm.

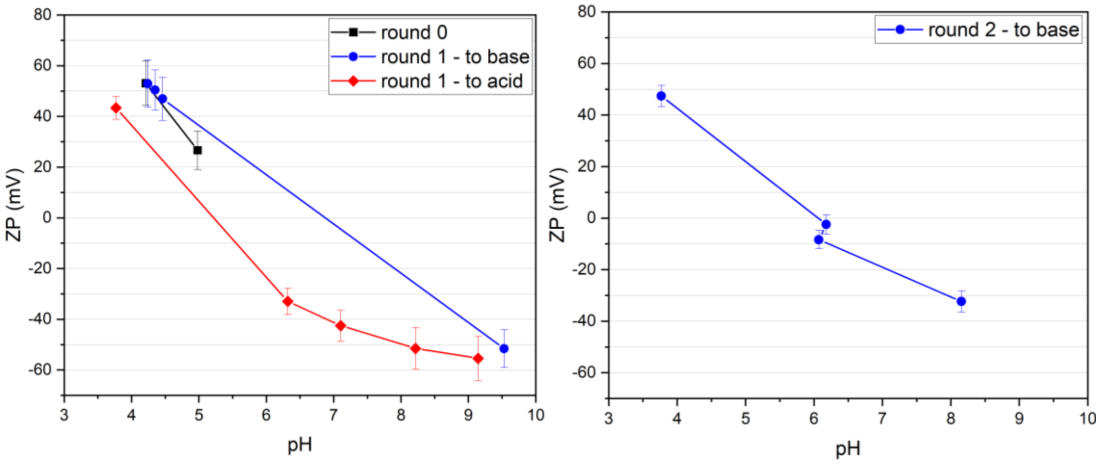

Figure 3.6: First titration to acid of sample CH. Titration curves of the 0th and 1st round (left), and the titration in the direction to base of the 2nd round (right).

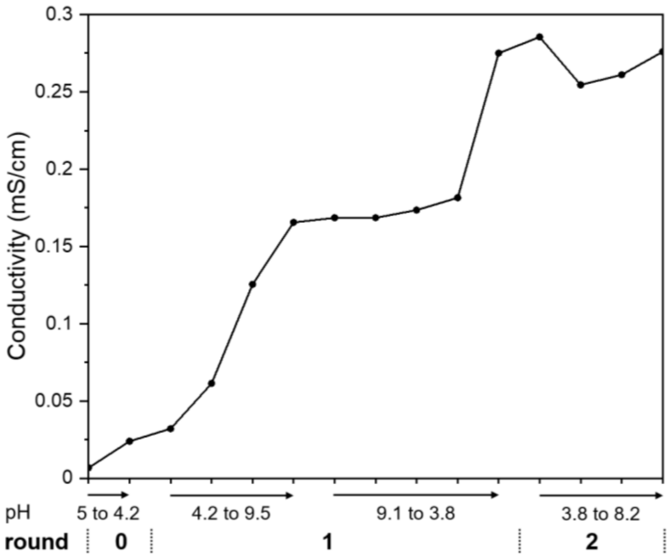

Figure 3.7: Conductivity of sample CH during the first titration to acid.

3.1.2.2.2. Titration to acid II

Results of the second titration to acid of sample CH are shown in Fig. 3.8. During this titration, buffering of the sample was not observed but it was probably due to careful manual adjustment of pH, where we added a sufficient amount of titration solutions to avoid big pH jumps. ZP ranged from 60 to -50 mV in the 1st round, but only from 40 to -50 mV in the 3rd round, so the insignificant flattening of the titration curves occurred. Minor hysteresis is present in the graphs, so the IEP values in the direction to base and to acid are different. However, IEP remained more or less at the same pH during the whole titration in both directions, with the value around 6.3 in the direction to base and 5.3 in the direction to acid.

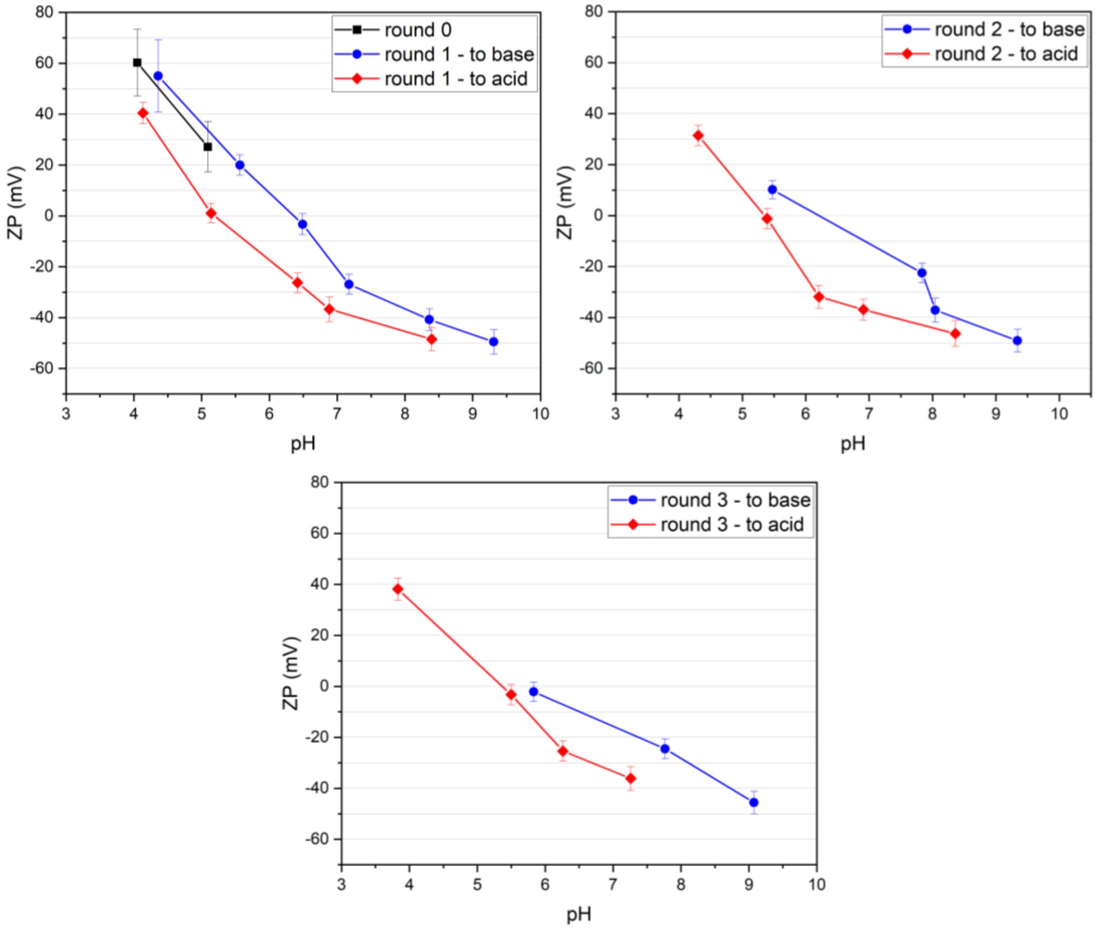

Figure 3.8: Second titration to acid of sample CH. Titration curves of the 0th and 1st round (upper left), 2nd round (upper right) and 3rd round (bottom).

A linear increase in conductivity of the sample CH during the second titration to acid is displayed in Fig. 3.9. In the course of the conductivity function, we can observe “waves” (as in the case of titration to base of sample CO described above), each corresponding to the one titration part, as indicated in the caption of the *x*-axis. These are connected with releasing and capturing ions to and from the solution by NPs when the direction of titration changes.

The size of the clusters at the beginning of the titration was around 60 nm, but it was gradually increasing during the titration. Around every IEP size locally significantly increased up to 4000 nm. These big clusters partially separated when ZP in absolute value rose, but not back to the size before the aggregation. As this process was repeated several times, at the end of the measurement average size of the clusters was approximately 2000 nm.

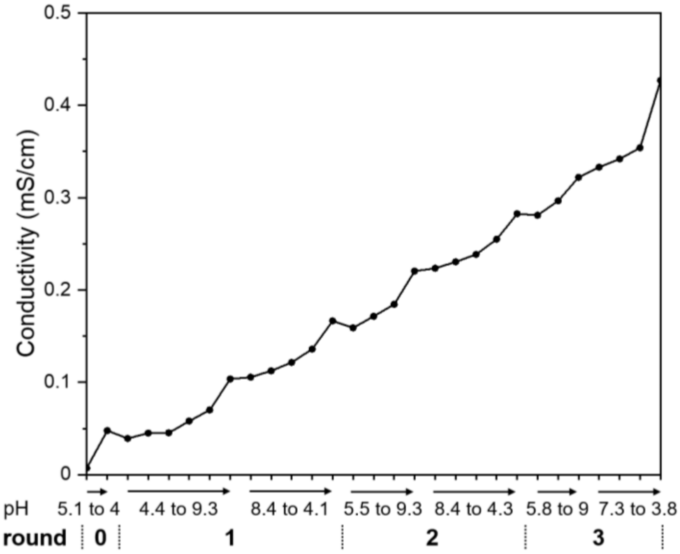

Figure 3.9: Conductivity of sample CH during the second titration to acid.

3.1.2.2.3. Comparison of CH titrations to acid I and II

Results of the two titrations to acid of the sample CH are in good agreement. The range of reached ZP values is virtually identical, between 60 and -50 mV in the 1st round. As the border ZP values are higher than 30 mV in absolute value during both titrations, colloid stability of sample CH is quite high at both pH 9 and pH 4. In both titrations, there was a small hysteresis of the titration curves, which flattened a bit during the measurement. This flattening is probably connected to the increase of the average clusters' size described in detail above, caused by repeated transition via IEP. As the clusters merged, the number of adsorption sites on their surface decreased, therefore the range of achievable ZP became smaller. Despite these changes, the position of the IEPs did not change much during the measurements and remained around pH 6.2 in direction to base and around pH 5.2 in direction to acid for both to acid titrations.

3.1.2.2.4. Titration to base

In Fig. 3.10 titration curves of sample CH during titration to base are displayed. Buffering of the sample was not observed during the measurement, probably because it was performed half-manually. The range of ZP was from 40 to -52 mV in the 1st round, but it was slightly lower in the 2nd round, ranging from 30 to -50 mV. There was a small hysteresis in the titration curves, which practically did not change between the 1st and 2nd round. The position of the IEP following from the titration to base (pH 6.5 in the 0th round) was higher than from the titration to acid (pH 5.3 in the 1st round). However, these values gradually decreased during the measurement, as can be seen in Fig. 3.10. In the 2nd round, IEP in direction to base was at pH 5.6 and in direction to acid at pH 4.9. Conductivity was increasing quite linearly during the whole measurement, as shown in Fig. 3.11. We can see "waves" corresponding to the release of adsorbed ions from NPs' surface to solution and subsequent adsorption of another type of ions at every change point of titration direction.

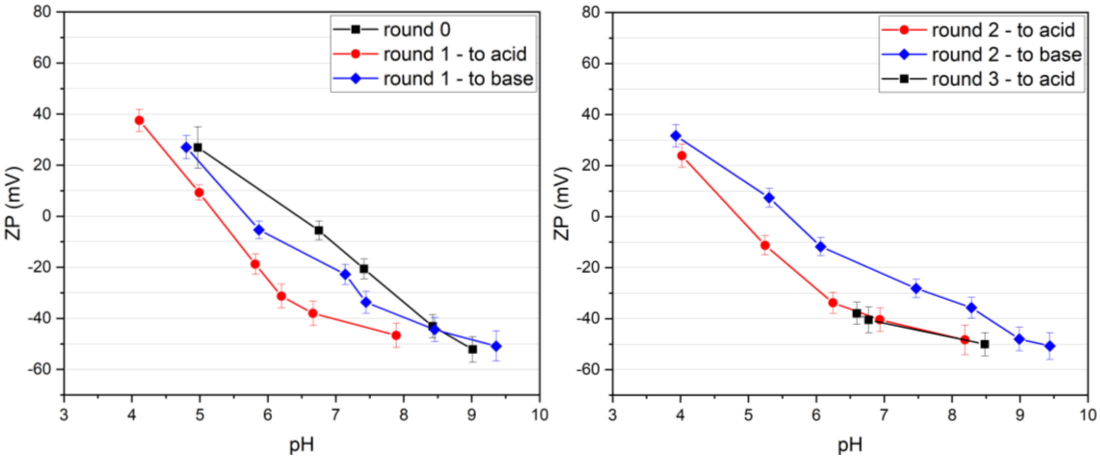

Figure 3.10: Titration to base of sample CH. Titration curves of the 0th and 1st round (left), and the 2nd and part of the 3rd round (right).

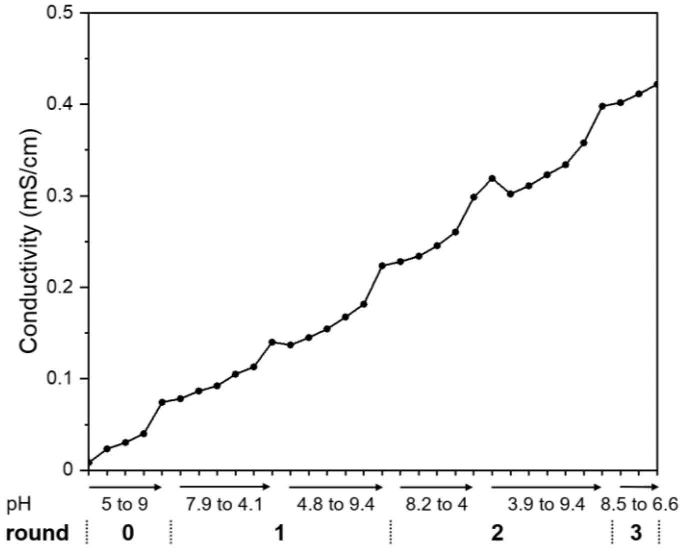

Figure 3.11: Conductivity of sample CH during titration to base.

At the beginning of the titration, NPs clusters had a hydrodynamic diameter of only around 60 nm. However, when pH around IEP was achieved during the titration, clusters agglomerated to structures with a diameter up to 5000 nm. Their size decreased again when an absolute value of ZP increased, but the minimum size was gradually increasing during the measurement. The size of the clusters at the end of the titration was around 840 nm.

ZP at pH 4 slightly decreased from 40 mV in the 1st round to 30 mV in the 2nd round (Fig. 3.10), indicating a subtle decrease in adsorption sites for positive ions during the titration. However, colloid stability of the sample remained high at both minimum and maximum measured pH, as the absolute value of ZP in both cases was higher than 30 mV (Fig. 3.10). The position of the IEP probably shifted to a slightly lower pH too, but we cannot determine this from our data, as the real IEP lies somewhere between the two measured IEPs in the direction to acid and to base, which did not change significantly enough to confirm this assumption.

3.1.2.2.5. Comparison of CH titrations to acid and to base

Now we can compare titrations to acid and titration to base of sample CH. The range of the reached ZP values in the 1st round differs, as in titrations to acid ZP ranges between 60 and -50 mV in the 1st round (Fig. 3.6, left, and 3.8, top left), but in titration to base only between 40 to -50 mV (Fig. 3.10, top left). This range is similar to the range in the 2nd and 3rd rounds of titration to acid (Fig. 3.8). Observing the graphs mentioned above we can notice, that the common event before the decrease of ZP to 40 mV at pH 4 is the transition via IEP, which did not happen before the measurement of ZP in the 0th round of titration to acid. Therefore we assume, that the transition via IEP causes the decrease of the adsorption capacity of the sample CH for hydrogen cations, and so the direction of the titration influences the maximum ZP which can be reached at pH 4. This decrease in the adsorption capacity is probably a result of the not fully reversible agglomeration of small NPs clusters around IEP, as discussed above. The adsorption capacity for negative ions was not influenced, as ZP remained around -50 mV in all rounds of every titration. Despite the modification of NPs clusters by measurement, the absolute value of ZP at both pH 4 and pH 9 was sufficiently high to consider sample CH colloidally stable at these pH values.

Minor hysteresis was present in every measurement and the position of IEPs resulting from the measured titration curves was more or less identical for titrations to acid and titration to base. The conductivity during this titration to base (Fig. 3.11) behaved practically identical to the conductivity of the second titration to acid (Fig. 3.9). They differed from the course of conductivity in the first titration to acid (Fig. 3.7), because it was influenced by sample buffering as this measurement was performed automatically. During the titration experiments of sample CH small NPs clusters (about 70 nm), which were present in the sample at the beginning, agglomerated to bigger clusters with a minimum size bigger than 850 nm.

3.1.2.3. Sample CG

3.1.2.3.1. Titration to acid

Titration curves of sample CG in to acid titration are depicted in Fig. 3.12. There is a number of data points around pH 6 in the 1st round in the direction to base because when pH was changed from pH 4.4 to pH 5.8, several points were skipped, as the set pH step was 0.3 pH unit. Thus, they were measured afterwards without further addition of base to the sample. When the programme got to pH 6 where pH should have been increased again to pH 6.2, the pH rose significantly to pH 8.2, although not much base was added. Then, while skipped points were being measured, pH of the sample was gradually decreasing, slowly reaching equilibrium around pH 6.6. Then this process was repeated several times, creating a lot of data points around pH 8.5. The sample was buffering, but it took several minutes to compensate for ions from NaOH added to the solution. The final pH of 9.5 was difficult to reach, even with the addition of a large amount of base, as the sample was able to compensate for it. This is the expected behaviour of glycine-covered NPs, as glycine is commonly used as a buffer solution and it is the most effective in a range from pH 8.2 to pH 10.6. Glycine exhibits buffering properties also at the pH ranging from 2.2 to 3.6 [95], as in the case of amino acids these ranges lie around its pK values. The extensive addition of base at the end of the direction to base of the 1st round was also reflected in the corresponding part of sample conductivity in Fig. 3.13 as a significant increase.

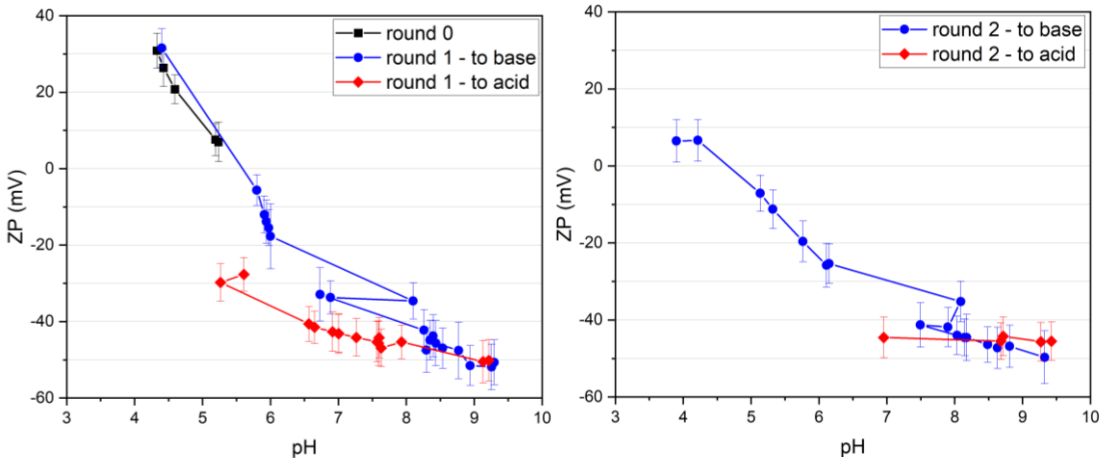

Figure 3.12: Titration to acid of sample CG. Titration curves of the 0th and 1st round (left), and partly of the 2nd round (right).

The first two data points in the direction to acid of the 1st round were measured without the addition of acid, as the pH of the sample was slowly decreasing naturally. Then sample CG buffered again when we wanted to adjust the pH of the sample from 9.1 to 7.9. Several skipped points around pH 7.6 were then measured without adding titrant. An excessive amount of acid was then added to decrease pH from 7 to 6.5, however, the sample was buffering and therefore titration was stopped. After restarting the titration, several data points were measured, but then the sample continued buffering, so the titration was stopped again. Then the situation was repeated one more time. After another restart, the value of pH was suddenly 3.9 (beginning of the 2nd round), which got out of the selected pH range (down to pH 4). Simultaneously, the conductivity of the solution rose rapidly (Fig. 3.13), as negative ions desorbed from the NPs' surface into the solution due to transition via IEP. Therefore, the base was added to get pH back into the desired pH range and then titration in the direction to base continued. During the 2nd round sudden jumps of pH and subsequent measurement of skipped points due to buffering happened several times, similarly to the 1st round. Also, an extensive amount of base was needed to increase pH at the end of the direction to base from pH 8.6 to pH 8.8. Again, the addition of that much base caused a substantial increase in conductivity, as shown in Fig. 3.13.

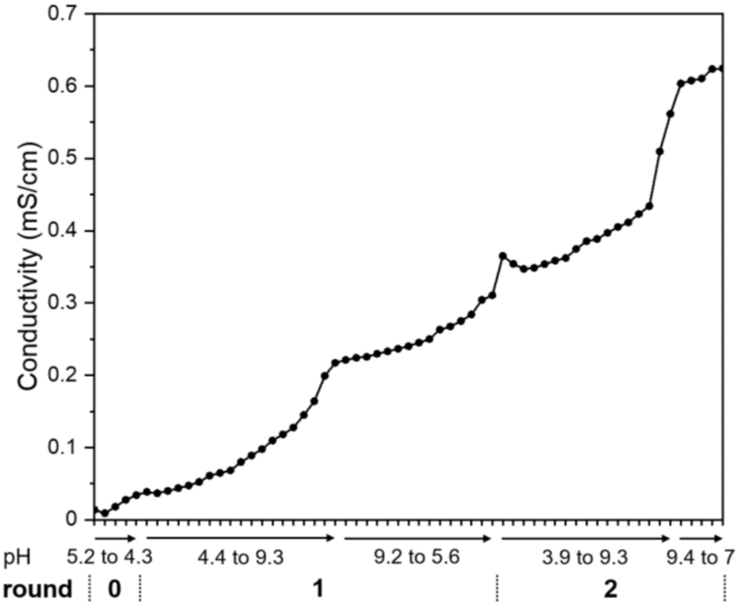

Figure 3.13: Conductivity of sample CG during titration to acid.

As the titration curves did not reach zero ZP in the direction to acid, we can determine the IEP only from direction to base. In the 1st round, IEP was at pH 5.6, while in the 2nd round at pH 4.7, which is significantly lower. At the beginning of the titration, NPs clusters had around 2500 nm in size. During the titration this size was changing – around the IEP increased up to 2800 nm, but in more extreme ZP size of the clusters generally decreased. At the end of the titration average cluster size was around 500 nm.

From the titration curves follows, the ZP was ranging from 30 to -50 mV in the 1st round (Fig. 3.12, left), but only from 6 to -50 mV in the 2nd round. Therefore, the adsorption capacity of glycine-covered Ce NPs for protons decreased during the titration. We assume that negative ions could have adsorbed on NPs partially irreversibly, resulting in the decrease of the free adsorption sites for cations. The presence of negative ions on NPs can also cause a lowering of IEP according to Ref. [94], as we observed in this titration. However, ZP at pH 9.5 remained the same, so the sorption capacity for negative ions was not changed by the titration. Moreover, ZP around -50 mV means the sample has good colloid stability around pH 9 and this characteristic does not change with time.

3.1.2.3.2. Titration to base

In Fig. 3.14 titration curves of sample CG in titration to base are shown. In the direction to acid of the 1st round, the sample started to buffer when a change from pH 8.1 to pH 7.4 should have been performed. Another buffering occurred at the beginning of direction to base in the 1st round. Small amounts of the base were ineffective, therefore larger amount was added causing a sudden increase to pH 9.0. After several minutes, pH decreased as added ions were gradually compensated. For further increase of pH, a relatively large amount of the base was needed, from which follows, that the adsorption capacity of sample CG for negative ions is quite high. In the 2nd round in to acid direction buffering occurred again at pH 6.4. Conductivity was increasing more or less linearly during the whole titration experiment, as shown in Fig. 3.15.

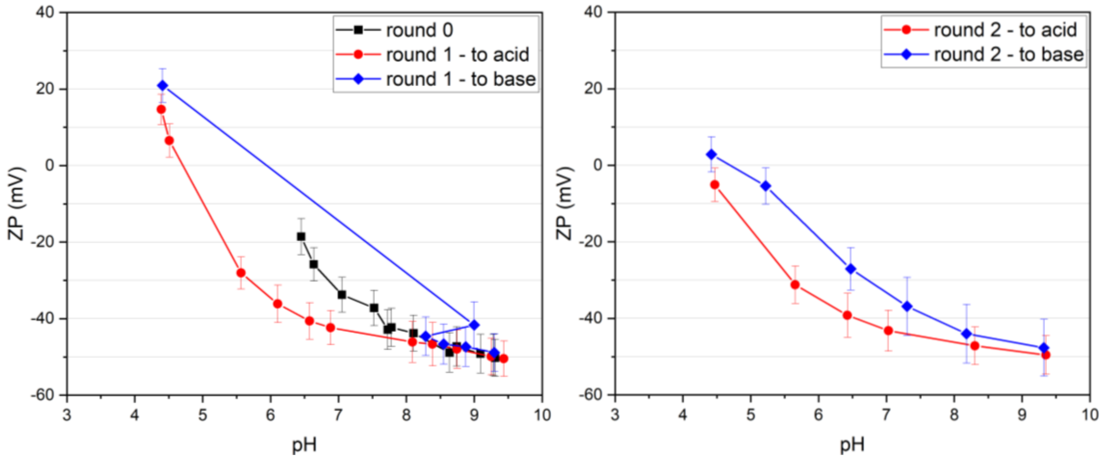

Figure 3.14: Titration to base of sample CG. Titration curves of the 0th and 1st round (left), and 2nd round (right).

Between the titration curve of the 0th round and the curve of the 1st round to acid is a hysteresis for the pH below 7.5. We can see similar hysteresis also in the 2nd round. IEP in direction to acid is at pH 4.7 in the 1st round, but below pH 4.4 in the 2nd round. The size of the clusters was around 2900 nm at the beginning of the titration but varied during the measurement. Around the IEP cluster size reached up to 5000 nm, but when ZP was about -50 mV, size decreased down to 600 nm. At the end of the titration, clusters were about 1400 nm in diameter.

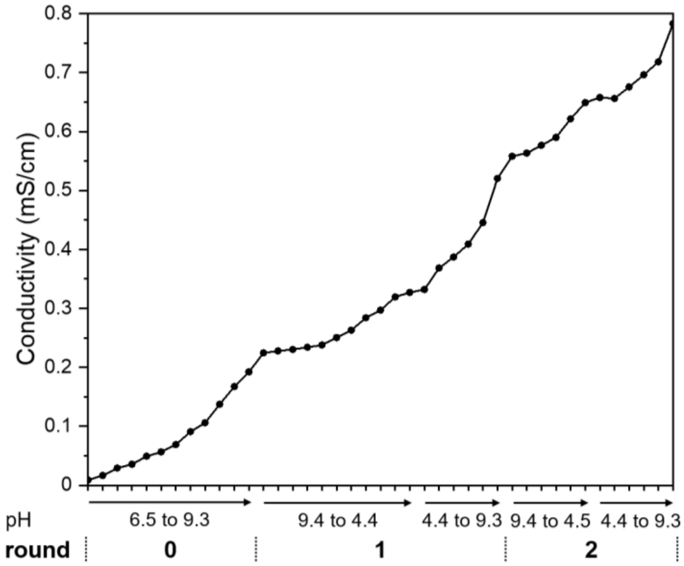

Figure 3.15: Conductivity of sample CG during titration to base.

In the 1st titration round, ZP ranged between 20 to -50 mV, but in the 2nd round only between 3 to -50 mV. Adsorption capacity for positive ions thus decreased during titration but remained the same for negative ions. ZP at pH 9.5 was in both rounds at approximately -50 mV, meaning good colloid stability.

3.1.2.3.3. Comparison of CG titration to acid and to base

When we compare the ZP range in the 1st round, in titration to acid ZP ranged from 30 to -50 mV, but in titration to base it was a bit smaller, ranging only from 20 to -50 mV. In the 2nd round, the difference disappeared, as the ZP range in both titrations was between 5 to -50 mV. It seems, that the decrease in the adsorption capacity for positive ions is connected to transition via IEP or to reaching such a negative ZP in basic pH. One explanation is, that at basic pH negative ions adsorbed on the NPs' surface irreversibly and blocked part of the adsorption sites for positive ions. This is supported also by the lowering of IEP during the titration. Another reason could be the spatial deformation of glycine molecules during the measurement. It is also possible, that when big clusters were created in the vicinity of IEP, NPs were somehow reorganized, resulting in the change described above.

3.1.2.4. Comparison of samples CO, CH and CG

Now we can compare the results of titrations within the samples CO, CH and CG. ZP range in to acid titration in the 0th and 1st round was 40 to -50 mV for sample CO (Fig. 3.2), 60 to -50 mV for sample CH (Fig. 3.6) and 30 to -50 mV for sample CG (Fig. 3.12). In the 0th and 1st round of titration to base, ZP ranged from -40 to -60 mV for sample CO (Fig. 3.4), from 40 to -50 mV for sample CH (Fig. 3.10) and from 20 to -50 mV for sample CG (Fig. 3.14). As the absolute value of ZP reflects the number of ions adsorbed on the NPs' surface, samples differ in adsorption capacity for positive ions, but the adsorption capacity for negative ions is more or less the same. This finding confirms, that molecular surface modification of Ce NPs influences the adsorption capacity of the sample. As all the samples have a high absolute value of ZP in basic pH (-50 mV around pH 9), they are colloidally stable in this environment and this stability lasts at least during the whole titration. For most of the samples ZP range during titration decreases at acid pH. As discussed above, a decrease in adsorption capacity for positive ions depends on the titration direction, mainly on the event of crossing the IEP and reaching minimum ZP in basic pH. We assume, that when basic pH is reached, negative ions adsorb on the NPs' surface, but part of them do not desorb when ZP becomes positive and remains there blocking adsorption sites for positive ions, resulting in the decrease of maximum reached ZP. The only exceptional behaviour was observed in titration to base of sample CO, which probably had been changed before the measurement itself as it already has different starting properties from the other samples, as discussed in the corresponding Subchapter. Therefore, we will not further compare the results of this titration with the others.

Our assumption about blocking adsorption sites is supported also by shifting of the IEP of the samples to lower pH during the titrations of most of the samples. As hysteresis is present in every titration (except CO titration to base in the 1st round), there are always two IEPs – one from the direction to base and one from the direction to acid. In every case, in the majority of the titrations both IEPs decrease, which according to Ref. [94] can be caused by strongly adsorbed negative ions on the NPs.

During the titrations, size of the NPs clusters in the terms of their hydrodynamic diameter was changing due to significant changes in ZP values. In general, cluster size always increased when titration approached IEP. When the extreme ZP values were reached, clusters' size decreased. In sample CH we observed that small NPs clusters (up to 70 nm), which were present in the sample at the beginning, agglomerated due to titrations to bigger clusters at least 850 nm in size. Big clusters present in the sample CG at the beginning (above 2500 nm) became smaller after the titration (above 500 nm in extreme pH). The minimum cluster size around pH 9 in sample CO was approximately 300 nm. Therefore we can conclude that titration increases the minimum size of the clusters of sample CH and decreases it in sample CG. From the starting values of clusters' sizes of each sample we suppose, that presence of histidine molecules on the Ce NPs surface decreases cluster size, while on the other hand presence of glycine molecules increases it. Different cluster sizes can be connected to the different adsorption capacities of each sample, as bigger clusters have smaller surface-to-volume ratio.

Due to the substantial buffering of samples CH and CG, some of their titrations had to be performed half-manually. This behaviour was not surprising, because buffering properties of glycine and histidine in certain pH ranges are widely known. However, sample CO in the titration to acid buffered too, even without the presence of any amino acid on the Ce NPs surface. Therefore it seems, that also the pure Ce NPs have some buffering properties.

3.2. Atomic force microscopy

From the AFM images of samples with neutral pH follows, that at this pH both bare and functionalized NPs tend to agglomerate. The size of the clusters depends on the preparation procedure of a particular sample. As we can see in the left part of Fig. 3.16, in the liquid part of the sedimented NPs solution there are only the smallest NPs clusters. When the solution is agitated, the bigger clusters get into the upper part of the solution, from which the sample was taken. When sonication is applied, even larger clusters appear in the image (Fig. 3.17). This happens because sonication breaks up clusters into smaller parts. These observed clusters are fragments of even larger

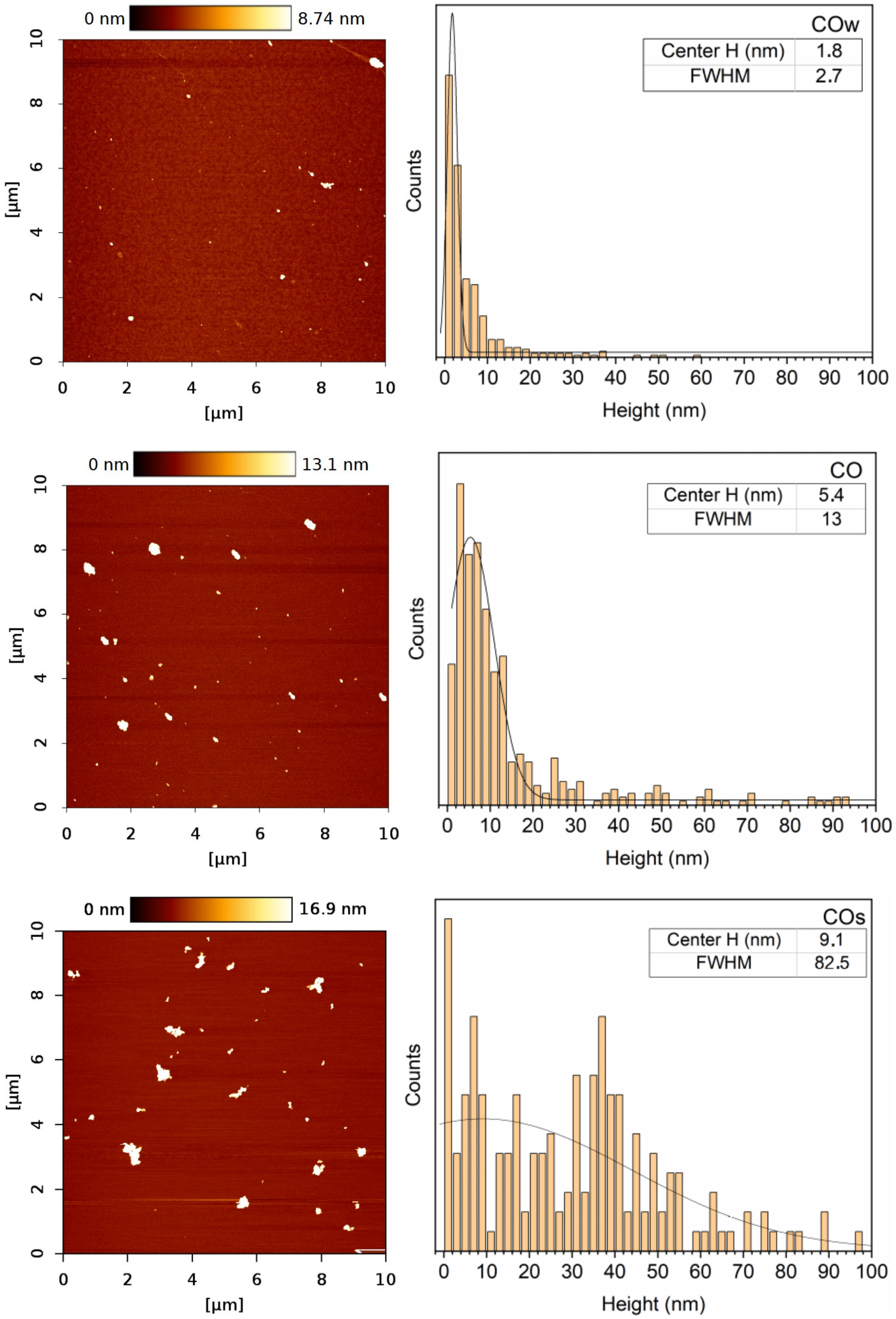

Figure 3.16: In the left part example of AFM 10×10 μm images of samples COw (top), CO (middle) and COs (bottom) at neutral pH prepared by different procedures and in the right part size distributions corresponding to each sample.

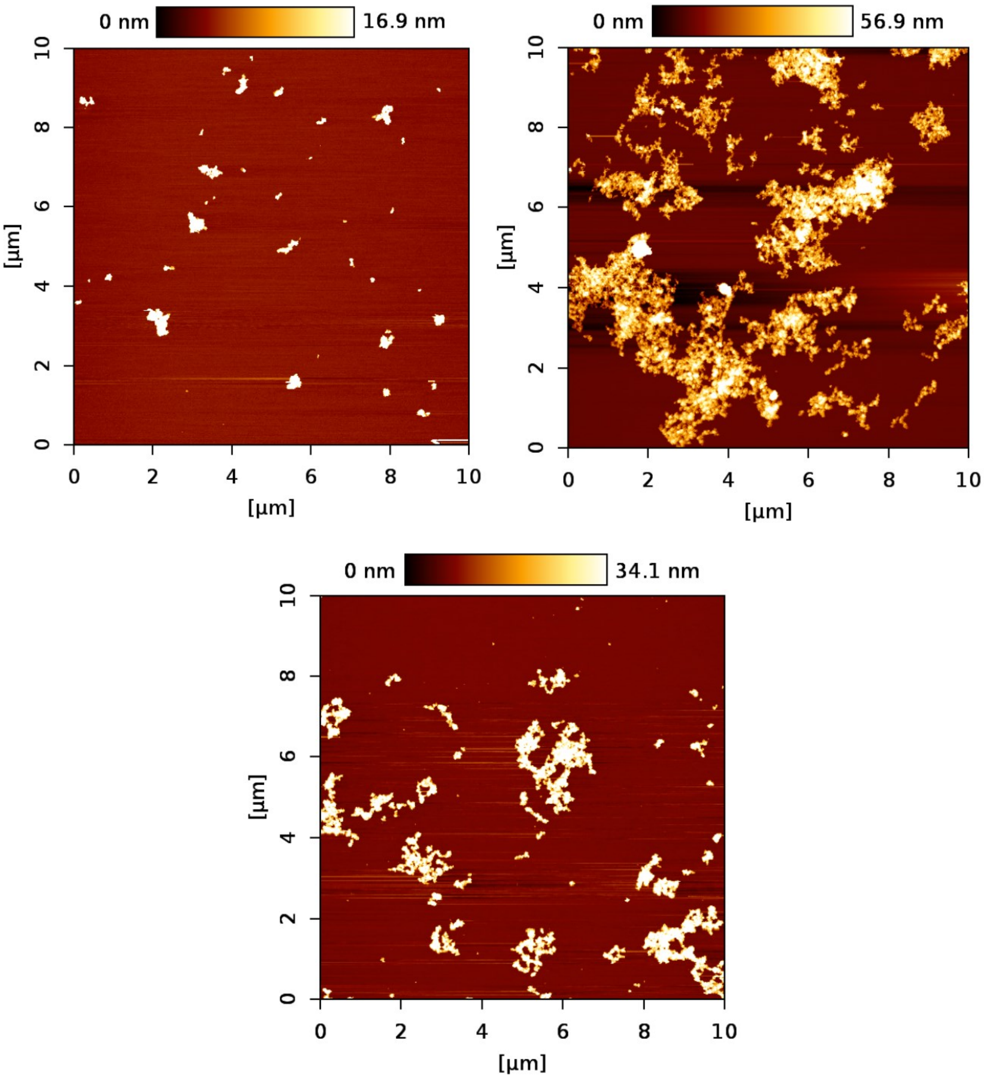

Figure 3.17: Representative example of AFM images of the sample COs (top left), CHs (top right) and CGs (bottom) in a neutral environment.

clusters, which accumulate on the dried drop border and therefore are not present in the measured region.

These findings are confirmed by size distributions of measured NPs clusters smaller than 100 nm (Fig. 3.16, right). For the comparison of the influence of different preparation procedures, only bare Ce NPs could be used. From the functionalized Ce NPs, images of samples CGw and CH only could have been successfully acquired as the remaining samples CG, CGs and CHs contained mainly large clusters accumulated at the dried drop border on mica. Therefore, for these samples, we were not able to acquire images and perform a statistical analysis of the clusters' size. In order to estimate the mean height of large clusters, their height profiles were measured in the AFM image of the sample CHs. By fitting the measured height distribution using

Gaussian fit, it was found that the mean height of the measured clusters is 30 ± 26 nm, where FWHM is taken as a deviation. Having a closer look at the size distribution of the smallest particles in the sample CGw (Fig. 3.18), we can distinguish two peaks at 1.3 and 2.2 nm, which indicate the presence of two phases in the sample, i.e. two types of NPs of different size.

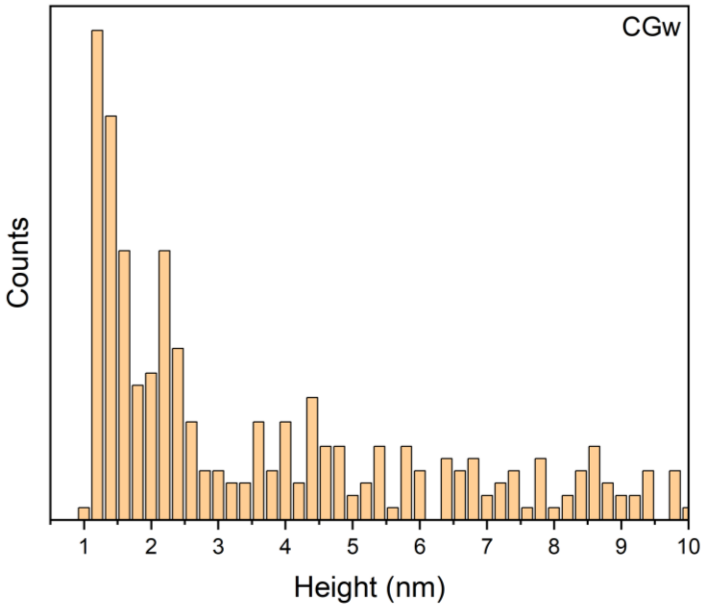

Figure 3.18: Detailed size distribution of the NPs clusters of the sample CGw smaller than 10 nm.

In the next step of the study, we utilized findings from DLS and adjusted the pH of the NPs' colloid solutions to the values where the solutions have higher colloid stability. One sample with acidic (pH around 4.8) and one with basic pH (around 8.8) were measured for each type of NPs (CO, CG, CH). Their AFM images are shown in Fig. 3.19. As we can see, by changing the pH we were able to break up NPs clusters into smaller fragments. We obtained clusters of sizes suitable for AFM measurements even from solutions CG and CH, which were impossible to measure in neutral pH. Images of the sample CO with pH 8.8 and CG with pH 8.9 were further processed to obtain size distributions of the clusters below 100 nm. These distributions are very similar with a centre height of 9.8 nm for CO NPs and 11.9 nm for CG NPs. Compared to the size distribution of sample COs with neutral pH, bare NPs clusters in basic pH have narrower distribution with the majority of the clusters smaller than 20 nm (Fig. 3.20).

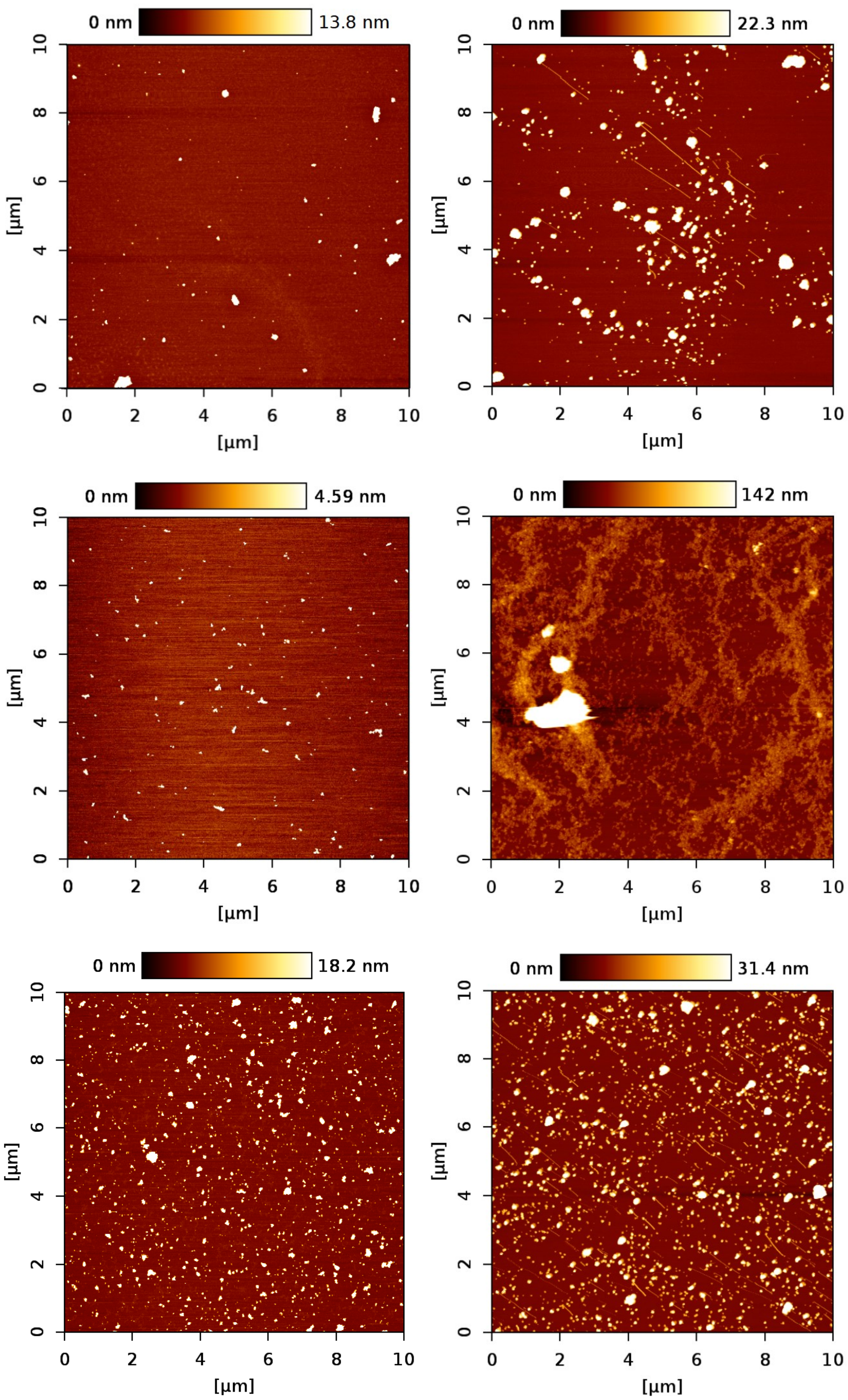

Figure 3.19: AFM images of sample CO with pH 4.8 (top left) and 8.8 (top right), sample CH with pH 4.8 (bottom left) and 8.5 (bottom right), and sample CG with pH 4.8 (middle left) and 8.9 (middle right).

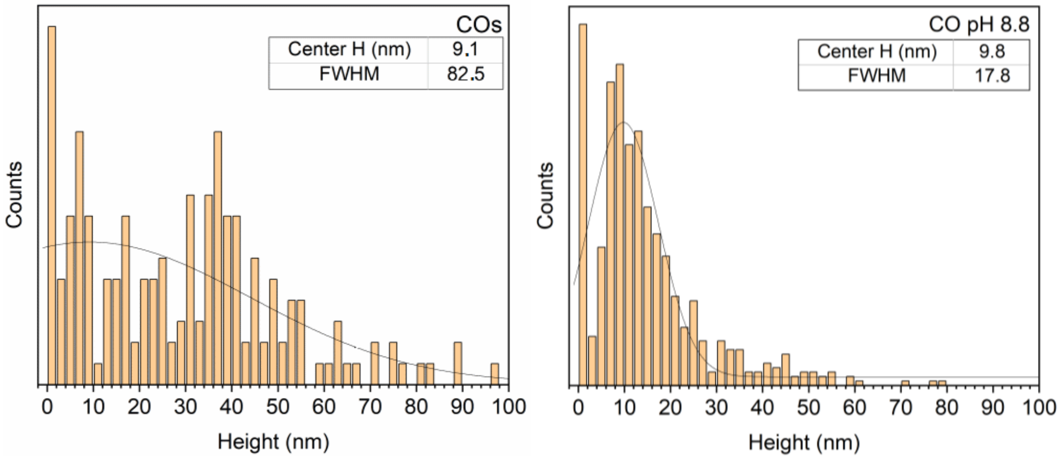

Figure 3.20: Size distributions of sample COs measured at neutral pH (left) and pH 8.8 (right).

Sample CH with pH 8.5 was prepared with a higher concentration of NPs, therefore we observed the creation of a layer as it is shown in Fig. 3.19 bottom right. NPs in this layer seem to be dispersed more or less uniformly creating an incomplete monolayer (Fig. 3.21). It is a confirmation of our hypothesis, that by adjusting the pH of the NPs colloid solution formation of a uniform layer can be achieved. This knowledge can be utilized in the preparation of samples for synchrotron measurements of semiconducting NPs. After a few days under room conditions, the same region of the same sample was measured again in order to assess changes. It was found that the layer becomes less uniform as NPs slowly assemble. Therefore, it is essential to measure the drop-casted NPs layer shortly after preparation to utilize its uniformity.

In the images of samples CO and CG in basic pH, we can see straight oblique lines, which are more or less parallel. Most of these lines have a cluster on their end. As the AFM tip is scanning from the bottom right corner horizontally, these lines correspond to the NPs' clusters which are shifted by the tip every time they get into contact. This phenomenon is observed when clusters are weakly bonded to the substrate and therefore force from the tip is strong enough to overcome this bonding.

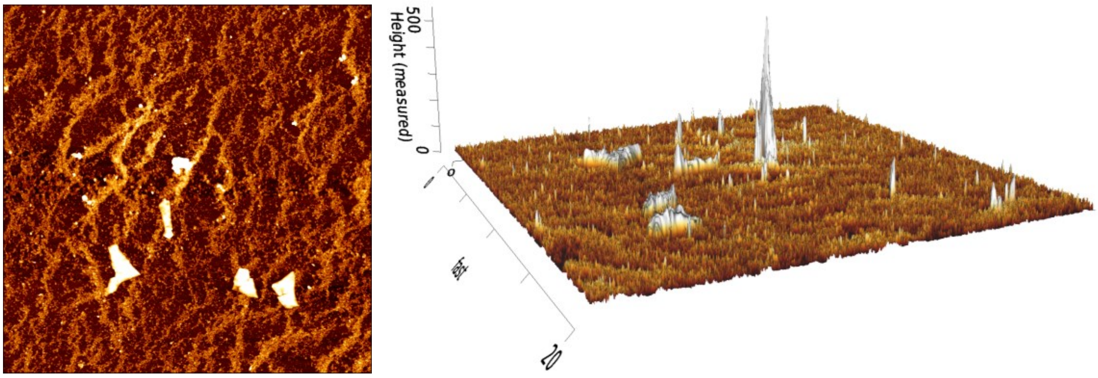

Figure 3.21: AFM image 20×20 µm of sample CH with pH 8.5 in the view from above (left) and side view (right).

3.3. Photoelectron spectroscopies

We measured nine differently prepared samples: bare (CO), histidine-functionalized (CH) and glycine-functionalized (CG) Ce NPs, each at acid, neutral and basic pH. Details about their preparation procedure are described in Subchapter 2.4.3.

By XPS we checked the wide scan spectrum (example in Fig. 2.9) of each sample measured using the laboratory X-ray source. Contributions from carbon, oxygen and cerium were present in every spectrum. When the pH of the sample was adjusted by HCl or NaOH, we could also observe the traces from chlorine or sodium (not shown in the thesis), respectively. There was no other significant contamination noticeable in the XPS spectra.

We analysed the chosen core level spectra as described in Subchapter 2.3.4. SRPES C 1s core level spectra measured with photon energy 410 eV are shown in Fig. 3.22, left. In general, the carbon intensity in the spectra is attenuated compared to the signal from the clean GC substrate, that reflects the presence of the NPs film on the substrate. A dominant peak around 284.5 eV arises mainly from the GC substrate. Histidine or glycine carbon atoms except the one in the carboxyl group contribute to the high BE part of this peak at about 286 eV [63, 64]. The lower C 1s component at binding energy 289.0 eV arises from the carboxylate carbon atom in the molecules (in case of functionalized Ce NPs) and from the contamination by organic acids in ambient conditions. This peak is the most pronounced in the samples CO and CG at pH 6.7. As the molecular signal expected at 286 eV is not well defined, the BE difference between the two components of the C 1s peak from histidine and glycine functionalized NPs cannot be analysed. There is also the Ce 4s peak around the BE of 289.7 eV. However, the photoionization cross section for Ce 4s peak measured with photon energy 410 eV is 0.13, while this value for C 1s core level under the same conditions is 0.44 [96]. Moreover, Ce 4s signal is attenuated by the adlayers of biomolecules or organic impurities. Thus, we do not expect to observe major Ce 4s contribution in the measured C 1s spectrum.

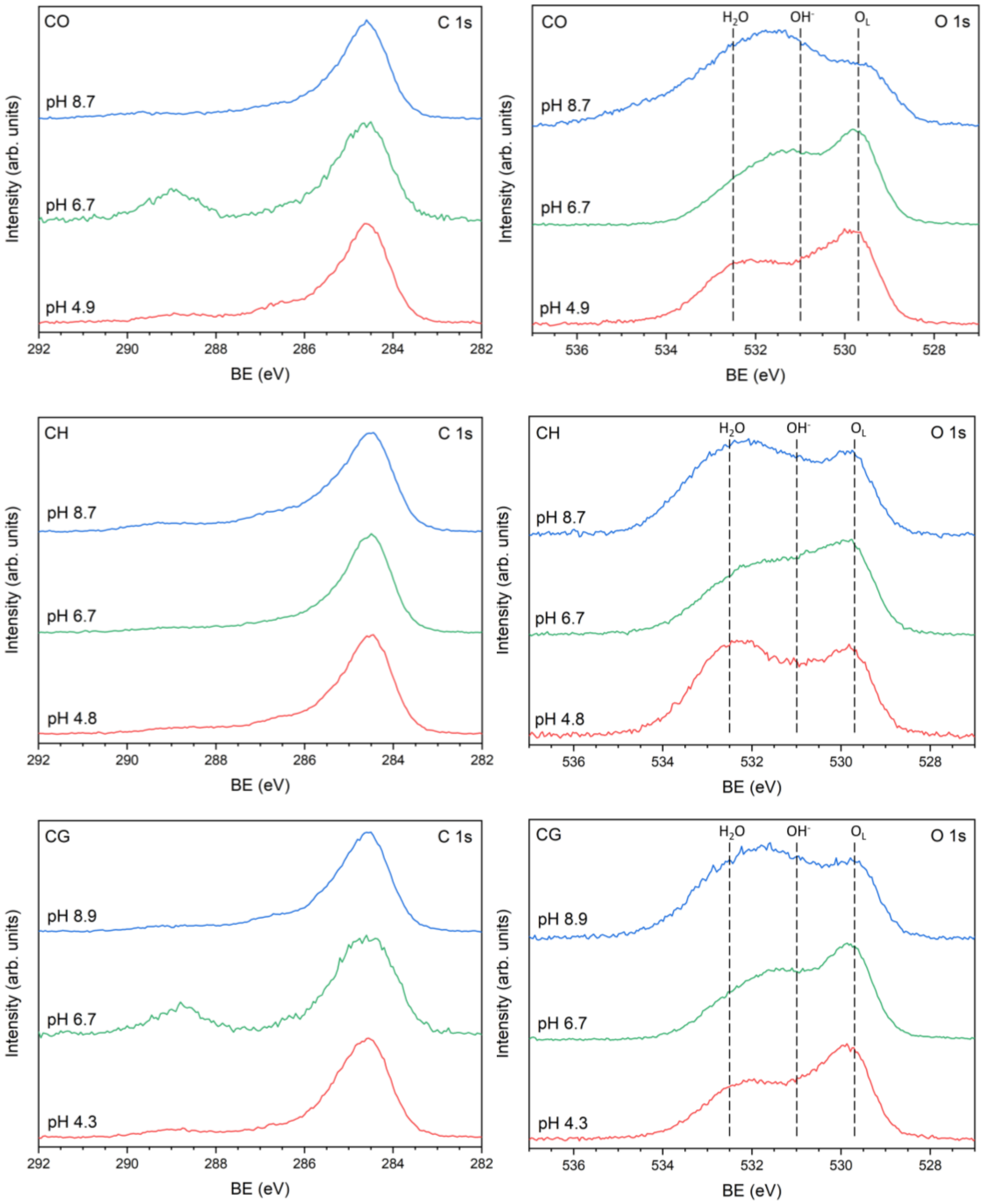

Figure 3.22: SRPES C 1s and O 1s core level spectra of the samples CO (top), CH (middle) and CG (bottom).

SRPES O 1s core level spectra measured with photon energy 630 eV are shown in Fig. 3.22, right. Peak at the BE of 529.7 eV arises from the lattice oxygen, i.e. oxygen atoms of the cerium oxide crystal lattice. The signal at higher BE, the band between 530.5 and 533.5 eV, indicates presence of adsorbed $–OH^-$ groups and H_2O on the surface. The carboxylate oxygen atoms of histidine or glycine contribute to this feature as well. The highest intensity of the signal from $–OH^-$ (H_2O) groups is observed for the samples with basic pH, as expected in the basic environments with high concentration of the $–OH^-$ groups. These findings are in line with the irreversible adsorption of $–OH^-$ ions on Ce NPs at basic pH observed during titration experiments (Subchapter 3.1.2.4).

High intensity in the $–OH^-$ (H_2O) region of O 1s was observed also for the sample CH at pH 4.8 but with slightly different shape. Under assumption that the typical BE of the $–OH^-$ and H_2O species is about 531 and 532.5 eV, respectively, the H_2O component is higher compared to $–OH^-$ signal for sample CH. Moreover, their ratio, i.e. H_2O to $–OH^-$ signals, is highest with respect to samples (CO, CH and CG) at basic pH. It can be elaborated in the following way. The positive charge of CH NPs at pH 4.8, with all tree nitrogen atoms protonated (see Fig. 3.24 and text below), strongly attracts the $–OH^-$ groups in the solution forming adsorbed water molecules, which remained on the surface after drying of the CH drop on the GC surface. Interestingly, the effect is more pronounce for sample CH in comparison to CO and CG systems at acidic pH. We tentatively link this discrepancy to the higher number of protonated nitrogen atoms in histidine (3 N atom) respect to glycine (1 N atom) or clean NPs at acidic pH, which efficiently attract the $–OH^-$ groups to the NPs surface.

In order to determine stoichiometry of the cerium oxide of measured NPs, XPS Ce 3d and SRPES Ce 4d core level spectra were acquired (Fig. 3.23). The Ce 3d core level was measured using Al K-α line with photon energy 1486.6 eV and for the measurement of the Ce 4d spectrum, synchrotron radiation with the photon energy 410 eV was used. Ce 3d spectrum was measured using Al K-α line with photon energy 1486.6 eV and for the measurement of Ce 4d spectrum, synchrotron radiation with photon energy 410 eV was used. Due to the significant difference in the energy of the photon beam, kinetic energies and therefore also the IMFPs of the ejected photoelectrons differ too. According to the software QUASES-IMFP-TPP2M [97], IMFP of the photoelectrons contributing to the Ce 3d core level is approximately 11.7 Å, while in case of the Ce 4d spectrum it is just around 7.4 Å. Therefore, the

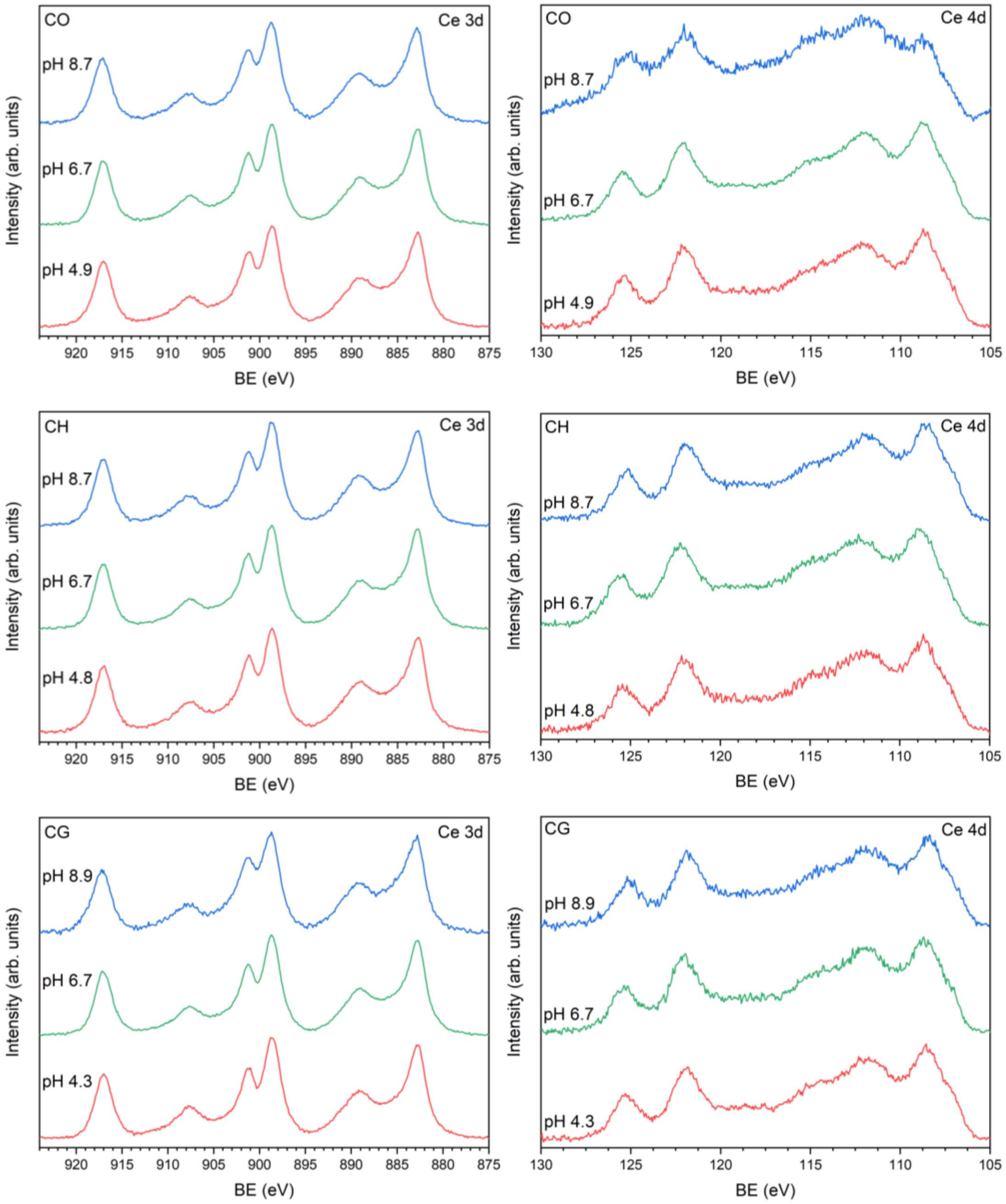

Figure 3.23: XPS Ce 3d and SRPES Ce 4d core level spectra of the samples CO (top), CH (middle) and CG (bottom).

Ce 4d signal gives us more surface-sensitive information, while the information depth of the Ce 3d spectrum is significantly higher.

Base on the shape of Ce 3d core level spectra (Fig. 3.23, left), the cerium oxide is mainly in the form of CeO_2, as expected. The most distinct contribution of Ce^{3+} states in the valley at 886 eV (indicated in Fig. 2.7, left) is minor for all spectra. Shape of Ce 4d spectra (Fig. 3.23, right) confirms this finding also for the surface region of the NPs, as there is no significant contribution of Ce^{3+} features either (according to Fig. 2.7, right). Only the shape of the Ce 4d spectrum of the sample CO at pH 8.7 slightly differs from the others, which can be caused by the remaining minor charging effect, which smears the sharp photoemission features. Although we were not able to determine stoichiometry from the Ce 4d spectra, we could utilize Ce 3d spectra for this purpose. We applied fits (shown in Fig 2.7, left) on each spectrum and from the areas corresponding to Ce^{4+} and Ce^{3+} contributions calculated the ratio of CeO_2 and Ce_2O_3 in the NPs. The averaged stoichiometry of the cerium oxide film was found to be $CeO_{1.95}$ for all the samples.

Another way to determine the ratio of Ce^{3+} and Ce^{4+} states on the surface of the NPs is to use RER calculated from the Ce VB spectra, as described in Subchapter 2.3.2. This technique is even more surface-sensitive than SRPES itself, providing information from just the few top-surface layers. The Ce NPs valence band spectra were measured several times during the PES and NEXAFS experiments. However, in this thesis we show only three RER values for each sample: RER_0 at the beginning of the PES acquisition, RER_1 measured after the all SRPES spectra and RER_2 after the NEXAFS spectra were obtained. These values are shown in Table 3.2. together with corresponding approximate time of irradiation of the sample. We also normalized these values to the RER_0 value of each sample for easier comparison within the samples (Table 3.3).

Sample	pH	RER_0	RER_1	t_1 [h]	RER_2	t_2 [h]
CO	4.9	0.56	0.81	1	0.98	3
	6.7	1.01	1.21	1	1.33	3
	8.7	0.95	0.94	1	0.99	3
CH	4.8	0.93	0.97	1	1.33	3
	6.7	0.66	0.74	1	0.86	3
	8.7	0.69	0.86	1	0.95	3
CG	4.3	0.66	1.00	2	1.19	4
	6.7	0.85	1.03	1	1.17	7
	8.9	0.88	1.01	2	1.06	3

Table 3.2: Determined RER values for all samples. RER_0 is the value measured at the beginning of the PES acquisition, RER_1 is measured at the end of the first SRPES series and RER_2 is determined from the spectra measured after the NEXAFS.

Sample	pH	$nRER_0$	$nRER_1$	t_1 [h]	$nRER_2$	t_2 [h]
CO	4.9	1.00	1.45	1	1.75	3
	6.7	1.00	1.20	1	1.32	3
	8.7	1.00	1.00	1	1.04	3
CH	4.8	1.00	1.04	1	1.43	3
	6.7	1.00	1.12	1	1.30	3
	8.7	1.00	1.25	1	1.38	3
CG	4.3	1.00	1.51	2	1.80	4
	6.7	1.00	1.21	1	1.38	7
	8.9	1.00	1.15	2	1.20	3

Table 3.3: Determined RER values for all samples normalized to RER value measured at the beginning of the PES measurements (RER_0 in Table 3.2).

From the Tables 3.2 and 3.3 follows, that the samples are reduced by the X-ray beam in a vacuum, as the RER increases with the time of exposure to radiation. As explained in Subchapter 2.3.2, higher RER value means higher Ce^{3+} to Ce^{4+} states ratio. This agrees with the findings following from Ce 3d spectra, which were also showing reduction of CeO_2 with the irradiation time but with much lower extent (not shown in the thesis). From the obtained RPES data, we cannot deduce any clear dependence of the surface reduction as a function of pH value or surface functionalization. Further research is needed to be able to draw any conclusions. For now, it seems that the degree of reduction depends strongly on the chosen spot.

Then we analysed the SRPES N 1s spectra, which provide the most valuable information about bonding of histidine and glycine molecules to the NPs surface. However, these spectra were very difficult to measure. We did not observe any nitrogen contribution even when we were quite sure there is N present in the sample. We found out, that our samples were differentially charged, so that the charges on Ce NPs and on the molecules bound to them were not the same. Therefore, even when we found a spot when the charging was not present on Ce NPs (according to the shape of Ce valance band spectra), there could still be charge on the molecules causing the dissipation of the nitrogen peak. It was very difficult and sometimes impossible to find a suitable spot on the sample, where both Ce NPs and molecules were not charged. This indicates, that even though the bond between the molecules and Ce NPs surface is quite strong, it is not sufficient for conducting the charge away from molecules. The best SRPES N 1s core level spectra of samples CH and CG at different pH are shown in Fig. 3.24.

Apart from the nine samples, whose SRPES spectra were presented above, there is also a spectrum of sample CH with pH 6.7 marked with year 2020. This is the only measured spectrum of CH sample at neutral pH yet in which N 1s peak is distinguishable. In this case we were lucky to find the right spot without the differential charging. Unfortunately, we were not able to measure the N 1s peak at neutral pH of samples CH and CG (see Fig. 3.24). As we had problems with the measurement of neutral samples, we utilized results of the DLS and AFM measurements and changed pH of the samples to basic (around pH 8.5) and acid values (around pH 4.5). At these pH values we expected the higher absolute value of ZP and therefore better dispersion of the NPs in solution. As shown in Subchapter 3.2, this leads to the creation of more uniform NPs layers, which would conduct the charge better and thus eliminate the differential charging. This method proved to be helpful for sample CH (at pH 8.7 and 4.8) and also for sample CG at pH 8.9 (see Fig. 3.24). In these cases, we found the spot without charging on Ce NPs quite easily (this applies also for sample CO at basic and acidic pH), in which even the charging on molecules was insignificant. However, change of the pH of sample CG to pH 4.3 did not help to measure the N 1s peak, but at least helped to better conduction of charge away from the cerium oxide surface. It can be noticed, that the spectra in which the N 1s peak is clearly visible correspond to O 1s spectra with the higher signal from $–OH^-$ groups (Fig. 3.22, right). We can conclude that adsorbed $–OH^-$ groups in the Ce NPs system improve the local conductivity of the films used for photoemission experiments.

We analysed and fitted the measured N 1s peaks, as shown in Fig. 3.24. In the N 1s spectrum for the sample CH at pH 6.7 2020, the feature A at 400.4 eV corresponds to amino nitrogen of the IM ring (marked N2 in Fig. 1.2) and the feature B at 399.1 eV to imino nitrogen of the IM ring (marked N3) and α-amino nitrogen (marked N1) engaged in hydrogen bonding with the surface or other molecule [42]. The intensity ratio of components A to B is about 3 to 4, in good accordance with the published data on the histidine adlayer on polycrystalline CeO_2 films, where the strong bonding of the molecular adlayer to the oxide surface was observed exclusively via the carboxylate group. The feature A is shifted to slightly lower BE for the sample CH at pH 8.7, which indicates alternation in chemical environment of the amino N atoms

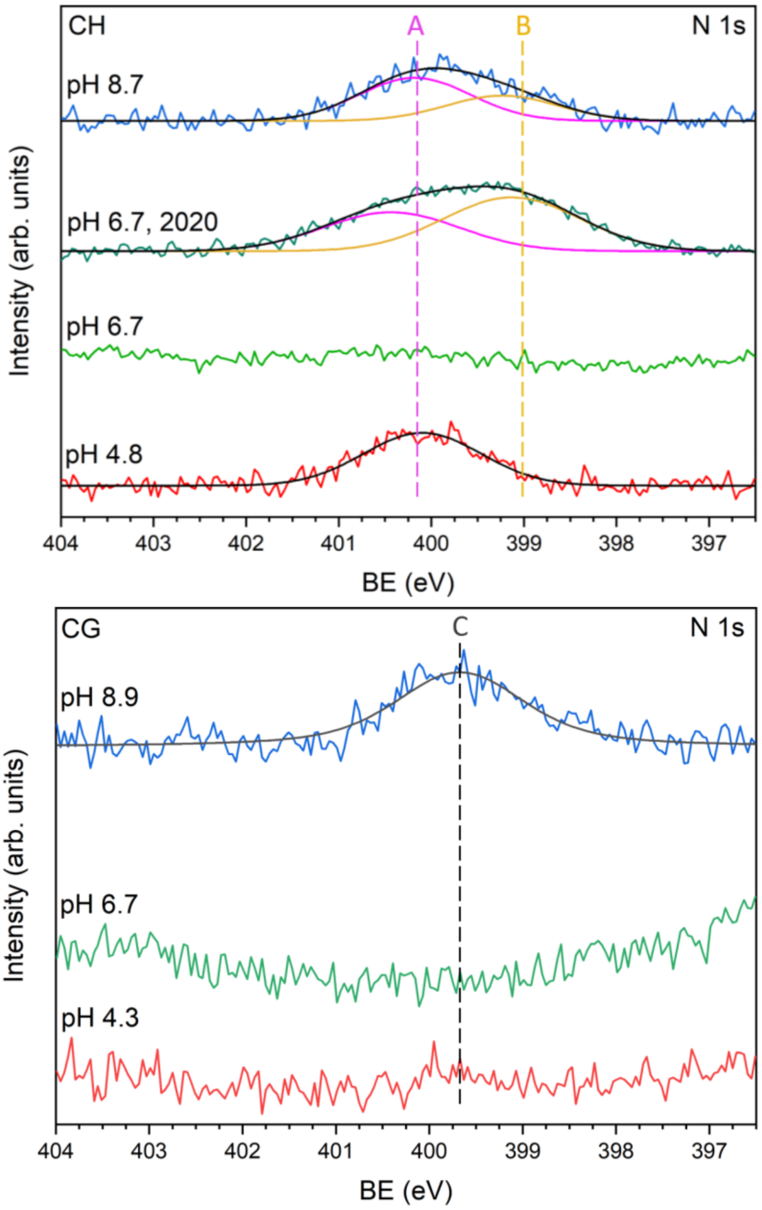

Figure 3.24: SRPES N 1s core level spectra of the samples CH (top) and CG (bottom).

of the molecule. Also, the relative intensity of the component A is higher compared to the peak B with corresponding A to B ratio as 7 to 4. Thus, environment enriched by $-OH^-$ alternates the intermolecular hydrogen bonding and in this case amino nitrogen atoms (marked N1 and N2) contributes more to the component A. This observation indirectly confirms the fact that amino nitrogen atoms are not involved in bonding to the Ce NP at pH 8.7, which is the same scenario as for pH 6.7. Moreover, the component B in N 1s confirms the presence of the imino nitrogen in the imidazole ring, in agreement with the expected ionic forms of histidine shown in Fig. 1.3 and Table 1.1. In the spectrum of the sample CH at pH 4.8, feature B is missing. It indicates, that all nitrogen atoms of histidine are protonated, which leads to the shift of the corresponding peak to the same energy as of the amino nitrogens' component A. It is worth to note that in the proton-rich environment the formation of hydrogen intermolecular network is suppressed due to the low relative concentration of the $–OH^-$ groups in the solution, which in line with the absence of the component B in N 1s for pH 4.8. This explanation agrees also with the expected protonated form of the histidine molecule at pH 4.8, as shown in Fig. 1.3 and Table 1.1. We can conclude that the nitrogen atoms of the histidine molecule directly reflect the change of the relative concentration of H^+ and $-OH^-$ ions in the solution, which is a sign of missing or very weak interaction with the surface of Ce NPs.

The only N 1s spectrum for the Ce NPs functionalized by glycine is visible at pH 8.9. Thus, we were able to acquire the N 1s core level by changing pH to 8.9, which confirms first of all the presence of the molecule on the surface of NPs. The single component peak C in N 1s corresponds to the amino nitrogen atom of glycine. The comparison with the data on closely related system (glycine adlayers on polycrystalline CeO_2) [64] allow us to suppose that the nitrogen of glycine is protonated and this group is not in strong bonding with the surface.

3.4. Near edge X-ray absorption fine structure spectroscopy

The NEXAFS Ce $M_{4,5}$-edge spectra of the measured samples are shown in Fig. 3.25, left. Features marked with F and G correspond to signal from Ce^{3+} and Ce^{4+} states, respectively. Subindices 1 and 2 denote characteristic features for Ce M_5-edge ($3d_{3/2} \rightarrow 4f_{5/2}$ transition) and Ce M_4-edge ($3d_{5/2} \rightarrow 4f_{7/2}$ transition), respectively [98]. Position of the features is more or less identical in all the spectra. Shape of the spectra corresponds well with the previous studies and confirms that Ce NPs are mainly in the form of CeO_2 with a minor presence of Ce_2O_3 phase, which is in good agreement with the $CeO_{1.95}$ film stoichiometry estimated by analysis of the Ce 3d core level.

The NEXAFS O K-edge spectra are shown in the right part of Fig. 3.25. Features marked K, L and M around photon energies 530, 533 and 537 eV correspond to π^* resonances typical for CeO_2. The feature K arises from excitation of the O 1s electron to hybridized Ce $4f^0$−O 2p lowest unoccupied states. Features L and M are assigned to excitation of the O 1s electron to hybridized Ce 5d−O 2p levels, which are

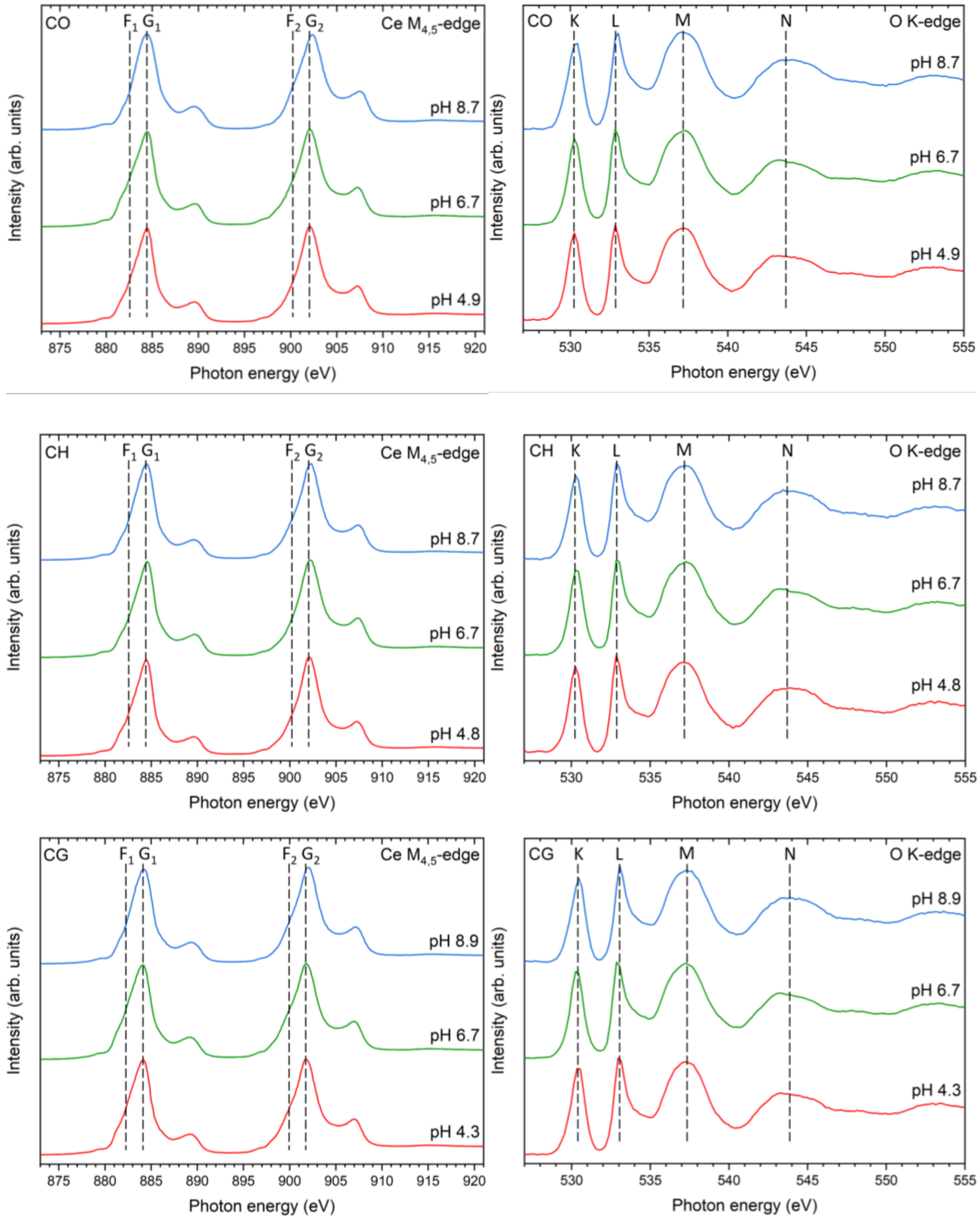

Figure 3.25: NEXAFS Ce $M_{4,5}$-edge and O K-edge spectra of the samples CO (top), CH (middle) and CG (bottom).

split into two distinctive features due to the crystal field effect [81]. A broad peak around photon energy 544 eV marked as N correspond to $1s \rightarrow \sigma^*$ resonances. We can see, that the shape and intensity of the oxygen absorption spectra are almost identical among all samples, confirming 1) the bulk origin of the signal, i.e. from Ce NPs, and

2) expected unresolved features from the molecular adlayers on Ce NPs mainly due to the low coverage.

The NEXAFS C K-edge spectra were acquired but they are very complex due to 1) the use of glassy carbon as a substrate and 2) the presence of possible advantageous carbon in result of sample preparation under ambient conditions. Therefore, we did not analyse them as the information they provide for characterisation of molecular bonding to the Ce NPs surface is not reliable.

The NEXAFS N K-edge spectra are shown only for samples CH and CG, where the presence of the nitrogen signal from amino acids is expected (Fig. 3.26). Spectrum of the sample CH at pH 6.7, 2020 is also shown (corresponding to the N 1s spectra from CH pH 6.7, 2020) as an example of the successful data acquisition. The shape of the N K-edge absorption spectra directly points to the systems where the partial charging occurred: CH at pH 6.7 and CG at pH 6.7 and 4.3, the systems for which N 1s data was impossible to acquire. Other spectra were considered of good quality as the typical regions of π^* and σ^* resonances were easily distinguishable. Features marked P and R at 400 and 402 eV for the CH sample correspond to the π^* resonances of the imino nitrogen and amino nitrogen atoms of the IM ring, respectively [63]. Broad peaks around 407 and 413 eV marked S and T are assigned to $1s \rightarrow \sigma^*$ resonances of all nitrogen atoms of histidine. The presence of two features attributed to π^* resonances confirms the existence of two inequivalent nitrogen atoms in the IM ring. In the spectrum of the sample CH at pH 6.7, 2020, the intensity of the features P and R is practically the same. The last spectrum together with the corresponding N 1s core level closely resemble the spectral features obtained for the histidine adlayer on the polycrystalline cerium oxide film [63], where the molecular bonding through solely the carboxylic group was demonstrated. Thus, we can conclude that the histidine molecule is bound to the Ce NPs at neutral pH in the same way as to CeO_2 polycrystalline film. At pH 8.7, the feature P is very weak (in line with low intensity of the component B of the N 1s core level), which might indicate protonation of the imino nitrogen of the IM ring or some charge redistribution in the ring due to the acidic environment. Again, as for the N 1s results, we can indirectly confirm that the IM ring is not involved in the bonding to the oxide surface. At pH 4.8, the feature P is completely vanishing, which is due to the protonation of imino nitrogen of the IM ring as expected below pH 6 (explained in Subchapter 1.2) and in agreement with the N 1s results. As the π^* resonances structure of the N K-edge reflects the change of pH for each sample and for the case of neutral solution we have direct relation to the published reference system, we are able to conclude that the IM ring is not engaged in the boding of histidine to Ce NPs surface independent of pH and the interface with the oxide is formed exclusively via the carboxylate group.

Spectra of the sample CG at pH 6.7 and pH 4.3 do not correspond to the expected spectral shape according to model systems [64], as was mentioned above. In particularly, we do not observe σ^* resonances, which are expected around the marks Y and Z, due to the presence of charge on the molecular adlayer. At pH 8.9, σ^* resonances are visible in the spectrum, but there is no peak around 400 eV (feature X) corresponding to π^* resonances of amino nitrogen. It is in good agreement with the previous research on the model systems where the π^* resonance feature was very low or missing at 25 °C [64], which is an expected result because the amino group of glycine does not have a double or triple bond. Thus, the molecular structure of glycine is likely to have a free amino group (or weakly bound by hydrogen bonds) and carboxyl oxygen bound to cerium cations on the surface of NPs.

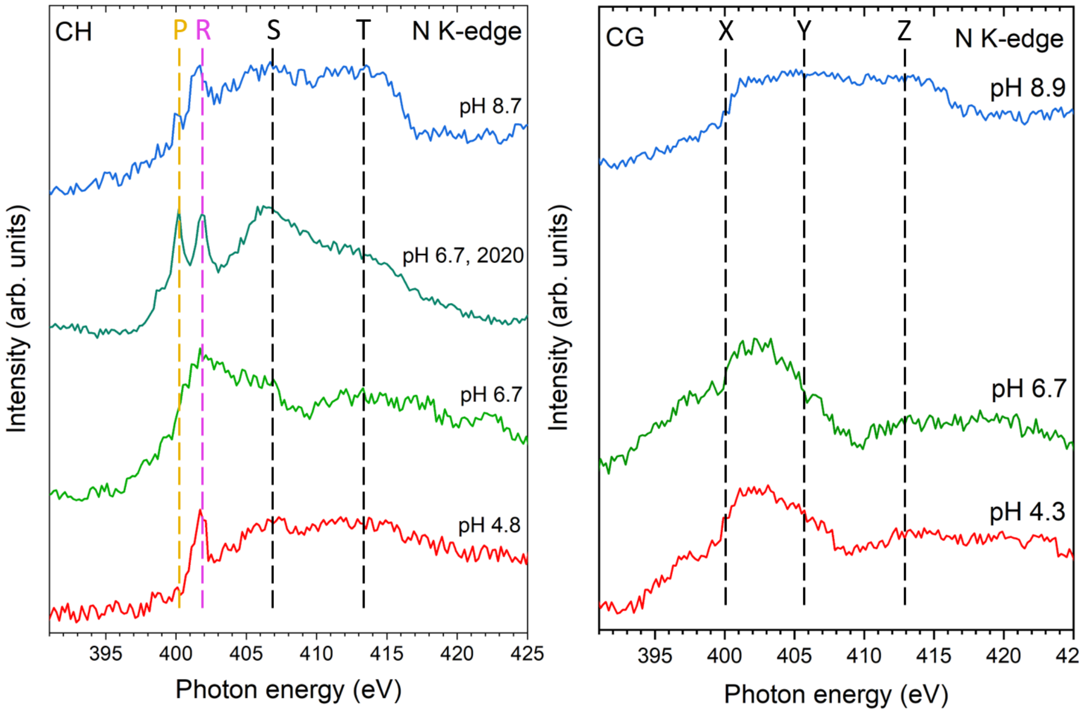

Figure 3.26: NEXAFS N K-edge spectra of the samples CH (left) and CG (right).

Conclusions

Within this thesis we studied cerium oxide nanoparticles, both bare (CO) and functionalized with simple amino acid (histidine (CH) or glycine (CG)). We examined pH dependence of the colloid stability of the samples and its influence on the structure of the dried NPs drop. We determined the best preparation procedure for the measurement of the NPs at synchrotron and using PES and NEXAFS inspected the bonding of histidine and glycine to the surface of Ce NPs.

Colloid solutions of samples CO and CG sediment with passing time, but the sample CH stayed visually homogeneous over several months at least. We have shown that agglomeration and further sedimentation of the NPs is because their zeta potential (ZP) is close to zero at neutral pH. However, ZP changes significantly with the pH. At pH 4.8, the value of ZP lies between 35 to 43 mV for all the samples. Around pH 8.5, ZP of each sample is approximately -55 mV. These ZP values indicate good colloid stability, which leads to the smaller cluster size of NPs.

At the beginning of the titrations, ZP of the samples at acidic pH is positive and at basic pH is negative. ZP range in the 1st titration round differs for each sample. The biggest range has the sample CH: 60 to -50 mV in titration to acid and 40 to -50 mV in titration to base. The sample CO has a smaller ZP range: 40 to -50 mV in titration to acid and -40 to -60 mV in titration to base. The smallest ZP range belongs to the sample CG: 30 to -50 mV in titration to acid and 20 to -50 mV in titration to base. From the ZP ranges listed above follows, that the adsorption capacity for the positive ions increased by functionalization of bare Ce NPs by histidine, but decreased when covered by glycine, which might be connected with the different number of nitrogen atoms per molecule as they are good proton acceptors. We observed, that the maximum ZP reached in acidic pH decreased with increasing titration round, indicating decrease in the adsorption capacity for positive ions. The decrease depends on the titration direction and is connected to events of crossing of IEP and reaching the minimum ZP value in basic pH. ZP around pH 9 remained the same in all samples (around -50 mV), which means the adsorption capacity for negative ions did not change due to titration. We suppose, that some of the negative ions are adsorbed irreversibly in basic pH and then block activity in acidic pH.

As the NPs agglomerate and due to possible dust particles in the NPs solutions, we were able to measure only the upper limit of the hydrodynamic diameter of the clusters' size and observe its behaviour during the titration. As expected, the size of the clusters decreased when the absolute value of ZP increased and vice versa. Initial cluster size was the smallest for the sample CH, just around 70 nm, but the biggest for the sample CG, at least 3500 nm. Comparison with the sample CO with NPs clusters of several hundreds of nm, allow us to conclude, that functionalization of Ce NPs by histidine decreases the size of the clusters and glycine increases it. The titration process caused small clusters of the sample CH to agglomerate and big clusters of the sample CG to break into the smaller ones.

The buffering of all samples was observed, which complicated titration measurements. It was not surprising in samples CG and CH, as both glycine and histidine are used as buffers. However, bare Ce NPs seem to also have some buffering properties itself. Although the buffering was a problem for the measurements, it can be an advantageous quality in the applications as these systems can stabilize biological environment.

By the AFM measurements we directly showed, that the NPs in solutions agglomerate and sediment. We verified, that by applying an ultrasonic bath for 15 min on the samples, the clusters are broken to smaller pieces to some extent. However, in case of samples CG and CH it was not sufficient to prepare clusters small enough to safely image and analyse them using AFM. When we adjusted pH of the samples to the values in which we expected the high absolute value of ZP according to the DLS measurements (around pH 4.5 or pH 8.8), the clusters' size distribution changed significantly. The clusters became smaller and more uniformly distributed over the substrate, creating a slightly imperfect monolayer when deposited in higher concentration.

The main challenge connected to photoemission studies was to eliminate the differential charging on NPs. At neutral pH we were not able to adjust the preparation procedure to surely find a spot without charging of the adsorbed molecules. Thus we successfully measured CH system at pH 6.7 in 2020 and were not able to repeat it in 2021. We utilized the result of DLS and AFM measurements and changed the pH of the sample to the values where the colloid stability is high and therefore a uniform dried drop is created. The pH adjustment helped to measure the NPs samples in both acidic and basic pH in case of samples CO and CH, but only in basic pH in the sample

CG. SRPES spectra of the Ce 4d core level, XPS spectra of Ce 3d and NEXAFS Ce $M_{4,5}$-edge and O K-edge spectra show that the Ce NPs are mainly in the form of cerium dioxide. More precisely, the average stoichiometry of Ce NPs is $CeO_{1.95}$ for all the samples at the beginning of the measurements. This is confirmed also by the RER values obtained from RPES measurements, from which also follows that the cerium oxide is being reduced by the irradiation. From N 1s core level and NEXAFS N K-edge spectra follow, that neither the IM ring of histidine is engaged in bonding to the NPs surface nor the amino group of glycine is strongly bound to the oxide at pH 8.9. We have indirectly confirmed that bonding of glycine and histidine to the Ce NPs surface most likely occurs via the deprotonated carboxylic group in both cases.

In general, this work demonstrated the applicability of the photoelectron based experimental techniques to the Ce NPs systems, bare or functionalised with biomolecules. For the first time the double charging effect, i.e. for the substrate and for the molecular adlayer, was clearly observed and analysed. It was concluded that the absence of the N 1s signal is not a reason to suppose that the molecules are absent on the surface but a sign of the possible charging effect. The thesis also suggests an approach in preparation of more homogenously distributed films of Ce NPs on a substrate by changing the pH of the colloid solution, for which the above-mentioned difficulties in application of the experimental techniques can be overcome.

Bibliography

1. WEN, Jia, YANG, Kui, LIU, Fengyu, LI, Hongjuan, XU, Yongqian and SUN, Shiguo. Diverse gatekeepers for mesoporous silica nanoparticle based drug delivery systems. *Chem. Soc. Rev*. 2017. Vol. 46, p. 6024. DOI 10.1039/c7cs00219j.
2. ABDELAZIZ, Hadeer M., GABER, Mohamed, ABD-ELWAKIL, Mahmoud M., MABROUK, Moustafa T., ELGOHARY, Mayada M., KAMEL, Nayra M., KABARY, Dalia M., FREAG, May S., SAMAHA, Magda W., MORTADA, Sana M., ELKHODAIRY, Kadria A., FANG, Jia You and ELZOGHBY, Ahmed O. Inhalable particulate drug delivery systems for lung cancer therapy: Nanoparticles, microparticles, nanocomposites and nanoaggregates. *Journal of Controlled Release*. 2018. Vol. 269, p. 374–392. DOI 10.1016/j.jconrel.2017.11.036.
3. JIANG, Xiaomin, HE, Chunbai and LIN, Wenbin. Supramolecular metal-based nanoparticles for drug delivery and cancer therapy. *Current Opinion in Chemical Biology* [online]. April 2021. Vol. 61, p. 143–153. DOI 10.1016/j.cbpa.2021.01.005. Available from: https://doi.org/10.1016/j.cbpa.2021.01.005
4. LEI, Can, LIU, Xiu Ran, CHEN, Quan Bing, LI, You, ZHOU, Jia Li, ZHOU, Ling Yue and ZOU, Tao. Hyaluronic acid and albumin based nanoparticles for drug delivery. *Journal of Controlled Release*. 2021. Vol. 331, no. January, p. 416–433. DOI 10.1016/j.jconrel.2021.01.033.
5. FAN, Yu, LIU, Shange, YI, Yu, RONG, Hongpan and ZHANG, Jiatao. Catalytic Nanomaterials toward Atomic Levels for Biomedical Applications: From Metal Clusters to Single-Atom Catalysts. *ACS Nano* [online]. 2021. Vol. 15, no. 2, p. 2005–2037. DOI 10.1021/acsnano.0c06962. Available from: https://pubs.acs.org/doi/abs/10.1021/acsnano.0c06962
6. YOGESH, Gaurav Kumar, SHUAIB, E. P., ROOPMANI, Purandhi, GUMPU, Manju Bhargavi, KRISHNAN, Uma Maheswari and SASTIKUMAR, D. Synthesis, characterization and bioimaging application of laser-ablated graphene-oxide nanoparticles (nGOs). *Diamond and Related Materials*. 2020. Vol. 104, p. 107733. DOI 10.1016/j.diamond.2020.107733.

7. MA, Qinqin, WANG, Jie, LI, Zhiheng, LV, Xiaobo, LIANG, Ling, YUAN, Quan, MA, Q Q, WANG, J, LI, Z H, LV, X B, YUAN, Q and LIANG, L. Recent Progress in Time-Resolved Biosensing and Bioimaging Based on Lanthanide-Doped Nanoparticles. *Small* [online]. 2019. Vol. 15. DOI 10.1002/smll.201804969. Available from: https://doi.org/10.1002/smll.201804969.
8. PIETRZAK, Mariusz and IVANOVA, Polina. Bimetallic and multimetallic nanoparticles as nanozymes. *Sensors and Actuators, B: Chemical*. 2021. Vol. 336, p. 129736. DOI 10.1016/j.snb.2021.129736.
9. FARKA, Zděnek, ČUNDERLOVÁ, Veronika, HORÁČKOVÁ, Veronika, PASTUCHA, Matěj, MIKUŠOVÁ, Zuzana, HLAVÁČEK, Antonín and SKLÁDAL, Petr. Prussian Blue Nanoparticles as a Catalytic Label in a Sandwich Nanozyme-Linked Immunosorbent Assay. *Anal. Chem.* [online]. 2018. Vol. 90, p. 2348–2354. DOI 10.1021/acs.analchem.7b04883. Available from: https://pubs.acs.org/sharingguidelines
10. GAO, Min, AN, Pengli, RAO, Honghong, NIU, Zhengrong, XUE, Xin, LUO, Mingyue, LIU, Xiuhui, XUE, Zhonghua and LU, Xiaoquan. Molecule-gated surface chemistry of Pt nanoparticles for constructing activity-controllable nanozymes and a three-in-one sensor. *Analyst*. 2020. Vol. 145, p. 1279. DOI 10.1039/c9an01956a.
11. KHORRAMI, Mohammad Bagher, PASDAR, Alireza, GHAYOUR-MOBARHAN, Majid, RIAHI-ZANJANI, Bamdad, ZARE, Mohammad and DARROUDI, Majid. Antioxidant and toxicity studies of biosynthesized cerium oxide nanoparticles in rats. *International Journal of Nanomedicine* [online]. 2019. Vol. 14, p. 2915–2926. DOI 10.2147/IJN.S194192. Available from: http://dx.doi.org/10.2147/IJN.S194192
12. LIN, Yi Hsuan, SHEN, Li Jiuan, CHOU, Tzu Ho and SHIH, Yang hsin. Synthesis, Stability, and Cytotoxicity of Novel Cerium Oxide Nanoparticles for Biomedical Applications. *Journal of Cluster Science* [online]. 2021. Vol. 32, no. 2, p. 405–413. DOI 10.1007/s10876-020-01798-4. Available from: https://doi.org/10.1007/s10876-020-01798-4
13. GARCÍA-SALVADOR, Adrián, KATSUMITI, Alberto, ROJAS, Elena, ARISTIMUÑO, Carol, BETANZOS, Mónica, MARTÍNEZ-MORO, Marta, MOYA, Sergio E. and GOÑI-DE-CERIO, Felipe. A complete in vitro

toxicological assessment of the biological effects of cerium oxide nanoparticles: From acute toxicity to multi-dose subchronic cytotoxicity study. *Nanomaterials*. 2021. Vol. 11, no. 6. DOI 10.3390/nano11061577.

14. WU, Di, ZHANG, Juanjuan, DU, Wenchao, YIN, Ying and GUO, Hongyan. Toxicity mechanism of cerium oxide nanoparticles on cyanobacteria Microcystis aeruginosa and their ecological risks. *Environmental Science and Pollution Research*. 2022. No. 2013. DOI 10.1007/s11356-021-18090-1.
15. JUNG, Heejung, KITTELSON, David B. and ZACHARIAH, Michael R. The influence of a cerium additive on ultrafine diesel particle emissions and kinetics of oxidation. *Combustion and Flame*. 2005. Vol. 142, no. 3, p. 276–288. DOI 10.1016/j.combustflame.2004.11.015.
16. CAMPBELL, Charles T. and PEDEN, Charles H.F. Oxygen vacancies and catalysis on ceria surfaces. *Science*. 2005. Vol. 309, no. 5735, p. 713–714. DOI 10.1126/science.1113955.
17. REED, Kenneth, CORMACK, Alastair, KULKARNI, Aniruddha, MAYTON, Mark, SAYLE, Dean, KLAESSIG, Fred and STADLER, Brad. Exploring the properties and applications of nanoceria: Is there still plenty of room at the bottom? *Environmental Science: Nano*. 2014. Vol. 1, no. 5, p. 390–405. DOI 10.1039/c4en00079j.
18. IVANOV, Vladimir K., SHCHERBAKOV, A. B. and USATENKO, A. V. Structure-sensitive properties and biomedical applications of nanodispersed cerium dioxide. *Russian Chemical Reviews* [online]. 30 September 2009. Vol. 78, no. 9, p. 855–871. DOI 10.1070/RC2009v078n09ABEH004058. Available from: http://stacks.iop.org/0036-021X/78/i=9/a=R04?key=crossref.fbc8e678801818a490fc893759731866
19. MORSHED, A. H., MOUSSA, M. E., BEDAIR, S. M., LEONARD, R., LIU, S. X. and EL-MASRY, N. Violet/blue emission from epitaxial cerium oxide films on silicon substrates. *Applied Physics Letters*. 1997. Vol. 70, no. 13, p. 1647–1649. DOI 10.1063/1.118658.
20. CORMA, Avelino, ATIENZAR, Pedro, GARCÍA, Hermenegildo and CHANE-CHING, Jean Yves. Hierarchically mesostructured doped CeO2 with potential for solar-cell use. *Nature Materials*. 2004. Vol. 3, no. 6, p. 394–397. DOI 10.1038/nmat1129.
21. JASINSKI, Piotr, SUZUKI, Toshio and ANDERSON, Harlan U.

Nanocrystalline undoped ceria oxygen sensor. *Sensors and Actuators B: Chemical* [online]. 15 October 2003. Vol. 95, no. 1–3, p. 73–77. [Accessed 29 March 2022]. DOI 10.1016/S0925-4005(03)00407-6. Available from: https://linkinghub.elsevier.com/retrieve/pii/S0925400503004076

22. CELARDO, Ivana, PEDERSEN, Jens Z., TRAVERSA, Enrico and GHIBELLI, Lina. Pharmacological potential of cerium oxide nanoparticles. *Nanoscale*. April 2011. Vol. 3, no. 4, p. 1411–1420. DOI 10.1039/c0nr00875c.
23. CASALS, Gregori, PERRAMÓN, Meritxell, CASALS, Eudald, PORTOLÉS, Irene, FERNÁNDEZ-VARO, Guillermo, MORALES-RUIZ, Manuel, PUNTES, Victor and JIMÉNEZ, Wladimiro. Cerium oxide nanoparticles: A new therapeutic tool in liver diseases. *Antioxidants*. 2021. Vol. 10, no. 5, p. 1–23. DOI 10.3390/antiox10050660.
24. CHAI, Wui Fang and TANG, Kim San. Protective potential of cerium oxide nanoparticles in diabetes mellitus. *Journal of Trace Elements in Medicine and Biology* [online]. 2021. Vol. 66, p. 126742. DOI 10.1016/j.jtemb.2021.126742. Available from: https://doi.org/10.1016/j.jtemb.2021.126742
25. KADIVAR, Fatemeh, HADDADI, Gholamhassan, MOSLEH-SHIRAZI, Mohammad Amin, KHAJEH, Fatemeh and TAVASOLI, Alireza. Protection effect of cerium oxide nanoparticles against radiation-induced acute lung injuries in rats. *Reports of Practical Oncology and Radiotherapy* [online]. 2020. Vol. 25, no. 2, p. 206–211. DOI 10.1016/j.rpor.2019.12.023. Available from: https://doi.org/10.1016/j.rpor.2019.12.023
26. MOGHIMI, Y., BANAEI, A., MAJDAEEN, Mehrsa, ZAMANI, H. and ABEDI-FIROUZJAH, Razzagh. Radiation protection and cytotoxicity effects of different concentrations of cerium oxide nanoparticles in aqueous solution combined with sodium dodecyl sulphate in Vero cells irradiated with 18 MV beams. *International Journal of Radiation Research*. 2021. Vol. 19, no. 4, p. 913–920. DOI 10.52547/ijrr.19.4.18.
27. ALPASLAN, Ece, YAZICI, Hilal, GOLSHAN, Negar H., ZIEMER, Katherine S. and WEBSTER, Thomas J. PH-Dependent Activity of Dextran-Coated Cerium Oxide Nanoparticles on Prohibiting Osteosarcoma Cell Proliferation. *ACS Biomaterials Science and Engineering*. 2015. Vol. 1,

no. 11, p. 1096–1103. DOI 10.1021/acsbiomaterials.5b00194.

28. POPOV, A. L., ABAKUMOV, M. A., SAVINTSEVA, I. V., ERMAKOV, A. M., POPOVA, N. R., IVANOVA, O. S., KOLMANOVICH, D. D., BARANCHIKOV, A. E. and IVANOV, V. K. Biocompatible dextran-coated gadolinium-doped cerium oxide nanoparticles as MRI contrast agents with high: T 1relaxivity and selective cytotoxicity to cancer cells. *Journal of Materials Chemistry B*. 2021. Vol. 9, no. 33, p. 6586–6599. DOI 10.1039/d1tb01147b.

29. FENG, Na, LIU, Ying, DAI, Xianglin, WANG, Yingying, GUO, Qiong and LI, Qing. Advanced applications of cerium oxide based nanozymes in cancer. *RSC Advances*. 2022. Vol. 12, no. 3, p. 1486–1493. DOI 10.1039/d1ra05407d.

30. SAHA, Shibu, ARYA, Sunil K., SINGH, S. P., MALHOTRA, B. D., SREENIVAS, K. and GUPTA, Vinay. Cerium oxide (CeO2) thin film for mediator-less glucose biosensors. In : *Materials Research Society Symposium Proceedings*. 2009. ISBN 9781617383946.

31. VASSIE, James A., WHITELOCK, John M. and LORD, Megan S. Targeted Delivery and Redox Activity of Folic Acid-Functionalized Nanoceria in Tumor Cells. *Molecular Pharmaceutics*. 2018. Vol. 15, no. 3, p. 994–1004. DOI 10.1021/acs.molpharmaceut.7b00920.

32. CAO, Lianlian, SHAO, Guojing, REN, Fengmei, YANG, Minghua, NIE, Yan, PENG, Qian and ZHANG, Peng. Cerium oxide nanoparticle-loaded polyvinyl alcohol nanogels delivery for wound healing care systems on surgery. *Drug Delivery* [online]. 2021. Vol. 28, no. 1, p. 390–399. DOI 10.1080/10717544.2020.1858998. Available from: https://doi.org/10.1080/10717544.2020.1858998

33. YOO, Jihye, PARK, Changhee, YI, Gawon, LEE, Donghyun and KOO, Heebeom. Active Targeting Strategies Using Biological Ligands for Nanoparticle Drug Delivery Systems. *Cancers* [online]. 8 May 2019. Vol. 11, no. 5, p. 640. DOI 10.3390/cancers11050640. Available from: www.mdpi.com/journal/cancers

34. BRANCOLINI, Giorgia and TOZZINI, Valentina. Multiscale modeling of proteins interaction with functionalized nanoparticles. *Current Opinion in Colloid and Interface Science*. 2019. Vol. 41, p. 66–73. DOI 10.1016/j.cocis.2018.12.001.

35. HEUER-JUNGEMANN, Amelie, FELIU, Neus, BAKAIMI, Ioanna, HAMALY, Majd, ALKILANY, Alaaldin, CHAKRABORTY, Indranath, MASOOD, Atif, CASULA, Maria F., KOSTOPOULOU, Athanasia, OH, Eunkeu, SUSUMU, Kimihiro, STEWART, Michael H., MEDINTZ, Igor L., STRATAKIS, Emmanuel, PARAK, Wolfgang J. and KANARAS, Antonios G. The role of ligands in the chemical synthesis and applications of inorganic nanoparticles. *Chemical Reviews* [online]. 2019. Vol. 119, no. 8, p. 4819–4880. [Accessed 18 April 2021]. DOI 10.1021/acs.chemrev.8b00733. Available from: https://pubs.acs.org/sharingguidelines

36. ANTAL, Iryna, KONERACKA, Martina, KUBOVCIKOVA, Martina, ZAVISOVA, Vlasta, JURIKOVA, Alena, KHMARA, Iryna, OMASTOVA, Maria, MICUSIK, Matej, BARATHOVA, Monika, JELENSKA, Lenka, KAJANOVA, Ivana, ZATOVICOVA, Miriam and PASTOREKOVA, Silvia. Targeting of carbonic anhydrase IX-positive cancer cells by glycine-coated superparamagnetic nanoparticles. *Colloids and Surfaces B: Biointerfaces* [online]. 2021. Vol. 205, no. December 2020, p. 111893. DOI 10.1016/j.colsurfb.2021.111893. Available from: https://doi.org/10.1016/j.colsurfb.2021.111893

37. CHEN, Chuanghua, FANG, Jianhua and XU, Chenke. Ultrasonication Mediated Fabrication of Glycine Coated Gadolinium Oxide Nanoparticles as MRI Contrast Agents. *Journal of Cluster Science* [online]. 2021. Vol. 32, no. 3, p. 773–778. DOI 10.1007/s10876-020-01836-1. Available from: https://doi.org/10.1007/s10876-020-01836-1

38. DHANYA, G. R., CAROLINE, D. S., REKHA, M. R. and SREENIVASAN, K. Histidine and arginine conjugated starch-PEI and its corresponding gold nanoparticles for gene delivery. *International Journal of Biological Macromolecules*. 1 December 2018. Vol. 120, p. 999–1008. DOI 10.1016/j.ijbiomac.2018.08.142.

39. BUTAYE, Patrick Rik, COENYE, Tom, CHHIBBER, Sanjay, GONDIL, Vijay S, SHARMA, Samrita, KUMAR, Munish, WANGOO, Nishima and SHARMA, Rohit K. A Novel Approach for Combating Klebsiella pneumoniae Biofilm Using Histidine Functionalized Silver Nanoparticles. *Frontiers in Microbiology* [online]. 2017. Vol. 8, no. 1104. DOI 10.3389/fmicb.2017.01104. Available from: www.frontiersin.org

40. NIVEDHINI ISWARYA, Chandrasekaran, KIRUBA DANIEL, S. C.G. and SIVAKUMAR, Muthusamy. Studies on L-histidine capped Ag and Au nanoparticles for dopamine detection. *Materials Science and Engineering C*. 1 June 2017. Vol. 75, p. 393–401. DOI 10.1016/j.msec.2016.11.102.

41. TSUD, Nataliya, ACRES, Robert G., IAKHNENKO, Marianna, MAZUR, Daniel, PRINCE, Kevin C. and MATOLÍN, Vladimír. Bonding of histidine to cerium oxide. *Journal of Physical Chemistry B*. 2013. Vol. 117, no. 31, p. 9182–9193. DOI 10.1021/jp404385h.

42. TSUD, Nataliya, BERCHA, Sofiia, ACRES, Robert G., VOROKHTA, Mykhailo, KHALAKHAN, Ivan, PRINCE, Kevin C. and MATOLÍN, Vladimír. Functionalization of nanostructured cerium oxide films with histidine. *Physical Chemistry Chemical Physics*. 2015. Vol. 17, no. 4, p. 2770–2777. DOI 10.1039/c4cp03780d.

43. PITTNEROVÁ, Daniela. *Model study of biomolecules bonding to cerium oxide nanoparticles*. Charles University, 2010.

44. ROYAL SOCIETY OF CHEMISTRY. Cerium - Element information, properties and uses | Periodic Table. [online]. [Accessed 29 March 2022]. Available from: https://www.rsc.org/periodic-table/element/58/cerium

45. TROVARELLI, Alessandro. *Catalysis by ceria and related materials*. London : Imperial College Press, 2005. ISBN 1860942997.

46. MATOLÍN, V., MATOLÍNOVÁ, I., SEDLÁČEK, L., PRINCE, K. C. and SKÁLA, T. A resonant photoemission applied to cerium oxide based nanocrystals. *Nanotechnology*. 2009. Vol. 20, no. 21. DOI 10.1088/0957-4484/20/21/215706.

47. VANGELISTA, S., PIAGGE, R., EK, S., SARNET, T., GHIDINI, G., MARTELLA, C. and LAMPERTI, A. Structural, chemical and optical properties of cerium dioxide film prepared by atomic layer deposition on TiN and Si substrates. *Thin Solid Films*. 2017. Vol. 636, p. 78–84. DOI 10.1016/j.tsf.2017.05.034.

48. PRABAHARAN, Devadoss Mangalam Durai Manoharadoss, SADAIYANDI, Karuppasamy, MAHENDRAN, Manickam and SAGADEVAN, Suresh. Structural, Optical, Morphological and Dielectric Properties of Cerium Oxide Nanoparticles. *Materials Research* [online]. 15 March 2016. Vol. 19, no. 2, p. 478–482. DOI 10.1590/1980-5373-MR-2015-0698. Available from:

http://www.scielo.br/scielo.php?script=sci_arttext&pid=S1516-14392016000200478&lng=en&tlng=en

49. LI, He, WANG, Guofeng, ZHANG, Fei, CAI, Yun, WANG, Yude and DJERDJ, Igor. Surfactant-assisted synthesis of CeO2 nanoparticles and their application in wastewater treatment. *RSC Advances* [online]. 2012. Vol. 2, no. 32, p. 12413–12423. DOI 10.1039/C2RA21590J. Available from: https://pubs.rsc.org/en/content/articlehtml/2012/ra/c2ra21590j

50. GRACIANI, Jesús, MÁRQUEZ, Antonio M., PLATA, José J., ORTEGA, Yanaris, HERNÁNDEZ, Norge C., MEYER, Alessio, ZICOVICH-WILSON, Claudio M. and SANZ, Javier Fdez. Comparative Study on the Performance of Hybrid DFT Functionals in Highly Correlated Oxides: The Case of CeO2 and Ce2O3. *Journal of Chemical Theory and Computation* [online]. 2010. Vol. 7, no. 1, p. 56–65. [Accessed 30 March 2022]. DOI 10.1021/CT100430Q. Available from: https://pubs.acs.org/doi/full/10.1021/ct100430q

51. TSCHÖPE, A., SOMMER, E. and BIRRINGER, R. Grain size-dependent electrical conductivity of polycrystalline cerium oxide. I. Experiments. *Solid State Ionics*. 2001. Vol. 139, no. 3–4, p. 255–265. DOI 10.1016/S0167-2738(01)00678-6.

52. HAILSTONE, R. K., DIFRANCESCO, A. G., LEONG, J. G., ALLSTON, T. D. and REED, K. J. A study of lattice expansion in CeO2 Nanoparticles by Transmission Electron Microscopy. *Journal of Physical Chemistry C*. 2009. Vol. 113, no. 34, p. 15155–15159. DOI 10.1021/jp903468m.

53. SUN, Lu, XIAO, Wei, HAO, Xiamin, MENG, Qingling and ZHOU, Miao. A first-principles study on the structural, thermal and electronic properties of cerium oxides by using different functionals. *Electronic Structure*. 2018. Vol. 1, no. 1, p. 015003. DOI 10.1088/2516-1075/aae6f2.

54. DRUGBANK. Glycine. [online]. 2005. Available from: https://www.drugbank.ca/drugs/DB00145

55. NATIONAL CENTER FOR BIOTECHNOLOGY INFORMATION. PubChem Compound Summary for CID 750, Glycine. [online]. 2022. [Accessed 15 April 2022]. Available from: https://pubchem.ncbi.nlm.nih.gov/compound/Glycine#section=Octanol-Water-Partition-Coefficient

56. HUMAN METABOLOME DATABASE. Showing metabocard for Glycine (HMDB0000123). [online]. 2022. [Accessed 18 March 2022]. Available from: https://hmdb.ca/metabolites/HMDB0000123

57. NATIONAL CENTER FOR BIOTECHNOLOGY INFORMATION. PubChem Compound Summary for CID 6274, Histidine. [online]. 2022. [Accessed 15 April 2022]. Available from: https://pubchem.ncbi.nlm.nih.gov/compound/Histidine

58. NCI THESAURUS. Histidine. [online]. [Accessed 15 April 2022]. Available from: https://ncit.nci.nih.gov/ncitbrowser/ConceptReport.jsp?dictionary=NCI_Thesaurus&ns=NCI_Thesaurus&code=C29597

59. PETERSON, Johnny W., BOLDOGH, Istvan, POPOV, Vsevolod L., SAINI, Shamsher S. and CHOPRA, Ashok K. Anti-inflammatory and antisecretory potential of histidine in Salmonella-challenged mouse small intestine. *Laboratory Investigation* [online]. 1998. Vol. 78, no. 5, p. 523–534. Available from: https://pubmed.ncbi.nlm.nih.gov/9605177/

60. MULLER, P. Glossary of terms used in physical organic chemistry: (IUPAC Recommendations 1994). *Pure and Applied Chemistry* [online]. 1994. Vol. 66, no. 5, p. 1077–1184. DOI 10.1351/PAC199466051077/MACHINEREADABLECITATION/RIS. Available from: https://www.degruyter.com/document/doi/10.1351/pac199466051077/html

61. ALIOUCHE, Hidaya. Overview of the Isoelectric Point (pI). *News-Medical* [online]. 2019. [Accessed 16 April 2022]. Available from: https://www.news-medical.net/life-sciences/Overview-of-the-Isoelectric-Point.aspx

62. KORTÜM, Gustav, VOGEL, W. and ANDRUSSOW, K. *Dissociation constants of organic acids in aqueous solution*. London : Butterworths, 1961.

63. BERCHA, Sofiia, MALI, Gregor, KHALAKHAN, Ivan, SKÁLA, Tomáš, PRINCE, Kevin C., MATOLÍN, Vladimír and TSUD, Nataliya. Histidine adsorption on nanostructured cerium oxide. *Journal of Electron Spectroscopy and Related Phenomena*. 2016. Vol. 212, p. 28–33. DOI 10.1016/j.elspec.2016.07.005.

64. KOSTO, Yuliia. *Study of cerium oxide thin films for biosensing applications*. Charles University, 2021.

65. MALVERN INSTRUMENTS LTD. *Zetasizer Nano Series User Manual* [online]. England, 2003. Available from: http://www.nbtc.cornell.edu/facilities/downloads/Zetasizer Manual.pdf

66. BHATTACHARJEE, Sourav. DLS and zeta potential - What they are and what they are not? *Journal of controlled release : official journal of the Controlled Release Society* [online]. 2016. Vol. 235, p. 337–351. [Accessed 31 March 2022]. DOI 10.1016/J.JCONREL.2016.06.017. Available from: https://pubmed.ncbi.nlm.nih.gov/27297779/

67. MALVERN INSTRUMENTS LTD. Measuring Zeta Potential – Laser Doppler Electrophoresis. *Malvern Guides* [online]. 2015. Available from: http://www.pct.hu/wsp_images/zetalde.pdf

68. MALVERN PANALYTICAL. Zetasizer | Expert Light Scattering Instruments. [online]. 2020. [Accessed 31 May 2022]. Available from: https://www.malvernpanalytical.com/en/products/product-range/zetasizer-range

69. MALVERN INSTRUMENTS LTD. *ZETASIZER NANO Series: PERFORMANCE, SIMPLICITY, VERSATILITY* [online]. [no date]. [Accessed 5 December 2021]. Available from: www.malvern.com

70. MALVERN INSTRUMENTS LTD. *Zetasizer Nano Series* [online]. Worcestershire, UK, [no date]. Available from: https://www.malvernpanalytical.com/en/assets/MRK1839_tcm50-17228.pdf

71. MOGENSEN, Mogens, SAMMES, Nigel M. and TOMPSETT, Geoff A. Physical, chemical and electrochemical properties of pure and doped ceria. *Solid State Ionics*. 2000. Vol. 129, no. 1–4, p. 63–94. DOI 10.1016/S0167-2738(99)00318-5.

72. JU, Xiaohui, FUČÍKOVÁ, Anna, ŠMÍD, Břetislav, NOVÁKOVÁ, Jaroslava, MATOLÍNOVÁ, Iva, MATOLÍN, Vladimír, JANATA, Martin, BĚLINOVÁ, Tereza and HUBÁLEK KALBÁČOVÁ, Marie. Colloidal stability and catalytic activity of cerium oxide nanoparticles in cell culture media. *RSC Advances* [online]. 2020. Vol. 10, no. 65, p. 39373–39384. DOI 10.1039/D0RA08063B. Available from: http://xlink.rsc.org/?DOI=D0RA08063B

73. MALVERN INSTRUMENTS LTD. *Zetasizer Software Reference* [online]. 1997. 7.13. Available from:

https://www.malvernpanalytical.com/en/support/product-support/zetasizer-range/zetasizer-nano-range/zetasizer-nano-zs#manuals

74. *Calc | LibreOffice* [online]. 6.0.2.1. [Accessed 3 April 2022]. Available from: https://www.libreoffice.org/discover/calc/

75. *Origin: Data Analysis and Graphing Software* [online]. OriginPro 2020b 9.7.5.184. [Accessed 3 April 2022]. Available from: https://www.originlab.com/index.aspx?go=Products/Origin

76. MIRONOV, V. L. *Fundamentals of Scanning Probe Microscopy*. Nizhniy Novgorod : The Russian Academy of Sciences, Institute of Physics of Microstructures, 2004.

77. JPK INSTRUMENTS. *Nanowizard AFM Handbook*. 6.0. Berlin, 2018.

78. MAGHFIROH, C. Y., ARKUNDATO, A., MISTO and MAULINA, W. Parameters (σ, ε) of Lennard-Jones for Fe, Ni, Pb for Potential and Cr based on Melting Point Values Using the Molecular Dynamics Method of the Lammps Program. *Journal of Physics: Conference Series* [online]. 1 March 2020. Vol. 1491, no. 1, p. 012022. DOI 10.1088/1742-6596/1491/1/012022. Available from: https://iopscience.iop.org/article/10.1088/1742-6596/1491/1/012022

79. SOMORJAI, Gabor A. *Chemistry in two dimensions: surfaces*. Cornell University Press, 1981. ISBN 978-0801411793.

80. SKÁLA, T., ŠUTARA, F., ŠKODA, M., PRINCE, K. C. and MATOLÍN, V. Palladium interaction with CeO2, Sn-Ce-O and Ga-Ce-O layers. *Journal of Physics Condensed Matter*. 2009. Vol. 21, no. 5. DOI 10.1088/0953-8984/21/5/055005.

81. MULLINS, D. R., OVERBURY, S. H. and HUNTLEY, D. R. Electron spectroscopy of single crystal and polycrystalline cerium oxide surfaces. *Surface Science*. 1998. Vol. 409, no. 2, p. 307–319. DOI 10.1016/S0039-6028(98)00257-X.

82. NIEMANTSVERDRIET, J. W. *Spectroscopy in catalysis*. Weinheim : Wiley-VCH, 1995. ISBN 3-527-28726-4.

83. MAX IV. Photoelectron Spectroscopy. [online]. [Accessed 30 March 2022]. Available from: https://www.maxiv.lu.se/accelerators-beamlines/beamlines/flexpes/techniques/photoelectron-spectroscopy/

84. CHUNHAI, Fan and ZHAO, Zhentang (eds.). *Synchrotron radiation in*

materials research. Weinheim : Wiley-VCH, 2018. ISBN 978-3-527-69708-3.

85. STÖHR, Joachim. *NEXAFS spectroscopy*. Heidelberg : Springer Series in Surface Sciences, 1992. ISBN 9788578110796.
86. STÖHR, J. and OUTKA, D. A. Determination of molecular orientations on surfaces from the angular dependence of near-edge x-ray-absorption fine-structure spectra. *Physical Review B* [online]. 15 November 1987. Vol. 36, no. 15, p. 7891–7905. DOI 10.1103/PhysRevB.36.7891. Available from: https://link.aps.org/doi/10.1103/PhysRevB.36.7891
87. JACOBS, A.G. Photoelectron spectrometer, ESCALAB Mk II by Vacuum Generators. [online]. 2017. [Accessed 3 April 2022]. Available from: https://jacobs.physik.uni-saarland.de/home/index.php?page=steinbeiss/home_cms_steinbeissdet3-1&navi=service
88. ELETTRA SINCROTRONE TRIESTE. Lightsources and Laboratories. [online]. [Accessed 31 May 2020]. Available from: https://www.elettra.trieste.it/lightsources/index.html
89. ELETTRA SINCROTRONE TRIESTE. Elettra and FERMI lightsources. [online]. 2011. [Accessed 20 April 2022]. Available from: https://www.elettra.trieste.it/index.html
90. ELETTRA SINCROTRONE TRIESTE. Materials Science Beamline. [online]. [Accessed 5 December 2021]. Available from: https://www.elettra.eu/elettra-beamlines/material_science.html
91. SPECS. Phoibos 150. [online]. [Accessed 31 May 2020]. Available from: https://www.specs-group.com/nc/specs/productseries/detail/phoibos-150/
92. LIBRA, Jiří. *KolXPD* [online]. 1.8.0. Available from: https://www.kolibrik.net/en
93. CHANNEI, Duangdao, PHANICHPHANT, Sukon, NAKARUK, Auppatham, MOFARAH, Sajjad S., KOSHY, Pramod and SORRELL, Charles C. Aqueous and surface chemistries of photocatalytic Fe-doped CeO2 nanoparticles. *Catalysts*. 2017. Vol. 7, no. 2, p. 45–67. DOI 10.3390/catal7020045.
94. GULICOVSKI, Jelena J., BRAČKO, Ines and MILONJIĆ, Slobodan K. Morphology and the isoelectric point of nanosized aqueous ceria sols. *Materials Chemistry and Physics*. 2014. Vol. 148, no. 3, p. 868–873. DOI 10.1016/j.matchemphys.2014.08.063.

95. Biological Buffers. [online]. [Accessed 15 June 2022]. Available from: http://staff.ustc.edu.cn/~liuyz/methods/buffer.htm

96. ELETTRA SINCROTRONE TRIESTE. Atomic Calculation of Photoionization Cross-Sections and Asymmetry Parameters. [online]. [Accessed 20 June 2022]. Available from: https://vuo.elettra.eu/services/elements/WebElements.html

97. TOUGAARD, Sven. *QUASES-IMFP-TPP2M* [online]. [Accessed 20 June 2022]. Available from: http://www.quases.com/products/quases-imfp-tpp2m/

98. WU, Lijun, WIESMANN, H. J., MOODENBAUGH, A. R., KLIE, R. F., ZHU, Yimei, WELCH, D. O. and SUENAGA, M. Oxidation state and lattice expansion of CeO2-x nanoparticles as a function of particle size. *Physical Review B - Condensed Matter and Materials Physics*. 2004. Vol. 69, no. 12, p. 1–9. DOI 10.1103/PhysRevB.69.125415.

List of Tables

List of Abbreviations

AFM	Atomic Force Microscopy
CAT	Constant Analyser Transmission
Ce NPs	Cerium oxide Nanoparticles
CRR	Constant Retarding Ratio
DLS	Dynamic Light Scattering
FWHM	Full Width at Half Maximum
GC	Glassy Carbon
HMA	Hemispherical Analyser
IEP	Isoelectric Point
IM	Imidazole
IMFP	Inelastic Mean Free Path
LDV	Laser Doppler Velocimetry
MSB	Materials Science Beamline
NEXAFS	Near Edge X-ray Absorption Fine Structure Spectroscopy
PALS	Phase Analysis Light Scattering
PES	Photoelectron Spectroscopies
RER	Resonance Enhancement Ratio
RPES	Resonant Photoelectron Spectroscopy
SR	Synchrotron Radiation
SRPES	Synchrotron Radiation Photoelectron Spectroscopy
UHV	Ultra-high Vacuum
XPS	X-ray Photoelectron Spectroscopy
ZP	Zeta Potential